Doping of Hole Conducting Polymers Utilized to Enhance Polymer Electronics

vorgelegt von
Holger Frohne
aus Dortmund

Köln 2004

Berichterstatter: Prof. Dr. Klaus Meerholz
                      Prof. Dr. Bernd Tieke

Tag der mündlichen Prüfung: 07.07.2003

Abstract

For this thesis the system „*poly(3,4-ethylenedioxythiophene) (PEDOT) utilized as electrochemically adjusted anodic material for organic devices*" has been studied in-depth. PEDOT films were polymerized electrochemically being subsequently adjusted to a certain electrochemical potential. Afterwards the resulting work function of the adjusted oxidation level was determined by Kelvin Probe measurements. This thesis provides unambiguous evidence that the work function of the PEDOT film surface is directly (linearly) correlated to the adjusted electrochemical potential. This finding has been utilized for optimising electronic properties of organic devices.

Organic semiconducting polymeric devices of the general structure

indium tin oxide (ITO) / electrochemically deposited and doped PEDOT / electroactive polymer / metal electrode

have been prepared and characterized. By means of electrochemical doping the PEDOT layer was adjusted to a desired potential and its influence on the respective devices was studied.

The adjusted doping level of the PEDOT layer could be directly correlated to its work function. This was demonstrated by Kelvin probe measurements above the semi-freestanding film and by photovoltaic measurements in the finished devices.

Thereafter this discovery was utilized to optimise organic light emitting devices (OLED) by adjusting their hole injection barrier. This barrier is given by the difference in work function between the anodic contact (PEDOT) and the highest occupied molecular orbital (HOMO) level of the adjoining polymer film. If this barrier equals the barrier on the cathodic (metal) side of the device an optimized efficiency can be expected in zero order approximation. Experiments verified this assumption.

If current contributions of holes and electrons are balanced, in principle each charge carrier could find an opposite charge and decay radiatively with the highest efficiency. Although this consideration neglects other influences like different charge carrier mobilities, it is of high interest to gain a possibility which enables current determination for both sorts of charge carriers rather than just the measurement of an overall current. This thesis presents an approach which enables the separation of electron and hole currents for OLED's. The utilization of the results of *hole only* devices (electrons are blocked) allowed predictions about the ratio of current contributions in devices with hole *and* electron currents. These current contributions also confirmed enhanced efficiencies caused by tuned barriers.

Investigations of up-to-date bulk-heterojunction solar cells (OSC) allowed a deeper insight in physical properties which govern these devices. By using a completely undoped PEDOT film the work function of the initial cathodic

(metal) electrode could be passed and the PEDOT took over the cathodic function. Slightly doped PEDOT films could be adjusted to the same level as the metal contact causing zero-built-in-field devices. These investigations enabled a correlation between the anodic and cathodic energy levels and a rough estimation of the adjustable absolute range of PEDOT work functions.

Danksagung - Acknowledgements

Contents

1   Introduction and Motivation

Polymers are long known as materials of technological interest with outstanding tuneable physical and chemical properties. The intense interest is primarily motivated by their advantages over conventional materials, in particular their ease of processing and low cost. They can be adjusted to nearly any technological demand either chemically or physically. On the one hand suitable chemical structures can be synthesized. On the other hand different polymers can be blended in order to benefit from several advantages. Furthermore by aligning the polymer chains enhanced properties in orientation direction can be obtained.

Recently a new class of polymers provide an additional physical property - *conductivity*. Although polymers in general are known to be insulators a special class of polymers containing conjugated π-bonds in their backbones are electrically conductive. The current level of research in the field of conducting and electroactive polymers was sparked by the discovery in 1977 by MacDiarmid, Shirakawa and Heeger (Nobel prize 2000 in Chemistry), who found that chemical doping of polyacetylene increased its conductivity by 7 orders of magnitude, up to 10^3 S/cm.[1] More recent advances have improved its conductivity to 10^5 S/cm, comparable to the conductivity of copper and silver of ~10^6 S/cm.[2]

Knowing that conductivity can be adjusted from insulating to conducting it becomes obvious that semiconducting properties can also be expected which are well known from inorganic semiconductors. Indeed, diodes could be produced, which showed rectification similar to their inorganic counterparts. Even though the first electroactive polymers were developed in the late 1970s, molecular semiconductors have been extensively studied from the 1960s.[3]

Polymers with a suitable band gap even exhibit *electroluminescence* which was discovered in anthracene single crystals in 1963.[4] Development of thin-film electroluminescence was spurred on in the 1980s through the work of Tang and Van Slyke,[5] who demonstrated efficient electroluminescence in two-layer sublimed molecular film devices.

The wide application of these new materials has given rise to interdisciplinary collaborations with scientists from the fields of chemistry, physics, engineering. Conducting polymers have been used as the active material in sensors,[6] transistors,[7-12] organic solar cells (OSC's),[13-14] organic light-emitting diodes (OLED's),[15-19] and organic lasers (OL's).[20-22]

Semiconducting devices in general usually consist of a series of layers:

- electrodes,
- the active semiconductor material,
- insulators

The technique of making devices out of the conventional inorganic materials relies on growing crystals layer-by-layer, a process that is very sensitive to impurities and must be carried out in a controlled environment. Polymers, on the other hand, have the potential to be processed from solution, making it very easy to engineer smooth and thin layers by spincoating techniques. Indeed, many have found important applications, such as the utilization of anthracene, which still is the active component for charge photogeneration and transport in many of the **xerographic copiers** and **laser printers** made nowadays.

Indeed, **colour flatbed dot-matrix displays** are set to be produced by "printing" the light emitting polymers onto the substrate using converted inkjet printers.[23]

The application to the harvesting of solar energy is also of intense interest. To date, due to their high production costs, conventional **solar technology** has yet to see its wide-scale use as a means for utilizing renewable energy. Even if polymers cannot match the conventional technology's performance, cheap mass-produced polymer cells could see the first global-wide employment of solar cells to harness the energy from the biggest nuclear reactor in the solar system, the sun. Such solar cells have the potential to ease the world's energy crisis, and to improve the living standards of those currently without grid power.

Polymer semiconducting devices also have the potential to be flexible, and to be fabricated in various shapes. Conjugated polymers can be incorporated into clothing, a vision that has captured the interest of suppliers for the astronautics, who can see the advantages of **electronic clothes**. Due to their flexibility semiconducting polymers may see also applications in niche areas such as **medical applications**, where curved detectors are required.

There are also first attempts to produce **polymer lasers**. This concept opens up a way to obtain inexpensive lasers that are tuneable over the whole visible range. Although the first (polymer) lasers were 'just' pumped optically newer results seem to enable electrically driven lasers.[24]

The efficiency of the active polymer layer in the mentioned applications strongly depends on the properties of the adjoining electrodes. Charge injection for example plays an important role which governs the efficiency of OLED's. Therefore, this thesis focuses on the determination of work functions of polymeric anodic electrodes and the tunability of their work function. The objective target is to increase efficiency of conjugated devices by controlled charge injection.

When polymeric devices first came up indium tin oxide (ITO) was mostly used as a transparent anodic contact. Nowadays ITO is still used but covered with a layer of a doped π-conjugated polymer which thereafter electronically becomes the anode itself. Having battery powered polymer devices in mind these additional polymer layers could improve respective device properties in

terms of reduced injection barriers for holes, an increased lifetime, an enhanced efficiency and a lowered operating voltage. These improvements were mostly achieved by synthesizing suitable polymers whereas the possibility of electrochemically modifying the hole-injecting polymer layers as an additional approach was neglected for several years.

Although it has been obvious from the literature that the work function of a π-conjugated polymer is correlated with the electrochemical equilibrium potential E_{eq},[25] this concept has not been utilized for polymeric devices for a long time. A linear correlation with an offset of 4.45 eV between the electrochemical potential and the work function is generally assumed.[26] Ultraviolet Photon Spectroscopy (UPS) measured on two differently synthesized PEDOT samples yielded work function values of 4.0 eV for "neutral" and 4.4 eV for "doped" material, respectively.[27] On the other hand a work function of about 5.3 eV was determined by electroabsorption and the Kelvin-probe method.[28] These large variations may either be caused by different experimental methods or originate from differences in the film preparation leading to different degrees of oxidation (work function) of the PEDOT film. Indeed, the mentioned uncertainties caused a lack of knowledge about the energetic conditions at the interfaces between the electrodes and the active layer in organic devices.

First attempts using electrochemically synthesized and treated polymers in organic devices have been made by Markus Groß who started to investigate the work function of poly(4,4'-dimethoxy-bithiophene) (PDBT) in dependence on its oxidation potential.[29] His results were derived indirectly, whereas this thesis aims at quantitative and direct evidence for a changed work function of the anodic polymer and its impact on the devices. For example he determined work function changes by changed diode current characteristics (e.g. changed "onset" voltages), whereas this thesis is based on direct methods like Kelvin Probe or photovoltaic measurement for the determination of changed work functions. For this thesis thin films of the well established anodic polymer PEDOT were examined in a Kelvin probe setup and in OLED's and OSC's later on. The devices and used materials were kept similar in order to get a complete set of data for the system "controlled oxidized PEDOT anode". In addition the experiments were extended to a n-type polymer in order to show exemplarily that the information gathered for PEDOT can be utilized for other systems as well.

Chapter 2 will provide a brief introduction to semiconducting and conducting polymers. In Chapter 3 the experimental techniques will be introduced, which were used for this thesis in order to characterize the polymer layers and the finished devices. Chapter 4 explains the technological background which is necessary to understand the structure and functionality of OLED's and OSC's. In Chapter 5 the results of this thesis are presented and discussed and chapter 6 deals with experimental details.

2 Theoretical Background

Polymers can be conductive and semi-conductive. The physical description and the corresponding models of these phenomena will be treated in this chapter. Furthermore the physical effects at interfaces between different polymer layers and polymer/metal contacts will be discussed.

2.1 Semiconducting and Conducting Polymers

2.1.1 Charge Transport in Conjugated Polymers

The common feature of all carbon-based molecular semiconductors is that they are conjugated, i.e. they consist of alternate single and double carbon-carbon bonds (e.g. Figure 2-2a).

The mechanisms for charge transport in conjugated polymers are completely different to those exhibited by conventional metallic conductors and inorganic semiconductors. In the latter, there is a high degree of periodicity, and conduction electrons move freely on a background lattice of atomic nuclei. Polymer solids, on the other hand, are largely amorphous, and charged species travel more easily along polymer chains, rather than from chain to chain.

Charge transport along conjugated polymers is easiest understood in terms of a charged moiety being flipped along the chain. In such a case, the charged species is not thought of as simply a hole or electron, but as a distortion to the local chain geometry, with a net overall charge, which is transferred along the chain. An example of such a case is polyacetylene. As shown in Figure 2-1, the charged species consists of a two bond length long alteration to the chain geometry. This charged species, known as a (negative) soliton is transported along the chain by flipping back and forth of the single and double bond locations, as illustrated in Figure 2-1.
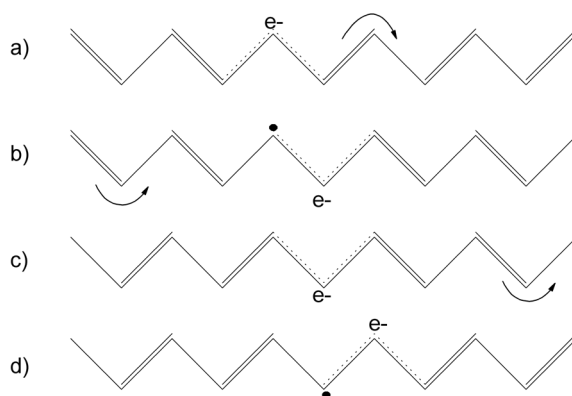
Figure 2-1: a) - d) Schematic illustration of a negative soliton moving along the polymer chain. Double bonds flip back and forth to accommodate its passage.

The real mechanism differs from the schematic representation, as the bonds in conjugated systems are delocalised over a certain length. The double bonds represent regions of high electron density. Fluctuations in electron distribution can initiate a local bond flipping, which can travel along the polymer chain. Since the exact form of the charged species depends in general on the geometry of the chain, they and their transport method are typically different for different polymer types.
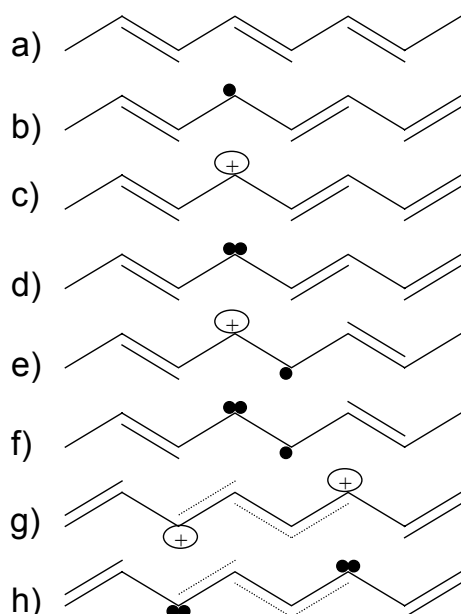
Figure 2-2: Illustration of various quasi-particles on polyacetylen: a) undisturbed conjugation, b) neutral soliton, c) positive soliton, d) negative soliton, e) positive polaron, f) negative polaron, g) positive bipolaron, h) negative bipolaron

Beside the already mentioned negative soliton (Figure 2-2a) positive and neutral solitons can be formed as well (Figure 2-2c+d). In addition defect pairs can be formed from a charged and a neutral soliton - they are called polarons (Figure 2-2e+f). At last bipolarons are pairs of two charged solitons (Figure 2-2g+h).

The most used model for the interpretation of measurements concerning the conductivity of organic materials is the "disorder"-Formalism introduced by Bäßler.[30] Simulations for charge transport often apply this Bäßler formalism. Beside the recurring monomer units polymers have a lack of periodicity. To overcome this lack the Bäßler formalism uses a Gauß distribution for the density of states (DOS) and a Gauß distribution for the distances between charge transporting molecules.[31] These distributions were applied since the absorption spectra of many polymers are widened with a gaussian shape. For the simulation charge carriers are created at random according to these distributions and they travel until become trapped in a position of lowest energy. In this position they stay until they are removed optically, thermally or by an electric field.

2.1.2   Band Gaps in Conjugated Polymers

The origin of the band gap in conjugated polymers is best understood in terms of the bonding and anti-bonding of carbon-carbon double bonds. In these compounds, electrons are delocalized from their parent atoms and form two molecular orbitals of different energies, which act as a highest occupied molecular orbital (HOMO, "valence band") and a lowest unoccupied molecular orbital (LUMO , "conduction band"). Carbon-carbon double bonds are formed when two of the three 2p orbitals on each carbon atom combine with the 2s orbital to form three $2sp^2$ hybrid orbitals. These lie in a plane directed at 120° to each other, and form σ molecular orbitals with neighbouring atoms. The third p orbital on the carbon atom, the $2p_z$, points perpendicularly to this plane, and overlaps with a $2p_z$ orbital on a neighbouring carbon atom, to form a pair of π bonding and π^* antibonding molecular orbitals (Figure 2-3). As equivalent π orbitals are formed between nearby atoms along the chain, the wave-functions overlap, resulting in a delocalisation over the polymer chain.
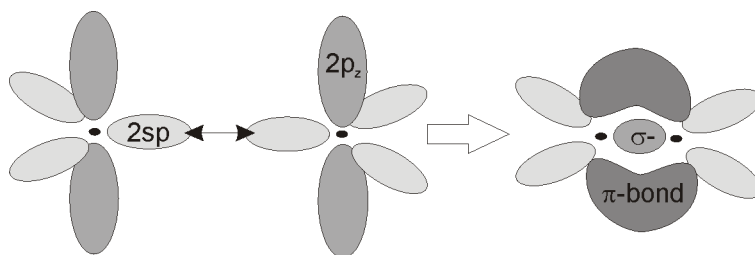
Figure 2-3: The overlapping of $2sp^2$ and $2p_z$ orbitals forms σ and π-bonds respectively.

The difference in energy between the highest occupied molecular orbital (HOMO) in the valence band and the lowest unoccupied molecular orbital (LUMO) in the conduction band gives the energy gap E_{gap}.
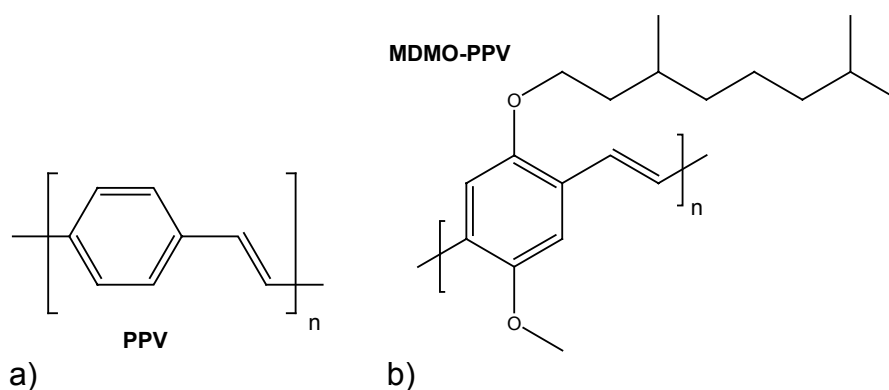
Figure 2-4: Structure of a typical electroluminescent polymer. The backbone is conjugated, i.e. double and single bonds alternate.

a) Poly(*p*-phenylene vinylene) (PPV)
b) PPV derivative called poly(2-methoxy-5-(3',7'-dimethyl)octyloxy-1,4-phenylenevinylene (MDMO-PPV)

Poly(*p*-phenylene vinylene) or PPV (Figure 2-4a) and its derivatives have been the basis for much of past research in semiconducting polymer devices. The band-gap of this polymer can be altered by adding different side groups to the polymer, which can push (pull) charges to (from) the backbone. This process alters the "absorption edge" (compare Figure 5-13) and therefore the band gap. Another duty of side chains is an improved solubility. Compared to the basic PPV (Figure 2-4a) e.g. the solubility for MDMO-PPV has been improved and the colour has been shifted from yellow to orange by an appropriate side chain.

2.1.3   Excitons

In polymer devices the neutral excited state, or exciton, is important, so further discussion of this state is useful. Excitonic effects are well known in many solid state systems, e.g. crystal lattices, and were well studied before electroactive polymers were investigated.

In semiconducting crystals, excitons are electron-hole pairs that are bound together by their Coulombic interaction. They can be formed by photons incident on the photosensitive layer or - the other way round - by coupling of opposite charges travelling through an electroluminescent device. The energy required to create them is less than the band gap. They may travel freely through the crystal transporting excitation energy, but not charge, as they are electrically neutral. So in inorganic crystals the exciton is a mobile neutral excited state of the crystal, which can travel through the crystal and give up its energy by recombination.

For excitons in crystalline solids, two different limiting approximations have been considered: the Frenkel theory in which the exciton is tightly bound and the Mott-Wannier theory in which the exciton is weakly bound, with an electron-hole interparticle distance that is large in comparison with the lattice constant.

The concept of Frenkel excitons and Mott-Wannier excitons can be extended to molecular semiconductors. If the bound electron-hole pair is located on one monomer unit it is classified as a Frenkel exciton, and if the pair extends over many units it is classed as a Mott-Wannier exciton. The behaviour of excitons in conjugated polymers must be different than in inorganic semiconductors, due to the inhomogeneous environment, where excitons are likely to travel more easily along the polymer chain than transverse to it. Indeed, a Mott-Wannier treatment of excitons in PPV[32] calculates an anisotropic effective mass for the exciton ($\mu_{\parallel}$ = 0.0421 m_e, $\mu_{\perp}$ = 2.66 m_e) and anisotropic relative permittivities ($\varepsilon_{\parallel}$ = 8, $\varepsilon_{\perp}$ = 3). The result is an anisotropic ellipsoid, of extension about 2 nm along the chain and 0.4 nm transverse to the chain. This paints a "molecular" picture of the exciton, which seems to be confined to a single chain.

A more complete description of the exciton must take into account both electron-electron interactions and electron-lattice interactions. A consequence

of including electron-electron interactions is that the singlet and triplet excitons are no longer of the same energy, or size. The triplet exciton (net spin S = 1 with individual particle spins aligned) is then considerably more localised than the singlet (S = 0) exciton (as a result of the reversed sign of the exchange interaction). Computer simulations[33] have divined that the triplet exciton in PPV is stabilised by 0.65 eV with respect to the singlet exciton, and is localised over not much more than a single repeat unit, whereas the singlet is considerably more extended and has a binding energy of 2.5 eV.

Excitons are mobile within the polymer solid, and their motion plays a very important part in the photophysics of conjugated polymers. It depends on many factors, how the exciton travels. For example, if there is significant electron-lattice coupling, the Frenkel exciton in PPV is more appropriate to think of it as a localised state that moves by hopping between sites, whereas Mott-Wannier excitons are thought to travel more uniformly.

The exact nature of the excited states and transport of excitons in PPV derivatives is not well understood. To begin with, there are theoretical difficulties in modelling the many complex interactions, where electron-electron and electron-lattice interactions are significant. There are also difficulties in extending these theoretical results to the actual bulk PPV, as impurities and inter-chain interactions are important. Consequently there is still much contention about the exact nature of excitons in PPV. Although agreement between theory and experimental observations has not been achieved, at least the properties illustrated by the one-chain models give an appreciation of how different (compared to traditional semiconductors) and exciting the processes in semiconducting polymers are.[34]

2.2   Organic/Metal and Organic/Organic Interfaces

In this chapter, recent progress in the understanding of the interfacial electronic structures will be reviewed[35] focusing on the results in energy level alignment at the interface. Band bending will also be briefly discussed. In particular, the invalidity of the traditional assumption of a common vacuum level (VL) will be pointed out, which has been widely used in the field of organic devices for estimating the interfacial electronic structure.

2.2.1   Energy Level Alignment and Interfacial Electronic Structures

In many cases, the key mechanisms of polymeric electronics originate at interfaces – either at the electrodes or for example at borders of interpenetrating networks (e.g. in bulk-heterojunction OSC's). Some examples are shown in Figure 2-5 with schematic energy diagrams: a) shows an OLED (see also chapter 4.2) in which electrons (e) and holes (h) are injected from the electrodes into the electron transport layer (ETL) and hole transport layer (HTL), respectively. These carriers recombine to emit light, possibly in another emission layer. b) depicts spectral sensitisation in silver halide photography. In this process, an electron is photo-excited in an organic dye molecule

adsorbed on an Ag halide (AgX) surface, and is injected into the conduction band of Ag halide, leading to sensitisation. c) shows an OSC (see also chapter 4.3): Photo-formed electron-hole pairs in the organic layer are separated in the bent band region accompanied by the Schottky barrier. Thus, the explanation of the interfacial electronic structure is one possible approach for understanding and improving the performance of these devices. In particular, the organic/metal and organic/organic interfaces have attracted much interest in relation to the rapid development of the organic EL devices. In addition, metal/organic interfaces are important in the wiring of molecular devices. The subject of interfacial electronic structure can be roughly divided into two aspects: first the energy level alignment at the interface; and second, the band bending in a thicker region, as shown in Figure 2-5c). The former is important in carrier injection (e.g., in OLED's or spectral sensitisation), while the latter is essential for carrier separation (e.g., in a solar cell).
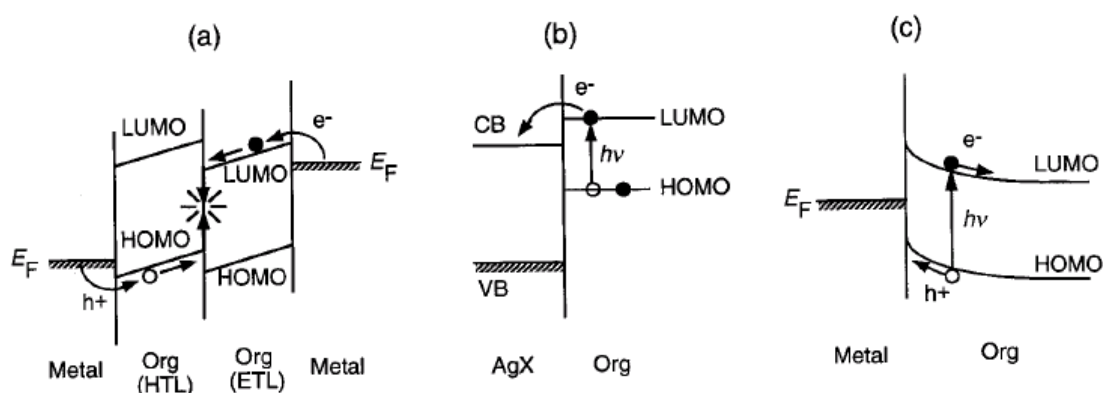
Figure 2-5: Energy diagrams of organic electronic devices with functions originating at interfaces.[35]
a) OLED consisting of an electron and a hole transport layer (ETL, HTL).
b) Spectral sensitisation in silver halide photography.
c) OSC using metal/organic Schottky barrier.

2.2.2   Vacuum Level

When an isolated electron is at rest in vacuum, it is said to be at the vacuum level (VL). The VL for an electron at rest at infinite distance from the system is often taken as an invariant energy reference, which is called vacuum level at infinite distance, and it is denoted as VL(∞). On the other hand, the VL of a solid involved in measurement of e.g. the work function corresponds to the energy of an electron at rest just outside the solid, and it is still affected by the potential of the solid. This vacuum level at surface is denoted as VL(s).

Thus, the experimentally determined VL is not that for an electron at infinite distance, and it cannot be used as an invariant reference level. There has often been misunderstanding about this point, with confusion between VL(s) and VL(∞). The effect of the solid on VL(s) is most convincingly demonstrated by the well-known dependence of the work function on the surface of a single crystal. For example, the work function of a tungsten single crystal is 4.63, 5.25, and 4.47 eV for the (100), (110), and the (111) surfaces.[36] Since the

Fermi level is a common level inside the solid, this dependence is due to the energy difference of an electron just outside of the solid, or VL(s).
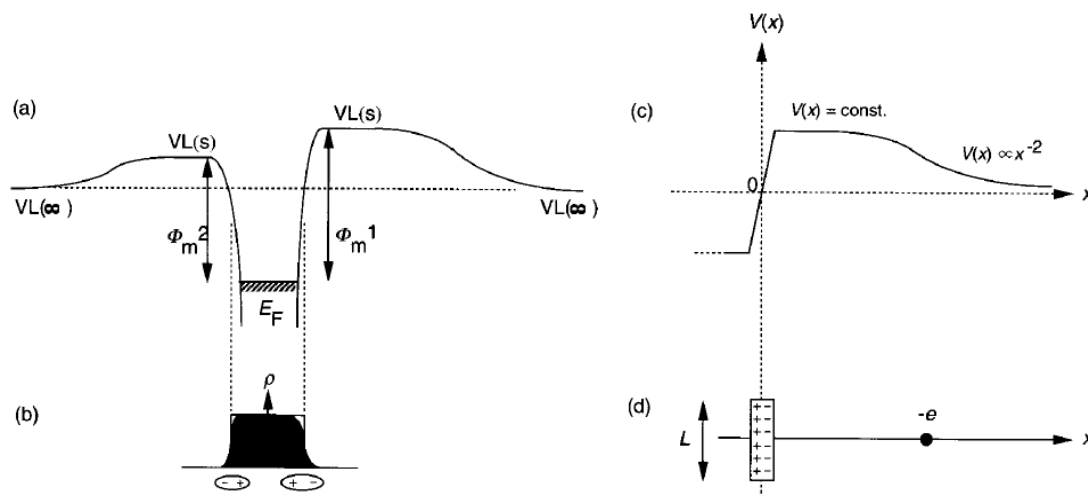
Figure 2-6: Vacuum level for a metal crystal[35]
a) Potential surface for an electron in and out of a metal crystal. E_F: Fermi level, VL(s): vacuum level at the surface, VL(∞): vacuum level at infinite distance, Φ_m: work functions of different crystal surfaces.
b) Electron density in the metal, with tailing at the surface to form a surface dipole layer. Note that the degree of tailing depends on the surface.
c) Electron and dipole layer with the distance x between them. The dipole layer has the representative extension L.
d) The potential energy of the electron by the dipole layer in (c).

For a metal, the difference between the energies of VL(∞) and VL(s) is mostly due to the surface dipole layer formed by the tailing of the electron cloud at the surface, as shown by the electron density distribution in Figure 2-6b). The tailing of the negatively charged electron cloud into vacuum makes the vacuum side negative, while the lack of electrons inside the surface makes the bulk side positive. For an electron at a distance x from a dipole layer of finite extension, with a representative length L (Figure 2-6d), the potential energy $V(x)$ by the dipole layer becomes as shown in Figure 2-6c). For a very small distance $x \ll L$, the dipole layer can be regarded to be infinitely extended. In such a case, the potential energy forms a step function across the dipole layer, and $V(x)$ at each side is independent of x. When the electron is separated from the dipole layer to make $x \gg L$, the dipole layer can be regarded as a point dipole, and the potential decreases. Such contribution from the surface dipole layer makes the potential energy for an electron in and out of a metal as shown in Figure 2-6a). The flat portion of the potential just outside the surface in Figure 2-6a) is the region of $x \ll L$. As the distance from the surface becomes larger than the extension of the sample surface ($x \gg L$), the effect of the surface dipole layer diminishes, and the energy of free electron gradually converges to a common value, which corresponds to VL(∞).

The dependence of the work function on the surface can be ascribed to the difference in the tailing of the electron cloud at different surfaces. For organic

solids, the existence of a surface dipole layer comparable to that of a metal surface has not yet been seriously examined by experiments. At least for solids formed by non-polar molecules, it can be speculated that it will not be so large for a free surface.

2.2.3   Interfacial Electronic Structure

An interface between the solids of two materials can be formed either by the contact of two solids or by the deposition of one material on the solid surface of the other. The studies of interfaces in these views have been developed rather separately in the fields of electronic devices and surface science, at least for organic molecules. In the following, the knowledge from these studies will be combined. Although a metal/organic interface will be primarily examined, the results can be easily extended to other types (organic/organic semiconductor, organic/inorganic semiconductor etc.) of interfaces, with appropriate cautions.
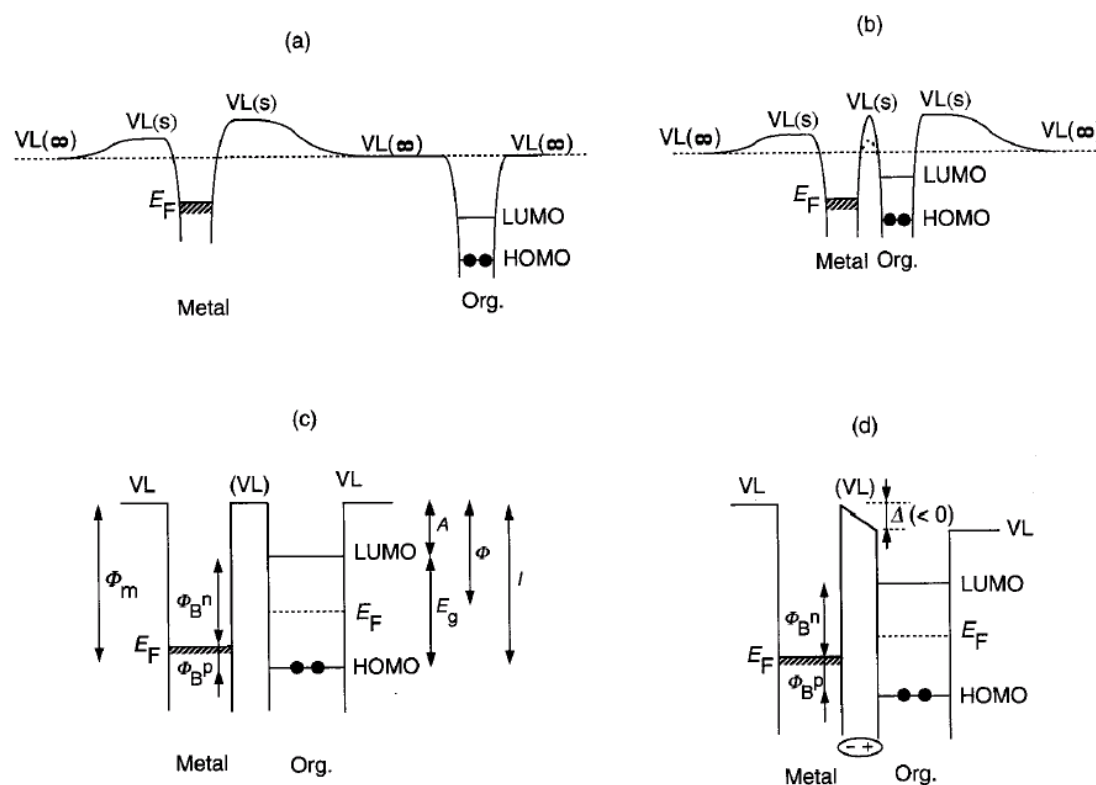
Figure 2-7: Energy diagrams[35]
a) Electronic structure of a metal and an organic solid at infinite distance.
b) Contact of a metal and a thin organic solid layer. The organic layer is within the electric field of the surface dipole layer of the metal, and the interfacial VL is common. When the two solids come into real contact, the actual potential well becomes as shown by the broken line.
c) Schematic representation of (a) assuming common (virtual) VL's at the interface. Φ_B^n and Φ_B^p denote the injection barriers for electrons and holes.
d) Interfacial energy diagram with a shift of VL Δ at the interface due to dipole layer formation. In this figure, the organic side is charged positive, making this side more comfortable (low energy) for an electron, and making the sign of Δ negative.

Figure 2-7a) and Figure 2-7b) illustrate the change in the potential well and the electronic states at the interface formation between a metal and an organic solid respectively. When a metal and an organic solid are far away, their energy levels are aligned sharing VL(∞), as shown in Figure 2-7a). When the solids come into contact without rearrangement of the electric charge, the organic layer is now in the potential of the surface dipole of the metal, and its energy levels are raised to have a common VL(s) in an extremely narrow interfacial gap, as shown in Figure 2-7b). In the actual contact, the two potential wells may be merged as indicated by the broken line, but it is often represented as shown by the solid line. In this sense, the vacuum level at the interface is a hypothetical concept to make the discussion easy. The situation in Figure 2-7b) is often represented as Figure 2-7c). Here the lines of VL(∞) are omitted, since the confusion between VL(s) and VL(∞) has been removed. In the actual systems, a dipole layer may be formed right at the interface, due to various origins such as charge transfer across the interface, redistribution of electron cloud, interfacial chemical reaction, and other types of rearrangement of electronic charge. We should recognize that this is an additional dipole layer, when there is already a dipole layer at the free surface as in the case of metal surfaces depicted in Figure 2-6b). With such interfacial dipole formation, there will be an abrupt shift of the potential across the dipole layer as shown in Figure 2-6d), leading to a shift of virtual VL Δ at the interface, as shown in Figure 2-7d). The value of Δ is determined by the magnitude of the dipole. This leads to the shift in VL in the organic layer at the right-hand side in Figure 2-7d) from that of the metal at the left-hand side.

On the other hand, this possible shift of the VL's is well known in the field of surface science at the adsorption and deposition of molecules on metal surfaces. It is usually called the change in the work function (or surface potential) of the metal, and extensive studies have been carried out for small molecules.[37] Following the common nomenclature, Δ will be positive when the VL is raised by deposition. In principle, controlled deposition in ultrahigh vacuum (UHV) is a convenient way to examine the interfacial electronic structure.[38] Unfortunately, most of such studies for organic compounds have been limited in the thickness region of sub-monolayer to several layers, and not much work has been carried out in interfaces with thicker organic layers, which can be regarded as solids. Also, most studies of the work function change were carried out for small molecules, and electronically functional large molecules have not been greatly examined, although there were some exceptions.[39-41]

2.2.4 Band Bending in the Organic Layer

For an interface with a thick organic layer, band bending should also be considered. In general, work functions for the metal and the organic layer are different, and the interfaces in Figure 2-7c) and Figure 2-7d) are not in electrical equilibrium, where the Fermi levels would be at the same energy. If the total number of the available mobile carriers in the organic layer is sufficiently large, there will be charge redistribution around the interface within a reasonably short time of an experiment. In the case of Figure 2-7c), for

example, the work function of the metal is larger than that of the organic layer, and the metal is more comfortable for an electron. As a result, some electrons may move from the organic layer to the metal, leading to the negative and positive charging of the metal and the organic layer, respectively. This charging makes the metal less comfortable for the negatively charged electron. Also, there may be a redistribution of mobile charge carriers in the organic layer. This flow and distribution of charge continues until the Fermi levels are aligned between the metal and the bulk of the organic layer. In such a redistribution of the charges, the potential distribution at the interfacial region is governed by the Poisson equation, which expresses the relation between the charge and potential distributions. As a result, a diffusion layer with band bending forms to align the Fermi energies of the two solids, with a built in potential in the organic layer.[42]

This corresponds to the work function and is shown in Figure 2-8a) and Figure 2-8b), for the cases with and without the interfacial dipole layer, respectively. The thickness of the diffusion layer W depends on factors such as V_{bi}, the dielectric constant of the organic layer ε, and the spatial distribution of the available donor or acceptor levels.

Such alignment of the Fermi level by band bending in Figure 2-8a) and Figure 2-8b) is possible only when a sufficient number of mobile charge carriers is available, either in a rather thick organic layer or organic layer with good semiconducting character. Such carriers may be available by extrinsic origin in polymers or materials under air, but are not expected in a thoroughly purified molecular layer prepared in inert atmosphere or even under UHV, since the HOMO-LUMO separation is usually much larger than the thermal energy. Thus for a very thin layer of molecular material in UHV, nearly-flat-band situations in the interfacial region are expected, as shown in Figure 2-7c) and Figure 2-7d), and the alignment of the Fermi level is not easily established (although there is a report that Fermi level alignment is achieved within 10 nm even for a molecular solid layer in UHV)[43] in the short time accessible in an experiment.
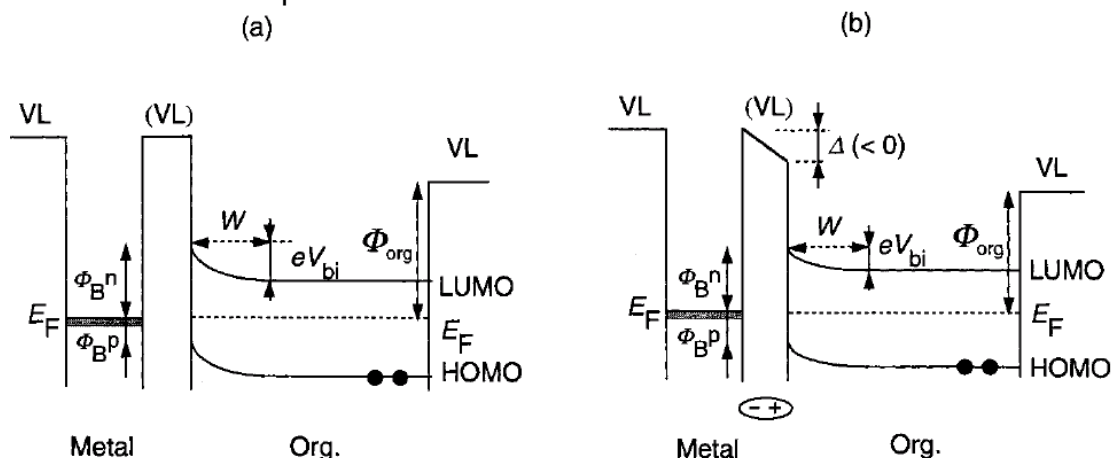
Figure 2-8: Interfacial energy diagram with band bending. The energy levels are bent by the charge redistribution in the organic layer to achieve the electrical equilibrium with the alignment of the Fermi levels of the two sides. This leads to the build-up of built-in potential V_{bi} within a diffusion layer of thickness W. a) and b) correspond to the cases without and with VL shift in Figure 2-7c and Figure 2-7d, respectively.[35]

2.2.5   Carrier Injection Barriers

In the cases of Figure 2-7c) and Figure 2-8a) without interfacial dipole layer formation, the (virtual) VL at the interface is common, and the barrier heights of carrier injection at the interface for holes and electrons comprise the Schottky-Mott rule, and correspond to the case of simple contact. When this rule applies, the barrier height can be deduced from the values of Φ_m (work function of the surface) and from the solid-state ionisation energy I determined by techniques like UV photoemission spectroscopy (UPS) or photoemission yield spectroscopy (PEYS).

$$\Phi_B^p = I - \Phi_m - \Delta \tag{2-1}$$

$$\Phi_B^n = \Phi_m - A + \Delta = E_g - \Phi_B^p \tag{2-2}$$

The injection barriers Φ_B^p and Φ_B^n for the case with interfacial dipole (Figure 2-7d and Figure 2-8b) are given by Equations (2-1) and (2-2), where the case of depositing organic layer on metal is considered (note that the sign of Δ is negative in Figure 2-7d) and Figure 2-8b). It is discernible that the injection barrier is modified from the simple expectation by Δ. This modification is critically important for applications using carrier injection, such as EL devices and spectral sensitisation in photography. We define the slope parameter S as:

$$S = \frac{d\phi_B^n}{d\phi_m} = -\frac{d\phi_B^p}{d\phi_m} \tag{2-3}$$

It is unity when the Schottky-Mott rule holds. It is also unity for the case with interfacial dipole layer, when Δ is independent of the metal. On the other hand, if Δ depends on Φ_m, S may deviate from unity. The deviation from unity has often been observed for inorganic semiconductors,[44] and is ascribed to the presence of interface states due to various intrinsic and extrinsic origins.[38,45-46] The values of S range from small (ca. 0.1) for covalent semiconductors like Ge and Si, to nearly 1 for ionic compound semiconductors.[44]

2.2.6   Practical Factors Affecting the Interfacial Electronic Structure

Attention should be called to at least two practically important factors in examining the actual interfaces including organics: 1) the possible chemical reaction and diffusion at the interface, and 2) the atmosphere under which the experiments are carried out.

The devices using organic materials are mostly formed by depositing thin layers using techniques such as vacuum deposition and spin coating. When the metal is deposited on an organic layer by evaporation, the high reactivity

of the vaporized hot metal atom often leads to a chemical reaction at the interface and it is also known that metal atoms may diffuse into the organic layer.[47] In such cases, the interface cannot be regarded as a simple contact between the metal and the organic layer. Instead, it should be considered as a third layer resulting from reaction and/or diffusion. This is important since the metal-on-organic system is used in the actual devices, e.g., at the last stage of fabrication of OLED's. In contrast, the situation is usually not as critical in the case of vacuum deposition of an organic layer on metal substrate, and the interfaces can be often prepared without much diffusion or chemical reaction.

The atmosphere of the sample fabrication and characterization can also affect the observed interfacial electronic structure. When the system is exposed to air or placed in low vacuum, the surface of many low work function metals can be oxidized, and adsorption or absorption of molecules like oxygen and water may occur for both the metal and the organic material. In the case of wet film preparation, such as spin coating, solvents may also remain in the organic film. The actual devices are usually fabricated under such conditions, and significant effects of atmosphere on various electric properties are known.[48-50] Further, the respective reactions across the conjugated polymer/metal interfaces have been examined (eg by UPS and XPS studies).[51-57] Together with the possibility of forming special forms of charge carriers, such as solitons, polarons, and bipolarons,[58] these factors make the fundamental studies of polymer interfaces rather complex. On the other hand, basic studies of the organic/metal interface can be more precisely carried out under UHV with in situ sample preparation. This can be performed for molecular material, which can be vacuum-deposited. The situation is more difficult for polymers, but oligomers can be used for such purposes.[51,55] In the comparison of these results with other experiments, care should be taken to match experimental conditions, and should take into account the possible effects of different atmospheres.

3 Experimental Background and Techniques

The electrical and optical properties of conducting polymers depend strongly on their current doping level. Experimental methods for the determination of corresponding properties will be treated in this chapter.

3.1 Voltammetry

Voltammetry can be defined as a group of electrochemical techniques in which a potential is applied to an electrochemical cell with the simultaneous measurement of the resulting current. By varying the potential of an electrode, it is possible to oxidize and reduce species that exist in solution. At more positive potentials, the electrons within the electrode become lower in energy and the oxidation of species in solution becomes more likely. At lower potentials, the electrons become higher in energy and the reduction of solution species becomes more likely. By monitoring the current of an electrochemical cell at varying electrode potentials, it is possible to determine several characteristics of the solution species such as concentration, reaction kinetics, thermodynamic parameters and so forth.

The main principle of voltammetry is that most of the reactions, which take place in the electrochemical cell, occur close to the electrode surface. Thus, it is important to understand the relationship between the concentration of species at the electrode surface and electrode potential. Considering an electrode at equilibrium with the solution it is in, the electrode will exhibit a constant potential, which is thermodynamically related to the composition of the solution. Assume the solution contains a species A, which is capable of being reduced to B at the electrode surface. If the electrode potential were changed by external means, the current in the electrode circuit would change the composition of the solution in such a way as to account for the new potential. The Nernst equation relates the electrode potential to the concentration of species at the electrode surface:

$$E = E^0 + \frac{RTF}{n} log\left(\frac{c_A}{c_B}\right)$$

(3-1)

where

- E applied electrode potential,
- $E°$ formal reduction potential of solution species,
- R Rydberg constant,
- T Temperature,
- F Faraday constant,
- n number of electrons transferred in reaction,
- c_A <u>surface</u> concentration of species A, and
- c_B <u>surface</u> concentration of species B (reduced A).

This relationship is true for systems in which the electrode reaction is rapid in both directions (a reversible system). For a hypothetical system where n = 1 and $E° = 0$ V, c_A would equal c_B when $E = 0$ mV, i.e., when the electrode is at equilibrium with the solution. High concentrations of species A are favoured when $E > E°$, while high concentrations of species B are favoured when $E < E°$. Changes in the electrode surface concentrations of A and B caused by the applied electrode potential creates a concentration imbalance between the solution at the electrode surface and the solution in the remainder of the cell. Mass transfer mechanisms such as diffusion and convection counteract this imbalance by moving species from regions of high concentration to regions of low concentration.

In cyclic voltammetry, the potential of an electrode in solution is cycled while the resulting current is measured. The potential of this working electrode varies with time and is controlled versus a reference electrode (e.g., Ag/AgCl). The potential between these two electrodes can be thought of as an excitation signal, which will change the species in solution. Cycling of the potential yields a linear potential scan with a triangular waveform. The electrode potential is cycled between two values of E known as switching potentials. When the electrode potential reaches one of these values, the signal reverses direction and scans until the other switching potential is reached, at which point the cycle repeats.

A cyclic voltammogram is obtained by measuring the current produced at the working electrode during the potential scan. The current, which is produced, can be thought of as the cell's response to the change in electrode potential. In a voltammogram the current is plotted against the potential.

Cyclic voltammetry can be utilized to characterize the redox-active range of a conducting polymer, i.e., the characterization of the range, in which a polymer can be doped electrochemically. In case of polymer deposition on the working electrode solid-state reactions make a precise determination of mechanistic aspects difficult. Structural changes during charging can take place, which can change the cyclic voltammogram significantly.

Solution electrochemistry allows to separate pure redox processes from morphological ones by eliminating the latter. However these solid state effects are important in some cases, especially in practical applications such as in electronics. Unlike low-molecular, redox-active materials *thin polymer films* are not expected to have an exactly defined redox potential, but a broad range of redox-states. The reason for this assumption is the fact that polymers are not uniform, but that they consist of chains of different isomers, lengths and conformations. Additionally it has to be assumed that the conjugation is disturbed on a single polymer chain, which causes a broad distribution of effective conjugated polymer segments.

If the working electrode is covered with a thin polymer film changes of the cyclovoltammogram have to be considered. First a certain potential drop across this film can occur, i.e. the potential applied to the cell is not

necessarily the voltage between the electrodes. Nevertheless, potential shifts in general can be minimized by using a three electrode cell in which the reference electrode measures the static potential rather than a potential which is influenced by the amount of current. In addition charges which are needed for the oxidation and reduction of the *whole* film have to be considered. They scale with the film thickness if scan speeds are sufficiently low and if counter ions can penetrate the film. This point is very important during electropolymerization since in this case film thickness increases with time..

Figure 3-1 shows a typical cyclic voltammogram of a PEDOT film, here atop the Pt work electrode in acetonitrile with tetrabutylammonium hexafluorophosphate (TBAPF$_6$, 0.1 M). The electrochemical potential of the oxidation (0.12 V) and the reduction (-0.4 V) peak are clearly discernible. The electroactive area ranges from potentials of E_{eq} = -0.75 V where the current is zero (no electrochemical activity) on the left up to values for E_{eq} higher than 1.25 V since there are still electroactive states ($I \neq 0$). The upper limit is given by damaging oxidation. Another limiting factor for boundaries is a possible reduction or oxidation of the supporting solvent. Therefore, the solvent has to be selected with care.
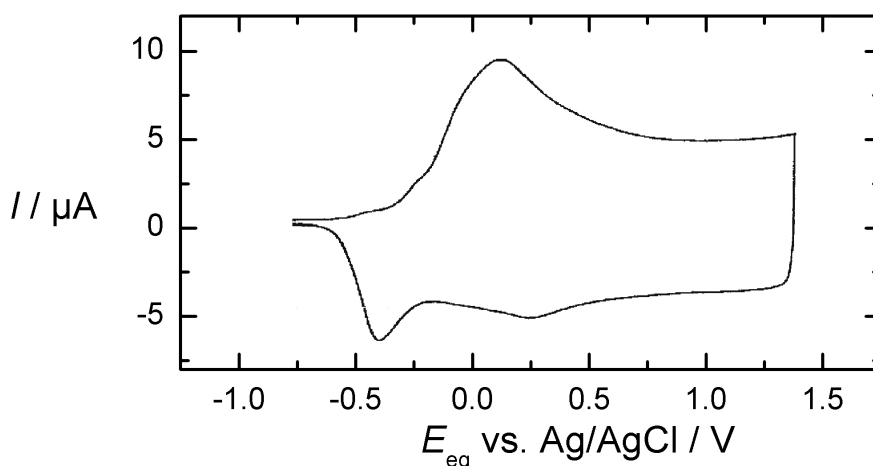
Figure 3-1: Cyclic voltammogram of PEDOT. The electrochemical potential of the first oxidation (0.12 V) and first reduction (-0.4 V) peak are clearly discernible. The electroactive area ranges from E_{eq} = -0.75 V (no electrochemical activity) on the left up to values for E_{eq} higher than 1.25 V. The boundary for the right side is given by chemical damage of the polymer, which occurs for high potentials.

3.2 UV-Vis Spectroscopy

Ultraviolet-visible spectroscopy (UV = 200-400 nm, visible = 400-800 nm) measures electronic excitations between the energy levels that correspond to the molecular orbitals of the systems. In particular, transitions involving π orbitals and lone pairs are important and so UV-Vis spectroscopy is of most use for identifying conjugated systems, which tend to have sufficient absorptions.

Luminescence is the emission of light by a substance. It occurs when an electron returns to the electronic ground state from an excited state and loses its excess energy as a photon. The absorption and emission of electromagnetic radiation is associated with changes in energy states of the species. UV-Vis spectrophotometry uses ultraviolet and visible electromagnetic radiation to energetically promote valence electrons in a molecule to an excited energy state. The UV-Vis spectrophotometer then measures the absorption of the energy to promote the electron by the molecule at a specific wavelength or over a range of wavelengths.

The amount of electromagnetic radiation absorbed by a species in a solution (A) depends on its concentration (c), the path length of the electromagnetic radiation (d), and the specific molar absorptivity (ε) of the species. This is defined as Beer-Lambert's Law:

$$A = \varepsilon\,dc$$ (3-2)

The absorption of energy also depends upon the intensity of the incident light, P_0, and the intensity of the exiting electromagnetic energy, P, where

$$A = \log\left(\frac{P_0}{P}\right).$$ (3-3)

Luminescence spectroscopy is a collective name given to three related spectroscopic techniques. They are:

- Molecular fluorescence spectroscopy,
- Molecular phosphorescence spectroscopy, and
- Chemiluminescence spectroscopy.

The electronic states of most organic molecules can be divided into singlet states and triplet states as exemplarily shown in Figure 3-2. For a singlet state all electrons in the molecule are spin-pairs, whereas for triplet states one set of electron spins is unpaired.
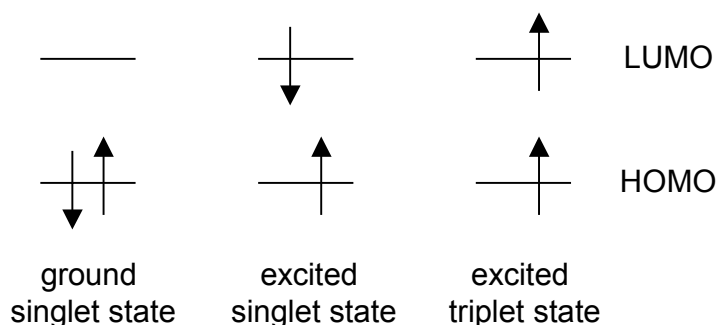
Figure 3-2: Simplified sketch of electronic states of most organic molecules. Singlet state: All electrons in the molecule are spin-paired. Triplet state: One set of electron spins is unpaired.

27

Absorption of UV radiation by a molecule excites it from a vibrational level in the electronic ground state to one of the many vibrational levels in the electronic excited state. This excited state is usually the first excited singlet state. A molecule in a high vibrational level of the excited state will quickly fall to the lowest vibrational level of this state by losing energy to other molecules through collision. The molecule will also partition the excess energy to other possible modes of vibration and rotation. Fluorescence occurs when the molecule returns to the electronic ground state, from the excited singlet state, by emission of a photon. If a molecule, which absorbs UV radiation, does not fluoresce it means that it must have lost its energy some other way. These processes are called radiationless transfer of energy.
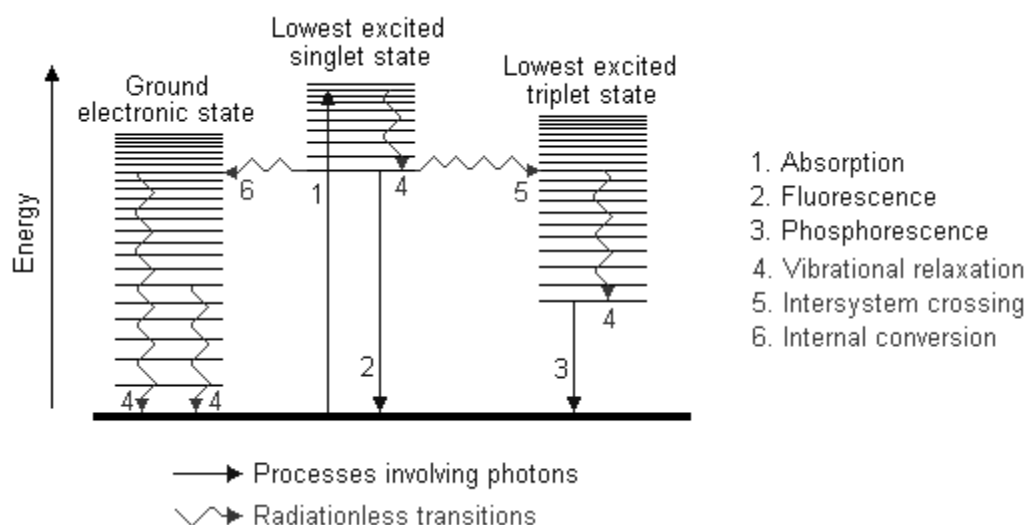
Figure 3-3: Possible physical process following absorption of a photon by a molecule. During fluorescence or phosphorescence electrons are transferred into *one out of several* vibrational states of the ground electronic state (simplified in this sketch).

By intra-molecular redistribution of energy between possible electronic and vibrational states the molecule can also return to the electronic ground state. The excess energy is converted to vibrational energy (internal conversion), and so the molecule is placed in an extremely high vibrational level of the electronic ground state. This excess vibrational energy is lost by collision with other molecules (vibrational relaxation). The conversion of electronic energy to vibrational energy is favoured, if the molecule is "flexible", because it can reorient itself in ways, which aid the internal transfer of energy.

A combination of intra- and intermolecular energy redistribution takes place when the spin of an excited electron is reversed, leaving the molecule in an excited triplet state; this is called intersystem crossing. The triplet state is of a lower electronic energy than the excited singlet state. The probability of this happening is increased if the vibrational levels of these two states overlap. For example, the lowest singlet vibrational level can overlap one of the higher vibrational levels of the triplet state. A molecule in a high vibrational level of the excited triplet state can lose energy in collision with solvent molecules, leaving it at the lowest vibrational level of the triplet state. It can then undergo

a second intersystem crossing to a high vibrational level of the electronic ground state. Finally, the molecule returns to the lowest vibrational level of the electronic ground state by vibrational relaxation.

A molecule in the excited triplet state may not always use intersystem crossing to return to the ground state. It could lose energy by emission of a photon. Due to the selection rules for electronic transitions the triplet/singlet transition is much less probable than a singlet/singlet transition. The lifetime of the excited triplet state can be up to 10 seconds, in comparison with 10^{-5} s to 10^{-8} s average lifetime of an excited singlet state. Emission from triplet/singlet transitions can continue after initial irradiation. Internal conversion and other radiationless transfers of energy compete so successfully with phosphorescence that it is usually seen only at low temperatures or in highly viscous media.

Chemiluminescence occurs when a chemical reaction produces an electronically excited species, which emits a photon in order to reach the ground state. This sort of reactions can be encountered in biological systems; the effect is then known as bioluminescence. The number of chemical reactions, which produce chemiluminescence, is small. However, some of the compounds, which do react to produce this phenomenon, are environmentally significant.

3.3   Kelvin Probe

The Kelvin probe (see sketch in Figure 3-4) is a non-contact, non-destructible vibrating capacitor device used to measure the work function difference of its electrodes.

The work function is the least amount of energy required to remove an electron from the surface of a conducting material, to a point just outside the bulk with zero kinetic energy (see Figure 2-6). The first Kelvin Probe method was postulated by the Scottish scientist W. Tompson, in 1861.
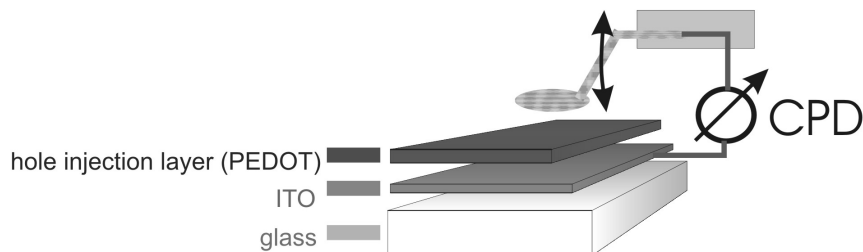
Figure 3-4: Kelvin probe measurement above material of interest (here: pre-adjusted PEDOT film). The AC-voltage caused by a vibrating gold grid (reference) is compensated by a lockin-amplifier, the resulting compensation voltage is the contact potential difference (*CPD*), which correlates directly to the difference in work function of the capacitor electrodes (PEDOT and reference).

The Kelvin Probe method consists to create a simple capacitor between a flat circular electrode and the specimen. Figure 3-5 shows various electron energy diagrams for two conducting specimens.
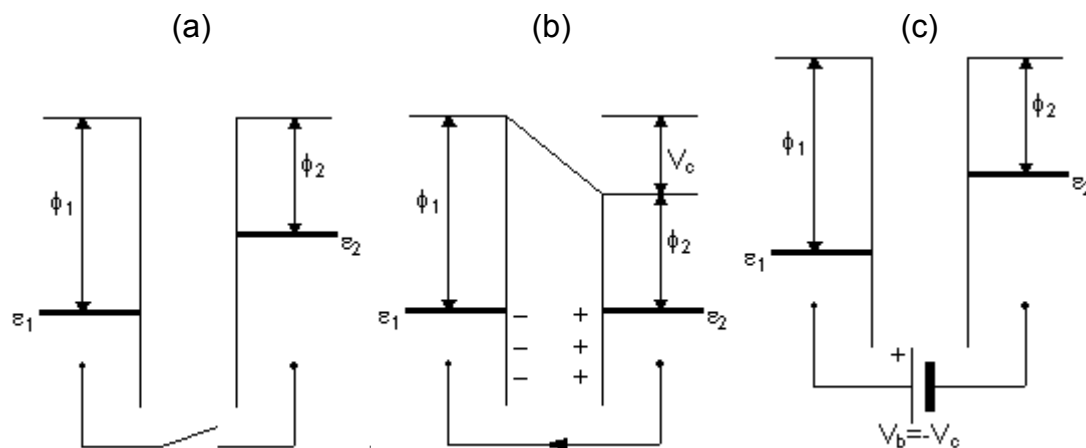
Figure 3-5: Electron energy level diagrams of two different metals (a) without contact, (b) with external electrical contact, and (c) with inclusion of the backing potential V_b.

ϕ_1 and ϕ_2 are the work functions of the materials, ε_1 and ε_2 represent their Fermi levels. In the Figure 3-5b), the two electrodes equalize their Fermi levels and the two surfaces become equally and oppositely charged. In Figure 3-5c), one electrode is biased with respect to the other by applying an external backing potential V_b. This method is used to find the work function difference between two surfaces. At the unique point where the electric field between the plates vanishes, the backing potential V_b equals the negative charge potential V_c. The respective V_b is called contact potential difference (*CPD*). In order to generate flow of charge which is not ebbing away we used a vibrating tip to change the capacity and thus allow the renewal of the charge flow.

3.4 Atomic and Electrostatic Force Microscope (AFM and EFM)

By scanning a Kelvin probe tip in two dimensions across a surface it is possible to obtain a two-dimensional map of the *CPD* with a lateral resolution of a few nanometers. An electrostatic force microscope (EFM/AFM) enables simultaneous imaging of topography and *CPD*.

Every line of the scan field is scanned twice. On the first pass (Figure 3-6) the sample topography is measured by a vibrating tip, i.e., the cantilever is physically vibrated near its resonant frequency by a small piezoelectric element. A laser beam is deflected from the cantilever. The deflection is detected by a quad photo detector arrangement, which enables AFM (height) and LFM (lateral force) measurements simultaneously.
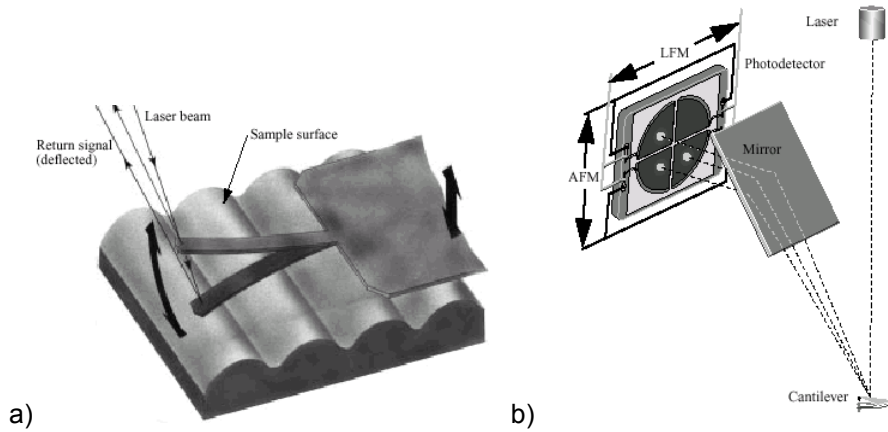
Figure 3-6: [59] Principle setup of an AFM: A laser beam is deflected from the cantilever. The deflection is detected by a quad photo detector arrangement. This arrangement enables AFM (height) and LFM (friction) measurements simultaneously.
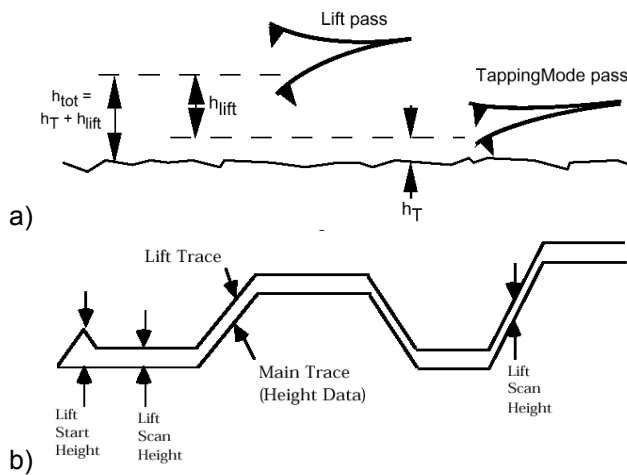
Figure 3-7: [59] Principle of an AFM with an additional EFM modus.

On the second pass on the same line (Figure 3-7), the scan height h_{tot} is kept constant which is realized by using the height information h_T from the first pass adding a certain distance. The piezo that normally vibrates the cantilever is turned off. Instead, in order to measure the surface potential, an oscillating voltage with the natural frequency of the cantilever is applied directly to the tip. This creates an oscillating electrostatic force with the frequency ω. The oscillating force F has the following amplitude:

$$F = \frac{dC}{dz} V_{dc} V_{ac}$$ (3-4)

where dC/dz is the vertical derivative of the tip/sample capacitance,

31

$$V_{dc} = V_{tip} - V_{sample} \text{,} \tag{3-5}$$

the dc voltage difference between the tip and the sample and V_{ac} is the amplitude of the oscillating voltage applied to the cantilever tip.

The key here is that the force on the cantilever depends on the product of the ac drive voltage and the dc voltage difference between the tip and the sample. And, when the tip and sample are at the same dc voltage (V_{dc} = 0), the cantilever will feel no oscillating force. An external electronic module uses this fact to determine the effective surface potential on the sample, V_{sample}. The external module determines the local surface potential by adjusting the dc voltage on the tip, V_{tip}, until the oscillation amplitude becomes zero. At this point the tip voltage will be the same as the local surface potential. The voltages applied to the cantilever tip V_{tip} are recorded and merged to a surface potential "image" later on.

It is noteworthy that the principle of the Kelvin probe measurement is slightly changed for the EFM. Due to the small currents caused by just a few atoms at the EFM tip (instead of a grid), a current compensation akin the classical Kelvin probe measurements is insufficient for the *CPD* determination. Therefore, the voltage compensation is controlled by the deflection of the laser beam rather than by a current measurement.

The same sample area can be measured from different directions. The accuracy of a measurement can be evaluated by using different scan angles. A scan angle of 0° corresponds to scanning from the top to the bottom, a scan angle of 90° corresponds to scanning from the left to the right and so on. If images scanned from different directions are identical artefacts like tip effects can be excluded.

3.5 Photovoltaic and Spectral Response Measurements

Another way of work function difference determination is a photovoltaic measurement. Instead of vibrating a reference above the material of interest (Kelvin probe) a photosensitive layer is deposited on top and a metal "reference" is evaporated at last. When the photosensitive polymer is excited by illumination the generated charge carriers travel in the electrical field given by the difference in work function of the material of interest and the reference. Therefore, an external voltage, called open circuit voltage, can be measured which allows the determination of the work function. Photovoltaic properties, which come into play in this thesis, are described in chapter 4.3.3 in detail.

Photovoltaic measurements are performed at one certain incident wavelength (e.g. laser) or with a fixed spectrum (e.g., from a sun light simulator). Similar to UV/Vis measurements, it is interesting to obtain a wavelength resolved photocurrent $I(\lambda)$. The spectral resolution of the photocurrent is called spectral response or photoaction spectrum. This spectrum allows to detect photo physical characteristics of the devices like filter effects for instance.

4 Technological Background

4.1 Hole Conducting Electrode

For polymeric devices which combine electronics with optics, e.g. OLED's or OSC's, at least one transparent electrode is desired in order to couple light into or out of the device. This specification is fulfilled for thin semitransparent metal layers or other transparent layers with similar properties.

4.1.1 Indium Tin Oxide (ITO)

In the early years of polymer electronics scientists used indium tin oxide as the hole injecting layer (anode). But beside the advantages of outstanding conductivity and optical transparency ITO had also a few disadvantages. ITO has the strong ability to shorten the life time of organic semiconducting devices[63] and it has a comparatively rough surface, which leads to an inhomogeneous *E*-field in the devices. The Root Mean Square (RMS) roughness is the standard deviation of the Z values within a given area:

$$RMS = \sqrt{\frac{\sum_{i=1}^{n}(Z_i - Z_{average})^2}{N}}$$

(4-1)

The RMS for ITO used in this thesis is about 10 nm but single spikes, which limit the device performance, are taller than 40 nm.

a)   b)
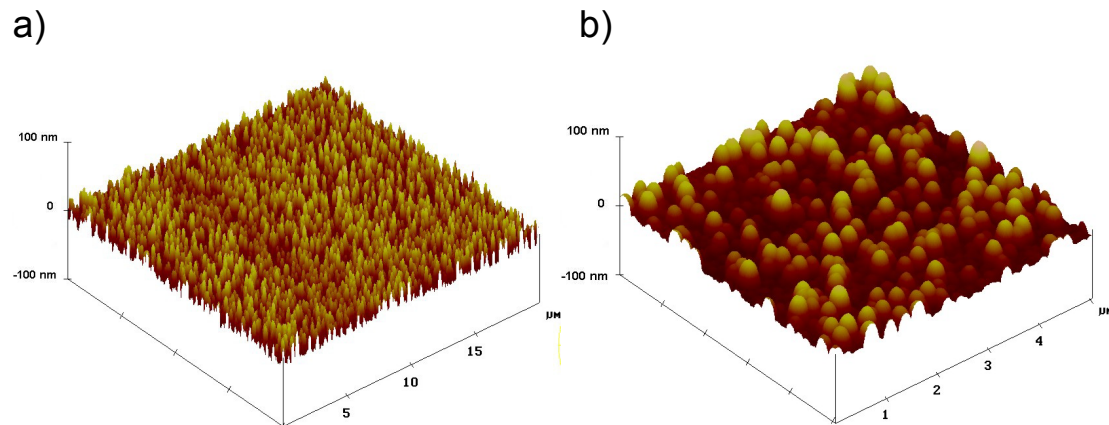
Figure 4-1: AFM images (contact mode) of the ITO used throughout this thesis. The z-range ranges from –100 nm to +100nm in both images; the scan field is 20 x 20 µm (a) and 5 x 5 µm (b). Single spikes are higher than 40 nm.

Furthermore, ITO has an ill-defined work function and, therefore, it causes an unpredictable hole injection. Thus, optimization of these devices was required.

4.1.2   Polymeric Anodes

By covering the ITO layer with CuPc or p-type conducting polymers, e.g., PEDOT, the properties of the devices could be enhanced. The surface is smoothened (Figure 4-2), the diffusion of lifetime limiting ITO particles is blocked, and a roughly predictable hole injection could be achieved.
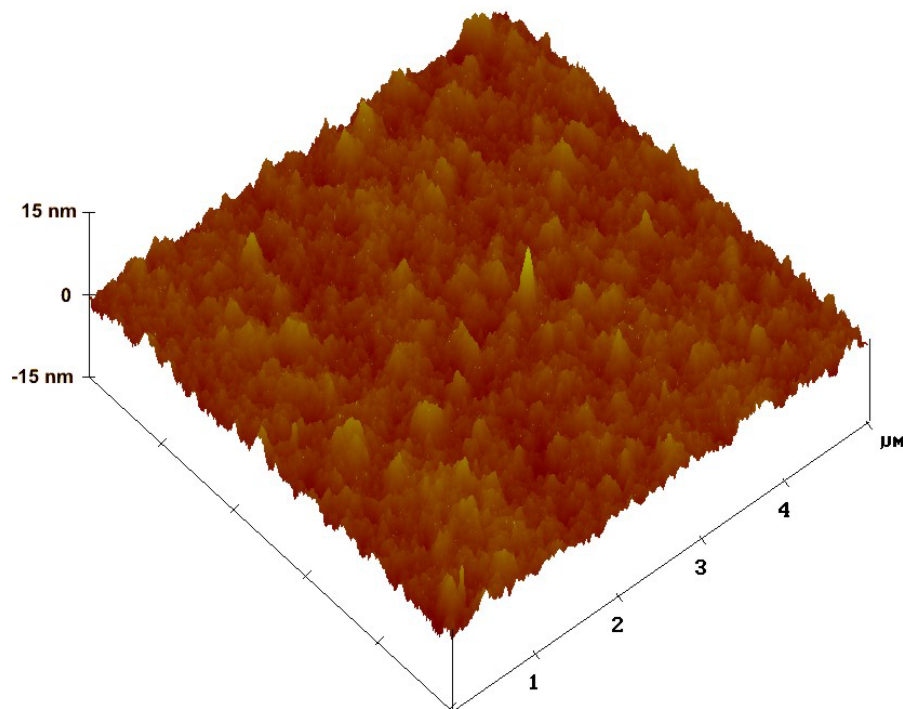
Figure 4-2: Tapping mode AFM image of a PEDOT film spin coated onto the surface of ITO (Figure 4-1). The total colour-range covers 15nm. The RMS is below 4nm.
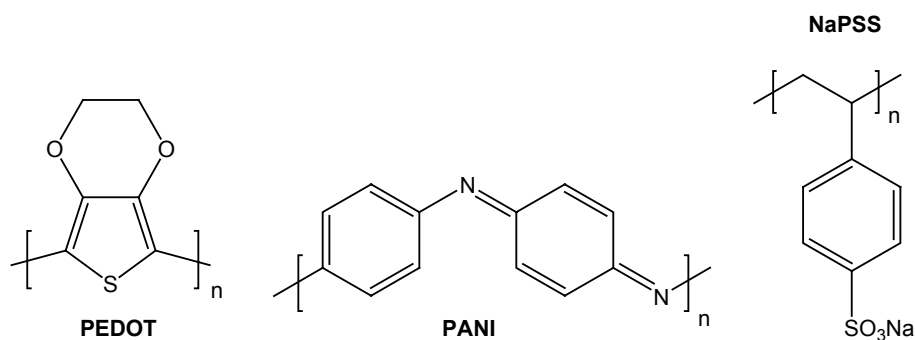
Figure 4-3: Materials often used as hole injection layer: Poly-3,4-ethylenedioxythiophene (PEDOT) and polyaniline (PANI); these p-type conducting polymers can be doped with counterions like poly(styrene sulfonate) (PSS⁻), here the sodium salt (NaPSS) is displayed.

4.1.3   Electrochemical Deposition and Doping of PEDOT

Usually PEDOT (poly-3,4-ethylenedioxythiophene, Figure 4-3) as the mostly used hole conducting material is spincoated from suspension forming a thin

film of about 40 nm. For our investigations we used the same polymer but instead of spin casting from solution we polymerized PEDOT electrochemically from its monomer EDOT.

As shown in Figure 4-4 the polymerization is started by an anodic oxidation of the monomer EDOT. After dimerization of two radical cations and after splitting off of two protons bithiophene is formed. Oligomers can be formed successively by further coupling (anodic oxidation of the bithiophene etc). The reactivity and solubility are decreasing with increasing chain length. After a certain chain length is reached the polymer is deposited onto the anode. The degree of polymerisation is determined by the applied electrochemical potential since the reactivity decreases due to an enhanced stabilisation of positive charges with an increasing chain length. Remaining positive charges on the chain are compensated by PSS⁻ counterions, which are incorporated into the film. This incorporation leads to an oxidized film after finishing the potentiostatic electropolymerisation.
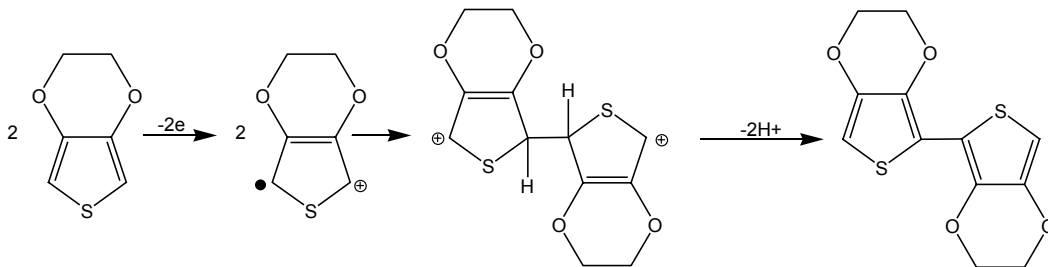
Figure 4-4: Dimerization mechanism of 3,4-ethylenedioxythiophene (EDOT).

Films of electrochemically deposited polymers are mechanically more stable than their spincoated counterparts and therefore better suited for the following doping treatment. In principle doping of conducting polymers is realized by oxidation or reduction of the polymer chain. Besides other possible techniques electrochemical doping is the most reliable alternative due to its unique ability to measure the resulting electrochemical potential E_{eq} as an evaluation.

During the doping process of PEDOT films the charges are provided from the anodic contact on which they are deposited – they are actually even part of the anode. Depending on the process (doping or dedoping) the counter ions penetrate into or leave the film. The doping level of the polymer is correlated to the electrochemical (equilibrium) potential, which can be measured between the reference and the working electrode.

In the redox-active range of a conductive polymer, which is discernible from the respective cyclic voltammogram (compare Figure 3-1), a certain doping level can be adjusted by applying a certain voltage to the work electrode until the system reaches its equilibrium. This status is reached when the current gets zero, i.e., charging processes are completed.

Initially it has been neglected that a shift of the Fermi level should be expected on varying the doping level.[64] Because this parameter is of utmost importance for the electrical properties and, generally, for the performance of

electronic devices, the knowledge of the Fermi level as a function of the doping level is a necessary condition for the utilization of these materials.

4.2 Organic Light Emitting Diodes (OLED)

Electroluminescence – the generation of light, other than blackbody radiation, by electrical excitation – is a phenomenon that has been seen for a wide range of semiconductors, and for organic semiconductors it was first seen in the 1960s.[3,4]

Organic light-emitting diodes (OLED's) represent a promising technology for innovative products such as displays in all kinds of portable electronic devices such as cellular phones and personal assistants.[68-69]

4.2.1 Basic Materials and General Structure of OLED's

Thin polymer layers can be produced by spin coating from solution. In addition big areas can be coated by techniques called "dip coating" or "doctor blading". Commonly used polymers are PPV- and PPP-derivatives and appropriate co-polymers, which exhibit a sufficient brightness and efficiency.[70]

Basic molecular structures of two basic electroluminescent polymers are shown in Figure 4-5.
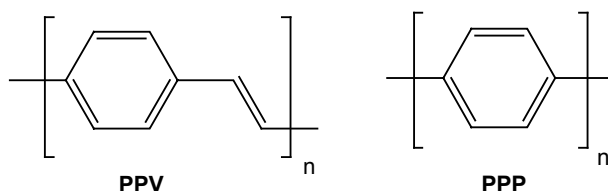
Figure 4-5: Chemical structure of electroluminescent polymers: poly(p-phenylene vinylene) (PPV), poly(p-phenylene) (PPP).

Although monochromic operation, which is enabled by these polymers, is sufficient for some applications, the extension to multi-colour devices does greatly enhance their technological impact. Multi-colour OLED's have been successfully fabricated by vacuum deposition of small electroluminescent molecules, but solution processing of larger molecules (electroluminescent polymers) results in a cheaper and simpler manufacturing process. However, it has proven difficult to combine the solution processing approach with the high-resolution patterning techniques required to produce a display. Recent attempts have focused on the modification of standard printing techniques,[71-73] but those still have technical drawbacks. A new class of electroluminescent polymers with oxetane sidegroups that can be cross-linked photochemically can be patterned in a way similar to standard photoresist materials.[74] These are soluble polymers utilized to produce insoluble polymer

networks in desired areas. The resolution of the process is sufficient to fabricate matrix displays.

Electroluminescence from conjugated polymers was first reported in 1990,[15] using poly(p-phenylene vinylene), PPV, as the single semiconductor layer between metallic or polymeric electrodes. Figure 4-6 illustrates a device structure with a PEDOT layer serving as the anodic contact. In this structure, the ITO layer functions as a transparent electrode, and allows the light generated within the diode to leave the device. The top electrode is conveniently formed by thermal evaporation of a metal. LED operation is achieved when the diode is biased sufficiently to achieve injection of positive and negative charge.
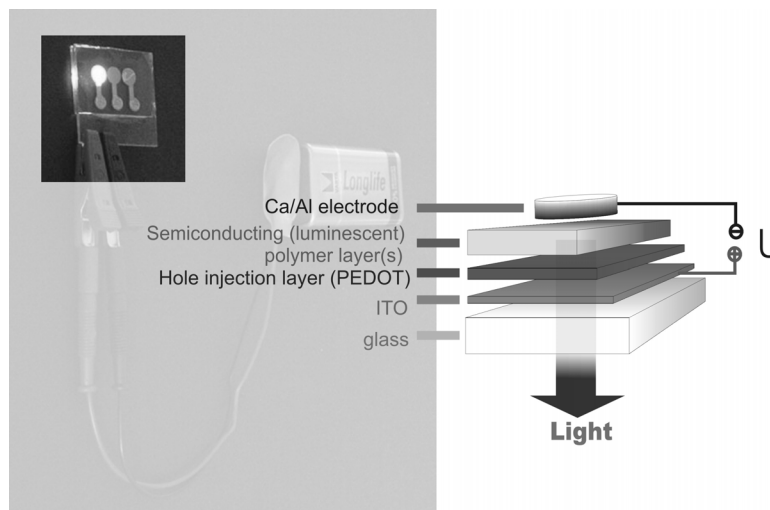
Figure 4-6: Sketch of an organic light-emitting device (OLED). The transparent anodic contact (ITO/PEDOT) is followed by the electroluminescent polymer and at last the cathodic metal contact.

4.2.2   Electrodes and Injection Barriers

The electrodes play an important role for the device performance. They are in direct contact with the adjoining semiconducting polymer layer. Accordingly, electrons and holes have to overcome certain energy barriers before they are injected into the electroluminescent polymer layer. Lowered energy barriers are of high technological interest, since high barriers cause a limitation in current and a corresponding high operation voltage, which is in contradiction to battery powered portable devices.

For a vanishing injection barrier, the highest possible current throughput, called space charge limited current (SCLC), is achieved. SCL currents are typically different for different charge carriers, e.g. due to different charge carrier mobilities and/or space charge fields. But in order to reach the highest efficiency charge carrier densities have to be balanced (see chapter 4.2.3). Therefore, it is often better to have a certain barrier for the major sort of charge carrier, which causes an injection-limited current (ILC) appropriate to the initial minor sort of charge carriers. Intuitively, balanced currents should

cause a recombination efficiency close to an optimum. Theoretical consideration in this thesis will confirm this assumption.

4.2.3   Recombination and Efficiency

After the charge carriers have been injected into the electroluminescent polymer _charge transport_ plays an important role. Since charge transport is not only crucial for OLED's, but for conductive polymers in general, it has already been described in Chapter 2.

For an efficient electroluminescence it is essential to have balanced hole and electron current densities. Different injection barriers and different mobilities of charge carriers lead to preconditions, which can be optimized. Since the mobilities are given by the electroluminescent material and cannot be optimized easily, the adjustment of the injection barriers is the key approach for an enhanced efficiency.

Experimentally the efficiency η can be determined by measuring the IV-curves and the respective light output of a device. Thereafter η can be calculated and expressed in the common properties Candela per ampere (Cd/A) or lumen per Watt (lm/W).

The measured total quantum yield η_{tot} (dimensionless), which is the number of emitted photons divided by the total amount of electrons, consists of at least 5 contributions:

$$\eta_{tot} = \eta_{rec}\eta_{S/T}\eta_{PL}\eta_{out}\eta_{prep} \tag{4-2}$$

The ratio of probabilities for the formation of singlet and triplet states is given by $\eta_{S/T}$, η_{PL} is the probability for a radiative decay, η_{out} is the amount of light which can be outcoupled out of the device (considering for example wave guide losses), and η_{prep} is the variation which is due to different preparation conditions. The recombination quantity yield η_{rec} (nondimensional) represents the probability of a charge carrier to meet its counterpart forming an exciton. Keeping the other contributions constant the recombination efficiency η_{rec} (physical property) can be used to evaluate an improved injection barrier.

The following simple considerations (based on Bäßler's assumption of a bimolecular reaction between holes and electrons inside the electroluminescent layer of an OLED)[115] are helpful to achieve a correlation between the current densities of the respective charge carriers and the recombination efficiency η_{rec}. The result will be utilized in chapter 5.2.3.

The volume density of charge carriers is

$$n = \frac{j}{e\mu E} \qquad \text{(4-3)}$$

and a bimolecular reaction yields the following recombination rate:

$$\frac{dn}{dt} = \dot{n}_h = \dot{n}_e = -\gamma\, n_h n_e = -\gamma \frac{j_h j_e}{e^2 \mu_h \mu_e E^2}, \qquad \text{(4-4)}$$

which consists of the bimolecular recombination rate constant:

$$\gamma = 4\pi \langle R \rangle (D_h + D_e) \qquad \text{(4-5)}$$

with respective diffusion constants for holes and electrons

$$D = \frac{\mu kT}{e} \qquad \text{(4-6)}$$

and an interaction distance between electrons and holes of

$$\langle R \rangle = r_c = \frac{e^2}{\left(4\pi\varepsilon\varepsilon_0 kT\right)}. \qquad \text{(4-7)}$$

Replacing D and $<R>$ in Equation (4-5) yields

$$\gamma = 4\pi \frac{e^2}{4\pi\varepsilon\varepsilon_0 kT} \frac{kT}{e} (\mu_h + \mu_e) = \frac{e}{\varepsilon\varepsilon_0} (\mu_h + \mu_e). \qquad \text{(4-8)}$$

Since the mobility of electrons μ_e can be neglected compared to the hole mobility μ_h in PPV derivatives Equation (4-8) can be approximated by

$$\gamma = \frac{e}{\varepsilon\varepsilon_0} \mu_h. \qquad \text{(4-9)}$$

Now, γ in Equation (4-4) can be replaced:

$$\frac{dn}{dt} = -\frac{e}{\varepsilon\varepsilon_0} \frac{j_h j_e}{e^2 \mu_e E^2} \qquad \text{(4-10)}$$

The efficiency can be calculated in terms of the number of bimolecular reactions (dn_h/dt) divided by the total number of injected charge carriers (j_h+j_e)/ed:

$$\eta_{rec} = \frac{\dot{n}_h ed}{j_h + j_e} = -\frac{1}{\varepsilon\varepsilon_0}\frac{j_h j_e}{\mu_e E^2}\frac{d}{j_{ges}} = \frac{d}{\varepsilon\varepsilon_0 \mu_e E^2}\frac{j_h j_e}{j_{ges}}$$

(4-11)

Thus, the efficiency can be easily calculated by multiplying the current contributions of holes and electrons, if the total current density j_{ges} is kept constant.

An influence of a changing voltage cannot entirely be excluded. However, it is negligible, if the used electric fields are larger than 3.6 V per 100 nm.[75] This efficiency levelling for higher fields was clearly demonstrated by Blom et al. for dialkoxy-PPV (similar to the PPV-derivative used in this thesis).

4.2.4   Combinatorial Devices
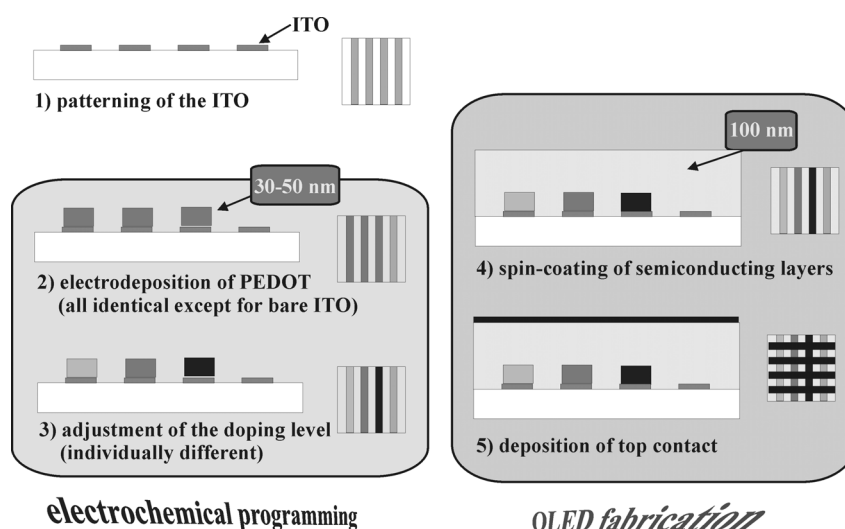
Figure 4-7: Combinatorial polymer devices: Sequence of preparation steps: 1) ITO stripes are etched on glass as a substrate, 2) PEDOT stripes are deposited electrochemically, 3) PEDOT stripes are adjusted to different desired doping levels, 4) the electroluminescent polymer is deposited, 5) the top electrode is evaporated yielding 16 OLED's on a single substrate.

There are several advantages for a combinatorial approach. Identical preparation conditions for all devices on a single substrate allow a direct comparison. This is supported by the fact that measurements for all devices are performed under identical environmental conditions. Short preparation cycles offer the ability of fast screening for an optimum.

Figure 4-7 shows schematically how combinatorial devices were prepared throughout this thesis.

4.2.5   Photometric Properties

IV-curves are measured in order to characterize the OLED's and OSC's. For OLED's the corresponding brightness is monitored simultaneously, which is of outmost importance, since OLED's are designed to work in displays or similar devices. Since the human eye is the receiver of these emitters, the corresponding photometric properties will be briefly introduced in the following.

The observed spectrum of electromagnetic radiations, extends from a few Hz to beyond 10^{24} Hz, covering some 80 octaves. The narrow channel from 430 THz to 750 THz would be entirely negligible, except that more information is communicated to human beings in this channel than from the rest of the spectrum. This radiation has a wavelength ranging from 400 nm to 700 nm and is detectable by the sensory mechanisms of the human eye. Radiation observable by the human eye is commonly called light.

Measurements of the physical properties of light and light sources can be described in the same terms as any other form of electromagnetic energy. Such measurements are commonly called *radiometric* measurements. Measurements of the psychophysical attributes of the electromagnetic radiation we call light are in units, other than radiometric units. Those attributes, which relate to the luminosity (sometimes called visibility) of light and light sources, are called *photometric* quantities. The measurement of these aspects is the subject of photometry.
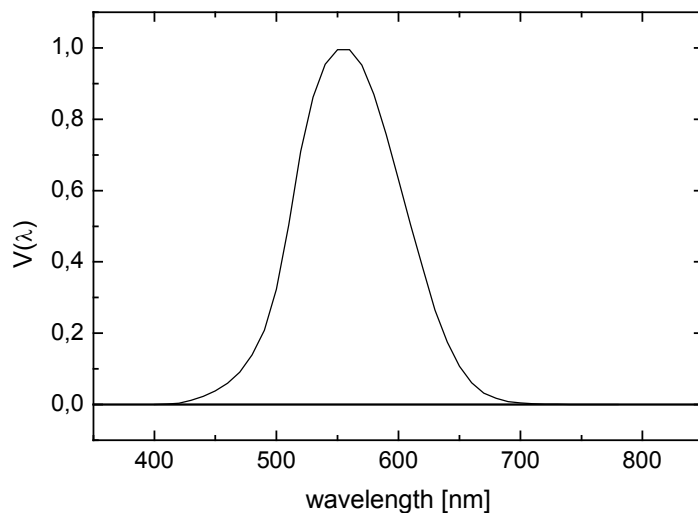
Figure 4-8: C.I.E. standard eye sensitivity function

The photometric quantities are related to the corresponding radiometric quantities by the C.I.E. Standard Luminosity. The luminosity function works as the transfer function of a filter, which approximates the behaviour of the average human eye under good lighting conditions. The eye responds to the rate at which radiant energy falls on the retina, i.e., on the radiant flux density

expressed as W/m^2. The corresponding photometric quantity is lm/m^2. Therefore, the standard luminosity function is a plot of lm/W as a function of wavelength. The function has a maximum value of 680 lm/W at 555 nm and the half power points occur at 510 nm and 610 nm (Figure 4-8).

The lumen is the unit of luminous flux and corresponds to the watt as the unit of radiant flux. Thus the total luminous flux emitted by a light source in all directions is measured in lumen, and can be traced back to the power consumed by the source to obtain an efficiency number. Since it is generally not practical to collect all the flux from a light source and direct it in some desired direction, it is desirable to know how the flux is distributed spatially about the source. If we treat the source as a point (far field measurement), we can divide the space around the source into elements of solid angle (dω), and inquire as to the luminous flux (dF) contained in each element of solid angle (dF/dω). The resulting quantity is lumen/Steradian and is called luminous intensity. The unit of luminous intensity is called the Candela (Cd).

The brightness in this thesis is given by Cd/m^2 as the unit of luminance. The efficiency is given by the "light output per injected charge" in Cd/A.

4.2.6   OLED Lifetime

During operation the polymeric films inside an OLED are under enormous stress. Deußen and Bäßler demonstrated this fact with the following estimation:[76]

Assuming an OLED is driven for 10000 hours at a current density of 100 mA cm^{-2}. During this time more than 2×10^{25} charge carriers per cm^2 pass the device. Having an active area of 1 cm^2, a device thickness of 100 nm and a density of 10^{21} molecules per cm^3 the diode exhibits typically 10^{16} lumophors. Normally a charge carrier needs 10 μs for passing the device. During this time it is transported by roughly 1000 molecules. Therefore, every molecule is converted 2×10^{12} times to a radical anion or cation for about 10 ns per conversion. Thus, a single molecule is charged for about 5.5 hours, in which it should not react with a neighbouring molecule or with impurities in the film. This estimation makes clear how sensitive OLED's are according to impurities like water or oxygen.

In addition an increased temperature stresses the devices, which is due to heat losses caused by low efficiencies.

The examination of the degradation process is difficult, since the effects can just be observed from *outside* the device under test. Beside testing simple physical properties like brightness, current and voltage with time, a non-destructive technique is necessary to observe the heat distribution and visible defects commonly known as "dark spots"[77,78], which occur during degradation. Statistical evaluation of these results can explain device failures and can disclose chances for device improvements.

4.3 <u>Organic Solar Cells (OSC)</u>

According to Figure 4-9 the process of the electricity-to-light conversion observed in OLED's can be reversed yielding OSC's.
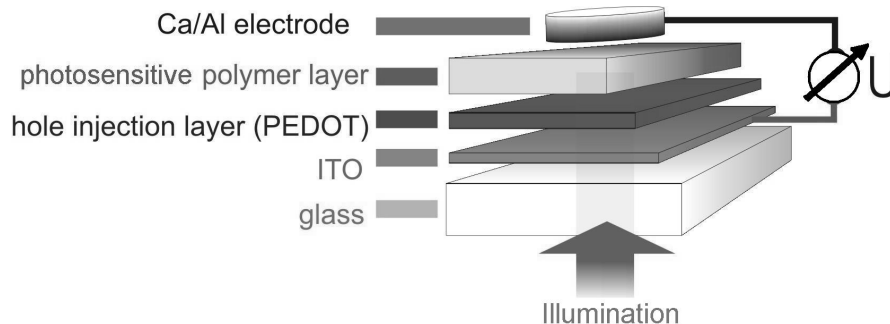
Figure 4-9: Reversion of the OLED principle. Illuminated devices produce an external voltage. This effect can be utilized for power production in OSC's.

The fabrication of solar cells based on polymeric semiconducting materials, rather than conventional inorganic semiconductors offers the possibility of inexpensively producing large area photovoltaic units.[79] Moreover, the inherent ability of these materials to be readily deposited on mechanically flexible substrates means that a variety of geometries are accessible to devices built using these materials. The most efficient devices to-date have been fabricated from semiconducting polymers based on poly(p-phenylene vinylene) (PPV) and its derivatives.[80] The charge generation and conduction mechanisms involved in these devices are complex.

4.3.1   <u>Charge Generation and Exciton Splitting</u>

Charge generation occurs via the photo-induced creation of excitons in the polymer material, which are subsequently dissociated at interfaces between materials of dissimilar ϕ_W.[81] In the original simple devices, this dissociation was limited to the electrode/polymer interface.[66, 81-82]

The tightly bound photo-excited electron hole pairs are unstable, and decay quickly such that they can only diffuse 10 nm on average. Since dissociation of these excitons is only efficient at the interfaces within the device, the instability of excitons renders the majority of the polymer film redundant, acting solely as an optical filter. The low mobility of electrons in p-conducting polymers further reduces the efficiency of these devices as the electrons freed by exciton dissociation at the ITO interface cannot traverse the polymer film and contribute to the current. Consequently, the part of the polymer which lies within an exciton diffusion length of the low work function metal electrode is the only active component in the thin film device.

4.3.2   Potential Improvements for the Device Performance

Areas in which there is room for further improvement of OSC's are perhaps best identified by returning to the steps involved in the generation of the photovoltaic effect:

- exciton creation,
- exciton diffusion,
- electron–hole separation in built-in field,
- carrier transport to electrodes,
- electron transfer at electrodes.

These steps considered, an energy conversion efficiency can be suggested:[83]

$$\eta = \frac{N_{exc}}{N_{ph}} \frac{N_{ct}^{e-h}}{N_{exc}} \frac{N_{free}^{e-h}}{N_{ct}^{e-h}} \frac{eV_{OC}}{h\nu} FF \qquad \text{(to be cancelled down)} \qquad \textbf{(4-12)}$$

$$= \alpha(\omega)\eta_{ex}\eta_{e-h}\xi_{en}FF$$

where

- N_{exc} number of electron hole pairs (excitons)
- N_{ph} number of incident photons
- N^{e-h}_{ct} number of interfacial composite charge transfer (ct) excitons
- N^{e-h}_{free} number of excitons that undergo charge separation
- V_{oc} open circuit voltage
- FF fill factor
- $\alpha(\omega)$ efficiency of photon collection
- η_{ex} quantum efficiency of the excitonic dissociation
- η_{e-h} quantum yield of free electrons in acceptor and holes in donor parts
- ξ_{en} energetic factor (fraction of absorbed photon energy that can be converted to electrical energy)

The most room for improving polymeric photovoltaic cells lies in improving ξ_{en} and the fill factor FF.

The energy factor ξ_{en} can be optimised by adjusting the polymer band gap close to the photon energy of the incident light. If white light is used the band gap should be sufficiently low in order to collect most of the incident wavelengths.

In general there has to be order at the molecular level, if photogeneration and charge transport are to be efficient, and at the meso level, if short distances between the site of irradiation and the charge collection are to be realized.

Attempts to improve the efficiency of the exciton splitting process initially focused on the development of new conducting polymers that contain electron-donating and electron-accepting species.[13,84-85] Creating interfaces between conducting polymer molecules of differing electron affinities enhances the probability of electron transfer between molecules, and the junctions formed at these donor-acceptor interfaces are analogous to semiconductor heterojunctions, leading to exciton separation.[86-91] Although these heterojunctions separate excitons well, the inherent short exciton mean free path length is still a limitation to cell efficiency. However, the development of the bulk-heterojunction concept, which essentially involves the creation of dense interpenetrating networks of electron-accepting and electron-donating polymers has led to dramatic improvements in photovoltaic efficiency.[80]

For organic solar cells made from pure conjugated polymers, energy conversion efficiencies were typically $10^{-3} - 10^{-1}\%$, which is too low to be utilized in commercial applications.[65,66,67] Therefore, the concept of interpenetrating networks of donor and acceptor molecules was used.[13] This concept controls the morphology of phase separation and causes an extremely high interfacial layer within the bulk material. If any point in the composite is within a few nanometers of a D/A interface, such a composite is called "bulk (D/A) heterojunction" material. If the D/A networks in a device are bicontinuous the collection efficiency is highly enhanced. With these materials, the high number of heterojunctions within the polymer blend increases the probability that an exciton will encounter a junction and be separated. Indeed, it has recently been shown that power efficiencies of up to 2.5 % under AM1.5 illumination can be obtained from blends of poly(2-methoxy-5-(3',7'-dimethyl)octyloxy-1,4-phenylenevinylene (MDMO-PPV) and a methanofullerene [6,6]-phenyl C_{61}-butyric acid methyl ester (PCBM).[80]
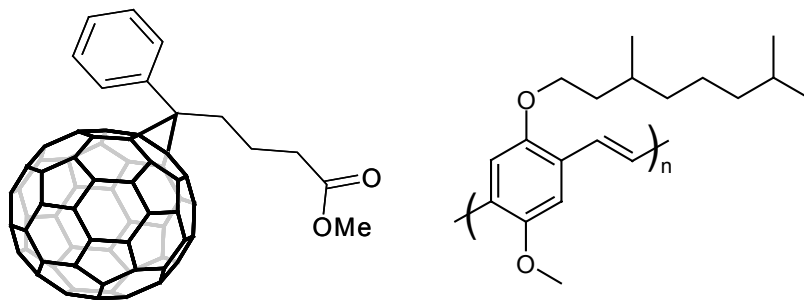
Figure 4-10: Materials for cutting-edge polymer solar cells: PCBM (electron acceptor) and MDMO-PPV (electron donor)

4.3.3   Device Properties

The built-in potential V_{bi}, which is due to the difference in the work functions ϕ_w of the electrodes, has to be applied to an OLED before charge carriers are injected (flat band condition).[92] Indeed, V_{bi} or V_{oc}, respectively, are important properties for OLED and OSC characterization, but there are other important

properties which can be determined in a photovoltaic setup characterizing solar cells.

The characteristics of the photovoltaic effect are shown in Figure 4-11, which shows an IV-curve of a solar cell under illumination. If the device works properly the curve does not pass the origin due to the independent photovoltaic voltage source. The short circuit current (I_{sc}) is the current when the voltage is zero. The open-circuit voltage (V_{oc}) is the voltage when the current is zero. The maximum output of the cell is given by the product $I_{pp}V_{pp}$, where I_{pp} is the current and V_{pp} is the voltage at peak power. The values of I_{pp} and V_{pp} are obtained from the I vs. V curve for the device where the product is maximum at a point along the curve. The fill factor (FF), which gives information about the amount of power output, i.e. the device quality, is defined as:

$$FF = \frac{V_{PP}I_{pp}}{V_{OC}I_{SC}}$$
(4-13)
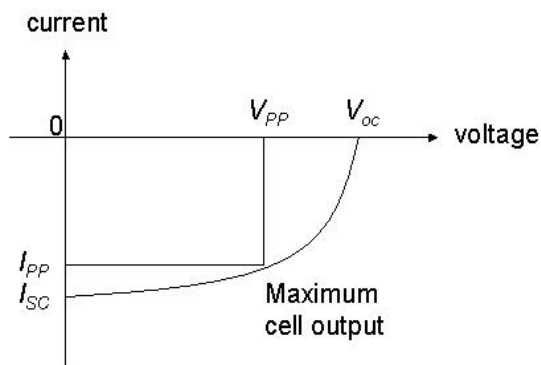
Figure 4-11: Device properties of a photovoltaic cell.

5   Results and Discussion

In the following chapter PEDOT was used as an anodic contact atop the transparent indium tin oxide (ITO). PEDOT is well known as a p-type hole-injection polymer.[93] *Baytron P®* for example is an aqueous suspension of PEDOT, which can be purchased from the Bayer Corporation as a standard anodic polymer. In this suspension PEDOT is stabilized by poly(styrenesulfonate) (PSS⁻) counter ions. Since PSS⁻ acts as a dopand the PEDOT delivered in this suspension is highly doped.

Rather than applying a finished polymer, for this thesis PEDOT was made by electrochemical polymerization of the monomer EDOT (for further details see chapter 7.2.1). The resulting PEDOT films were adjusted thereafter in a similar solution – but without monomer – to various equilibrium potentials E_{eq}. These differently doped layers were first examined by Kelvin probe experiments and then used in OLED's and OSC's in order to get a complete set of data for one of the most important hole injection polymers. In order to extend the results gained for the PEDOT system (p-type) similar experiments were carried out with the n-type C_{60}-polymer C_{60}-Pd.

5.1   <u>Characterization of Doped Polymer Layers</u>

5.1.1   <u>Qualitative Evidence for an Altered Polymer Work Function</u>

The absorption of PEDOT layers with different doping levels were examined in an UV/Vis setup in order to investigate any changes in energy transitions. Figure 5-1 shows the electrochromic response of these films, the arrows indicate the sequence of an increased doping level.

In the dedoped, neutral form the spectrum of PEDOT has a broad absorption band around 560 nm stemming from π-π*-transitions. This neutral form is deep blue. The absorption peak is broad due to the absorption of chains and conjugated segments of different length.[95] The respective band starts at about 760 nm, which corresponds to a band gap of 1.6 eV.[96-97] When the film is oxidized, it becomes discernible that the peak at about 560 nm decreases, which is due to an altered HOMO-LUMO transition, whereas the increased absorption at 970 nm stems from doping-induced mid-gap states.[98] The charged film exhibits a transparent grey-bluish colour. The incorporated counterions do not influence the spectrum since they do not absorb in the visible range.

Please note that the film at E_{eq} = –410 V is *not* a completely discharged (neutral) film. Considering the Nernst equation it is nearly impossible to get to fully neutral films. Therefore, the film at E_{eq} = –410 V has a remaining peak for wavelengths higher than 750 nm, i.e. a certain amount of mid-gap states remain.
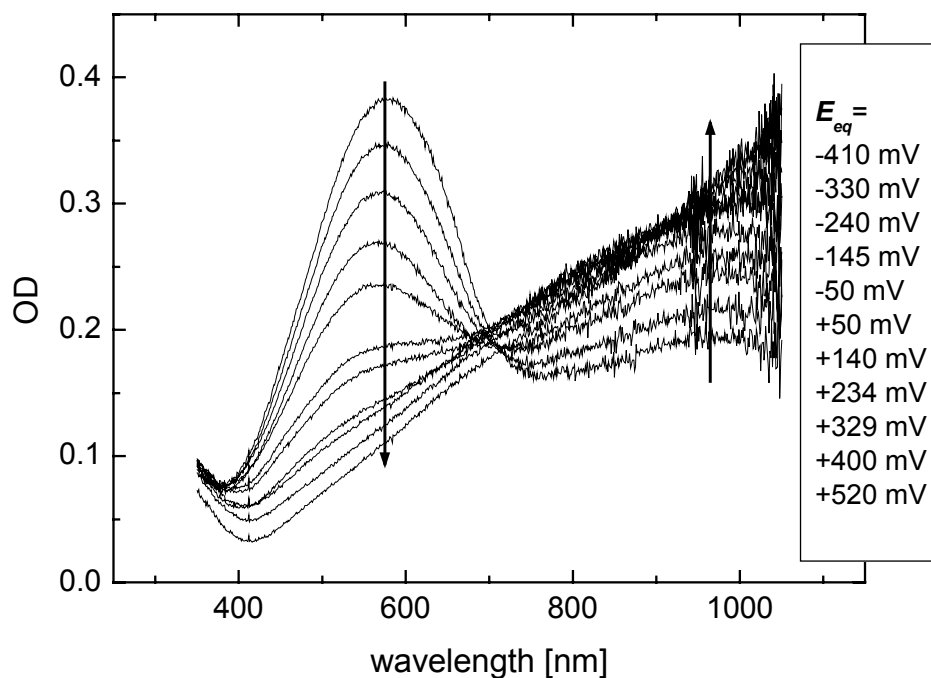
Figure 5-1: Electrochromic response of a PEDOT film doped at several doping levels. Arrows mark the sequence of increasing doping levels.
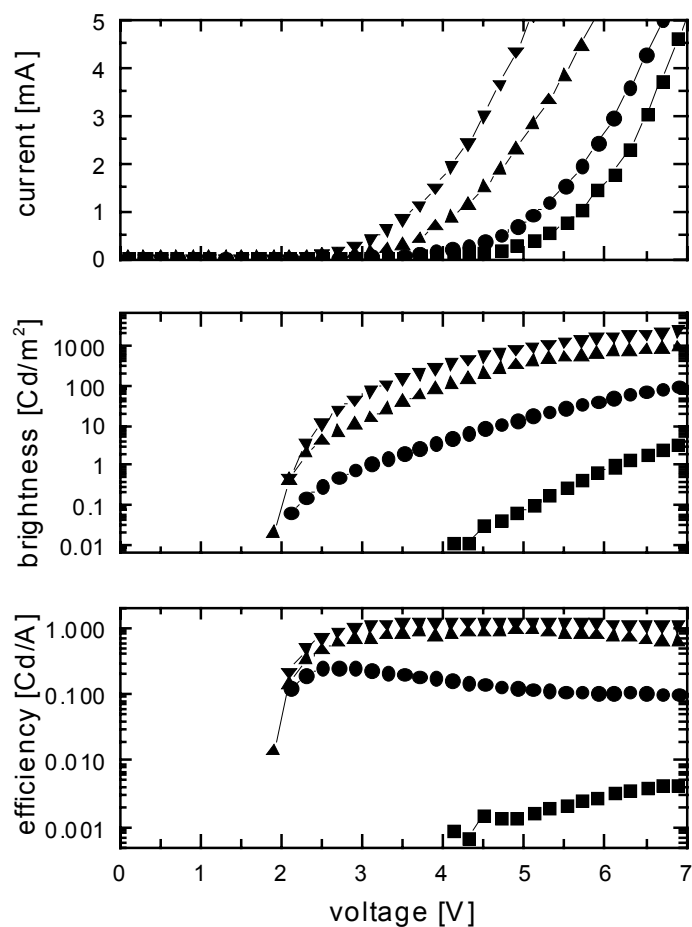
Figure 5-2: Influence of different PEDOT doping levels on the OLED (ITO / PEDOT(E_{eq}) / MDMO-PPV / Ca) performance: E_{eq} = -326 mV (squares), 36 mV (circles) 256 mV (up triangle) 551 mV (down triangle).

Devices of the structure **ITO / PEDOT(E_{eq}) / MDMO-PPV / Ca** were fabricated. In Figure 5-2 the results of a current-voltage-brightness investigation are summarized. The onset field for hole injection decreases systematically with increasing oxidation potential E_{eq} of the PEDOT layer. Beside the displayed curves intermediate curves can be obtained by properly adjusting E_{eq}. This fact pronounces that PEDOT is adjustable in a continuous way, which is not limited to certain steps. As the electroluminescent layer (MDMO-PPV) and the cathodic contact (Ca) are identical in all cases, these observations must be correlated with a decreased barrier for holes as a result of an increased work function of the PEDOT. These results provide an indirect proof for the concept of influencing the work function by adjusting the redox state of a conjugated polymer. It becomes obvious that for an increasing E_{eq} the onset voltage decreases and that the brightness and the efficiency increase.

In summary, the results of the current-voltage-brightness measurements suggest that the work function of PEDOT could have changed, but a quantitative evaluation had to be achieved by other techniques.

5.1.2   Kelvin Probe Measurements

Kelvin Probe measurements were carried out in order to obtain *quantitative* evaluation for a changed work function of the preadjusted PEDOT films. Using a Kelvin Probe setup described in Chapter 3.3 the contact potential difference (CPD) between a reference electrode and the material of interest (PEDOT) could be determined. This measurement monitors changes of the PEDOT work function as dependant on the changed electrochemical potential of the film. The experimental conditions were kept as close as possible to the preparation process of solution-based organic devices. Therefore, an inert gas atmosphere was chosen for the surrounding medium rather than air or vacuum.

A linear correlation between the *CPD* and the E_{eq} of the respective PEDOT layer (Figure 5-8a) was determined. The resulting slope of a linear regression was 0.8. Fortunately, the data point measured for the spincoated Baytron® (Bayer PEDOT) is part of this line as well (open square). This fact pronounces consistency for different preparation and doping methods of PEDOT, i.e. a certain E_{eq} is always correlated to a *single CPD* – independently from the preparation method.

A direct translation between E_{eq} and *CPD* (slope 1) is assumed in general, although there are reports in the literature on investigations in dilute solution reporting deviations (slope of 0.8 – 0.9).[100-102] Possible deviations from unity can be attributed to changes in the solvation energy. Nevertheless, this explanation cannot be applied for the measurements presented here, since the solvent was removed before Kelvin probe measurements were carried out.

The deviation from unity in the presented case can be attributed to the fact that counter ions enter the film during the oxidation process. This penetration is necessary in order to archive electroneutrality in the film, leading to changes of the polarization energy of the solid medium. By contrast, for pure ion exchange processes in the absence of redox reactions (Donnan potential) Kutner et al. reported a slope close to unity.[103]

5.1.3 Extension to Other Polymers

A similar polymer poly(4,4'-dimethoxy-bithiophene), called PDBT, produces similar results compared to PEDOT.[99] Although the chemical structures of PDBT and PEDOT are related, this finding is promising for gaining universal validity.

In order to extend the concept, completely different polymers were examined. One approach was a n-type C_{60}-Pd polymer (Figure 5-3) synthesized electrochemically. This polymer can form polymer chains or networks dependent on the ratio of the educts.[103] C_{60} derivatives are known for the ability of multiple reductions.[104] Therefore, this approach promised to extend the adjustable range down to electrochemical potentials, which could provide cathodic contacts for polymeric devices. This possibility would allow to built a completely polymeric device without any metal layers. In addition both the anodic (PEDOT) and the cathodic (n-type polymer) could be adjusted separately.
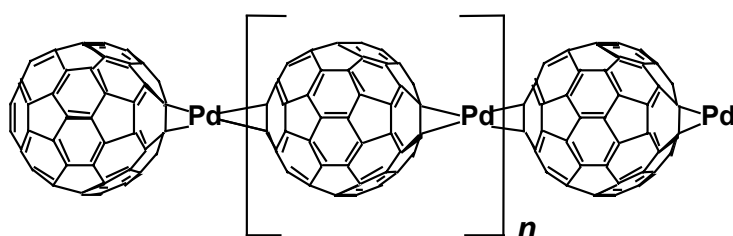
Figure 5-3: C_{60}-Pd polymer synthesized electrochemically.

The C_{60}/Pd film was prepared under cyclic voltammetry conditions. The potential range was cycled from zero to -1.5 V back and forth (Figure 5-4). In each cycle the thickness of the polymer layer was increased. In addition the total current per cycle increased as well. This finding can be explained in terms of a deposition current, which remains nearly constant in every cycle, and an additional reloading current, which is rising with an increasing film thickness.
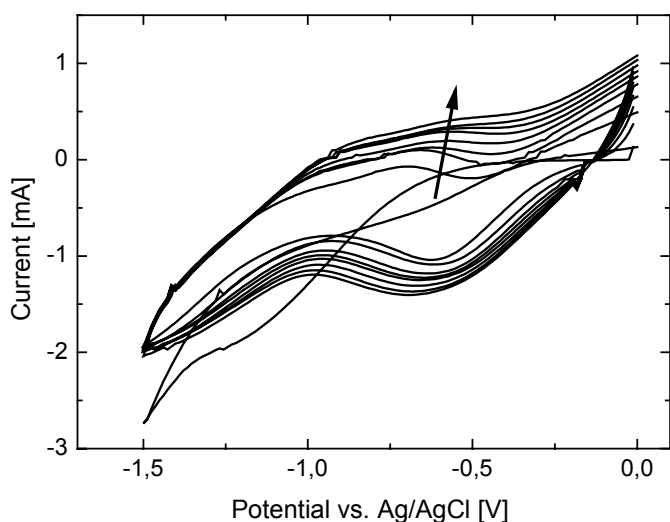
Figure 5-4: Cyclic voltammogram of C_{60} -Pd deposition on ITO at a scan speed of 0.1 V/s. The current increases from cycle to cycle. Here, just every fifth cycle is plotted.

Figure 5-5 shows a voltammogram of the adjustable range, which is promising due to a usable width of at least 2 V (further possible reduction peaks are not visible in this graph).
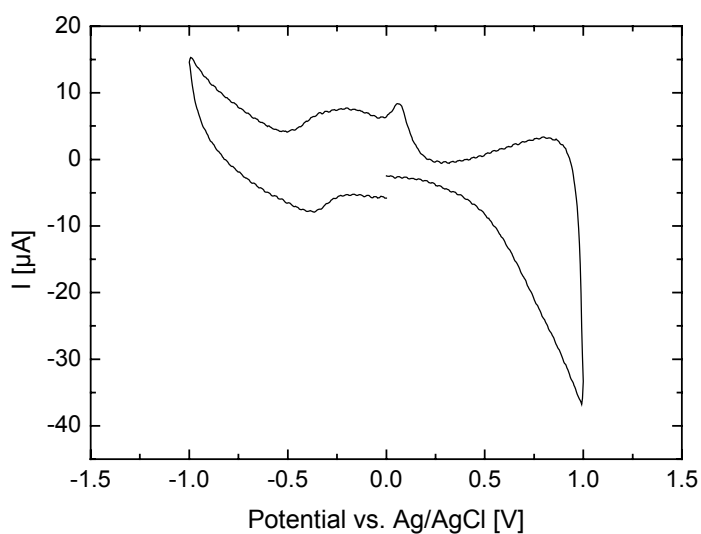
Figure 5-5: Cyclic voltammogram of the deposited C60-Pd-stripes in (TBA)PF_6 in acetonitrile/toluene.

As described in Ref. [103] the reduced polymer film becomes partially electrochemically inactive at a sufficiently negative potential range. At very negative potentials, the film is removed from the electrode. Other problems occurred due to the solvents used, which were not stable in the desired negative potential range. Instead, this film can be oxidized at positive potentials. For charge compensation, the tetra(n-butyl)ammonium counter cations enter the film during its electroreduction and are expelled from the film during electrooxidation.

Figure 5-6 shows Kelvin Probe measurements at differently doped C_{60}-Pd films (solid squares). In comparison with the PEDOT results (open squares) there is a perfect agreement with the already obtained correlation (slope 0.8). Therefore, these experiments give evidence that the electrochemical potentials of totally different polymers translate directly to the respective work function.
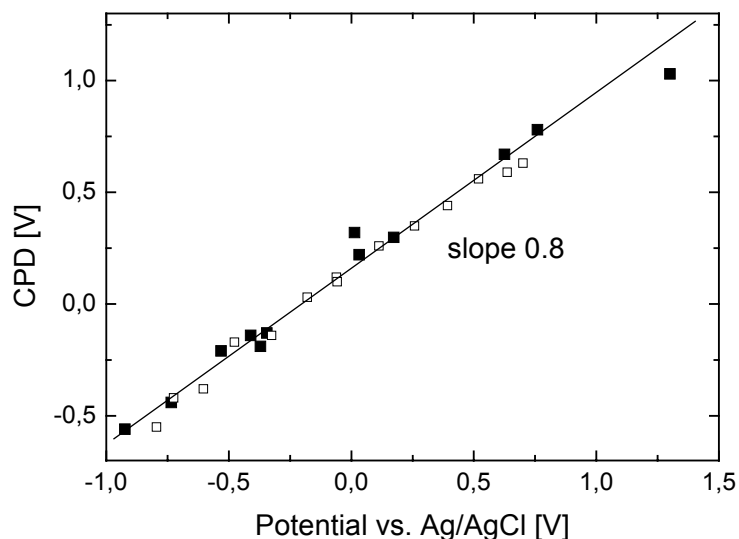
Figure 5-6: Kelvin Probe measurements on electrochemically adjusted C_{60} -Pd films (solid squares). A slope of 0.8 akin to the PEDOT measurements (open squares) was obtained.

Considering technological demands, metals like Pd are not the compounds which are preferred, especially if there is an interest in cheap products with a short life cycle. Another disadvantage is that Pd nanoclusters are incorporated into the film during polymerisation.[104] Pd has a high work function and these clusters can influence the device performance. The smaller work functions, which are desired for an operation as a cathode, might not be reached due to the Pd nanoclusters.

5.1.4   Photovoltaic Investigations

Kelvin probe measurements, which were presented in the last two chapters, determine the *CPD* of a *semi-freestanding* film. Since the results gained for PEDOT were promising there was a desire to use the changed work function as a adjusted anodic contact *inside* a polymeric device. However, the PEDOT doping is followed by a spincoating process. For OLED's an electroluminescent polymer and for OSC's a photosensitive polymer is spincasted on top the PEDOT layer. This solution based preparation step may not necessarily preserve the pre-adjusted PEDOT doping level.

In order to verify that changes of the PEDOT work function can also be found in a finished device photovoltaic measurements were performed. Several authors have detected work function changes caused by different metal cathodes providing different work functions in real devices by

electroabsorption measurements.[28,106] The fact that the built-in potential V_{bi} can also be determined in a photovoltaic (PV) configuration[107] is utilized in the following measurements. Charges from excitons which split close to the interfaces of a device start to travel towards the electrodes due to the internal field given by the difference in work function of the two electrodes (PEDOT and metal). Charges, which reach the electrodes, then contribute to the photocurrent. If the built-in field V_{bi} is compensated by applying a compensation voltage V_0,[108] the net photocurrent vanishes. This corresponds to the flat band situation of the device, therefore

$$V_0 = V_{bi} = \frac{\varphi_{W,anode} - \varphi_{W,cathode}}{e}.$$ (5-1)

Equation (5-1) is just valid for high injection barriers, since injection limited currents are usually not influenced by space charge effects. If the barriers decrease, the electroactive material between the electrodes is not able to transport the injected charges, which results in a partly charged layer at the contact. The resulting band bending of these regions reduce the internal electric field in the device by about 0.2 eV for each (ohmic) contact. Thus, for two ohmic contacts the maximum built-in voltage is typically 0.3-0.4 V lower than the band gap.

For the photovoltaic experiments devices of the general structure **ITO / PEDOT(E_{eq}) / EL polymer / cathode** were fabricated. Figure 5-7 shows the absorption spectra of the orange emitting PPV-derivative MDMO-PPV used in the OLED's and of the blend MDMO-PPV : PCBM used for the bulk-heterojunction OSC's in Chapter 5.3. A vertical line at 532 nm indicates the wavelength of the incident laser light for the photovoltaic measurements. The photon energy does not coincide exactly with the absorption maximum, but, nevertheless, it is sufficient to excite the polymer with its energy being above the band gap. Adding PCBM to the MDMO-PPV results in a broader absorption over the total range of wavelengths (Figure 5-7b) compared to the single peak of pristine MDMO-PPV. Beside a slightly increased absorbance for the red end of the spectra there are additional peaks for the blue end. An overall increase of absorption is in accordance with the brownish appearance of these blend layers. This fact pronounces the quenching effect of PCBM. Any exciton which is produced close to a PCBM molecule will be dissociated very quickly passing its electron onto the buckyball.

Figure 5-8b) shows the results of the PV investigations. The MDMO-PPV devices were illuminated with a 532 nm laser, and the open circuit voltages were determined. Two sets of devices with different cathodic metals were used. One set exhibited an evaporated aluminium (Al) cathode, the other set exhibited an evaporated calcium (Ca) cathode. In both cases, a linear correlation between E_{eq} and V_{oc} was obtained. The slope of the linear regressions was 0.8 akin the Kelvin Probe results. Therefore, a preserved work function change of the PEDOT layer could be demonstrated for the finished device.
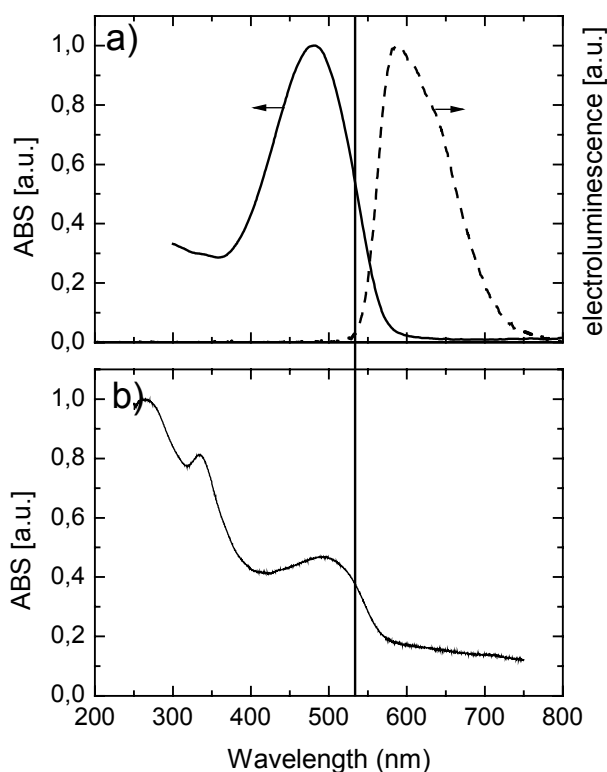
Figure 5-7: Absorption measurements of the used electro-active polymers; the vertical line indicates the wavelength of the incident laser light of 532 nm.
a) absorption and electroluminescence spectrum of MDMO-PPV
b) absorption spectrum of the blend MDMO-PPV : PCBM

The fact that Ca-devices exhibit a higher V_{oc} can be explained in terms of a lower work function of Ca compared to Al,[109] which results in a higher built-in field and, therefore, a higher overall V_{oc}. Again, this finding demonstrates that *in general* work function changes of *both* electrodes result in a changed device performance. Deviation can be observed for bulk-heterojunction devices, for which the cathodic energy level is pinned (compare Figure 5-9).

Kelvin probe and the photovoltaic measurements yield an identical slope (0.8) in their dependence on E_{eq} showing that the changes measured on the surface of a semi-free-standing film translate directly to the internal energy conditions in the finished device.
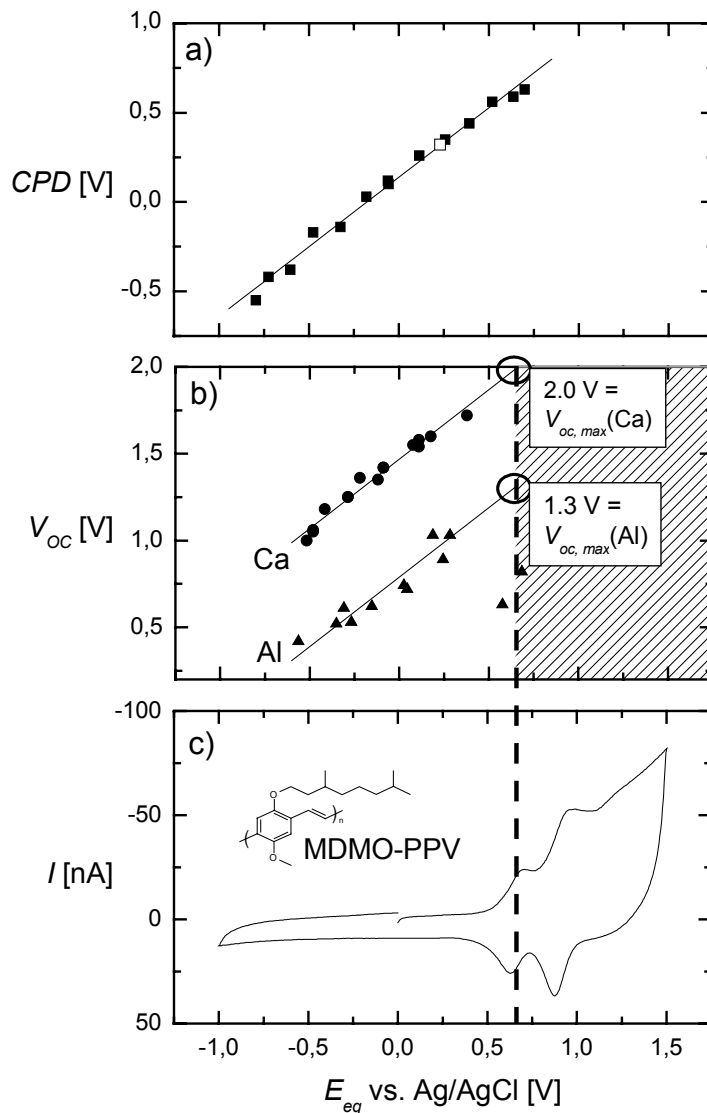
Figure 5-8: Dependence of the relative work function ϕ_w of PEDOT on the equilibrium potential E_{eq}:

a) Kelvin probe measurements reveal the contact potential difference (*CPD*) between the freestanding film and a gold grid as a reference (solid squares). In comparison the open square represents the commercial PEDOT (Baytron®). The solid line displays a linear regression to the data points;

b) Photovoltaic characterization of devices of the general structure PEDOT(E_{eq})/MDMO-PPV/cathode yields the open-circuit voltage V_{oc} for devices with a Ca- (circles) and Al-cathode (triangles), respectively. The lines are linear fits to the data. The shaded area is "forbidden" because of $E_{eq} > E_{ox,MDMO-PPV}$ (see text for details). The circles mark the maximum voltage $V_{OC,max}$;

c) Electrochemical characterization of the emitter polymer MDMO-PPV: Cyclic voltammogram in CH_2Cl_2/0.1M $TBAPF_6$. The dashed line indicates the first oxidation potential $E_{ox,MDMO-PPV}$. Inset: chemical structure of MDMO-PPV.

It is noteworthy that irreproducible results (data points close to the hatched area) were obtained in the PV measurements whenever E_{eq} of the PEDOT anode approached or even exceeded a certain E_{eq}. This finding is in contradiction with the Kelvin probe results, where these irregularities for

higher potentials were not observed. The reason for this deviation can arise from the difference in the architecture of the samples used for these measurements. The first technique examines the semi-freestanding film, whereas the second technique examines a device in which PEDOT is covered by MDMO-PPV. In order to investigate a possible influence a cyclic voltammogram of MDMO-PPV was measured and, indeed, the origin of the deviations could be discovered:

In Figure 5-8 the characterizations of differently doped (x-axes) PEDOT films are summarized. Beneath the Kelvin Probe results the V_{oc}'s are plotted, which are gained from the PV measurements of devices with different cathode metals. The cyclic voltammogram of the electroluminescent polymer MDMO-PPV in the third graph explains the deviations in V_{oc} for higher E_{eq}, which is attributed to doping (oxidation) of the MDMO-PPV by the highly oxidized PEDOT layer. Because of these redox reactions, which seemingly lead to irregularities in the device performance and which are also expected to lead to reduced electroluminescence, the range $E_{eq} > E_{ox}$ is "forbidden" (shaded area in Figure 5-8b). Under conditions excluding redox reactions of the PEDOT, e.g. for the Kelvin probe experiments, (Figure 5-8a) the mentioned irregularities do not occur.

The open circuit voltages $V_{oc,max}$ for which the extrapolated curves in Figure 5-8b) enter the forbidden area will be utilized later on. They define the E_{eq} for which PEDOT has the same energy level as the HOMO of MDMO-PPV (first oxidation peek in the cyclic voltammogram). Therefore, the barrier for holes can be estimated to be zero for this extrapolated value. The reason why the experimental values drop down slightly before they reach the forbidden range is given by the fact that there is a certain probability for oxidation before the oxidation potential is reached. Although oxidation becomes more likely beyond the peak, it occurs already before the main oxidation potential is reached.

Pinning Effect
Photovoltaic investigations have to be interpreted carefully if energy level pinning takes place. This effect has been observed for bulk-heterojunction OSC's, in which the C_{60}-polymer PCBM is utilized as an acceptor molecule spincoated in a blend with MDMO-PPV. PCBM forms an interpenetrating network, which transports electrons, whereas MDMO-PPV transports holes.

The pinning effect, which occurs for this system, is demonstrated in Figure 5-9. The upper three curves are obtained from devices produced without PCBM (just MDMO-PPV), whereas the last curve is produced with PCBM blended to the MDMO-PPV. The known slope of 0.8 can be observed for every curve, and the distance between the V_{oc}-curves corresponds to the sequence in work function of the respective metals (except for the PCBM-device). These experiments verified the well known fact[79] that the PCBM device has a lower V_{oc} and does not change when the metal of the cathode is changed. This behaviour is called the pinning effect. PCBM "pins" the energy level of the adjoining metal to a certain position – no matter which work

function the metal has. Measurements for determination of the exact energy level of this pinning are presented later. This effect will also be utilized for the PEDOT energy scale calibration in chapter 5.4.
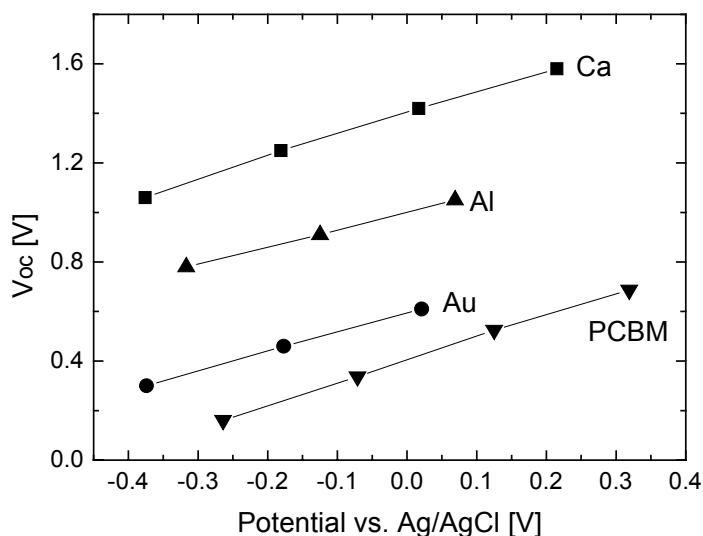
Figure 5-9: Pinning effect: Open circuit voltages (V_{oc}) of PEDOT(E_{eq})/MDMO-PPV/metal-devices for different cathode metals (Ca, Al, Au), for the lowest curve PCBM is blended into the MDMO-PPV-layer (the cathodic metal does not influence the V_{oc} anymore, for the points displayed here Al was evaporated).

5.1.5   Stability of adjusted doping level

It is still not fully understood if anions or cations are responsible for balancing the charge in the PEDOT film during doping/dedoping processes. During the doping process of PEDOT anions (e.g. PSS⁻) could enter the film, but the same effect of charge compensation can also be achieved by cations (e.g. Na⁺), which leave the film. The latter effect is more likely since the PSS⁻ used for these experiments has a molecular weight of 70.000 g/mol, which can hinder PSS⁻ movement sterically. Once built into the film during polymerization it will most likely stay there. A device built onto this layer will benefit from this fact since PSS⁻ cannot penetrate into the adjoining layers shorting the lifetime of the device. A method to check which ion travels upon oxidation or reduction is the microbalance measurement.[110] This technique uses a vibrating working electrode in the electrochemical cell. During the doping process the frequency of this electrode is monitored. If ions enter the film the weight increases and, therefore, the natural frequency decreases and vice versa. Thus, the direction of ion movement can be determined exactly. If for example the weight during the doping process increases it is obvious that PSS⁻ enters the film. If the weight decreases it is obvious that Na⁺ leaves the film. In addition the changes in mass per charge can be calculated quantitatively from the cyclic voltammogram and the respective frequency graph. Unfortunately, the motion of ions could not be measured so far.

In an actual device the stability of the oxidation level of the PEDOT films is very important. If they can be adjusted to an optimum for a certain device it is obvious that the doping level should not change with time in order to preserve this optimal behaviour. Therefore, the temporal stability of the adjusted doping level was checked by observing an uncovered PEDOT-film under inert gas conditions inside a glovebox. Figure 5-10a) shows the temporal development of the absorption spectrum.
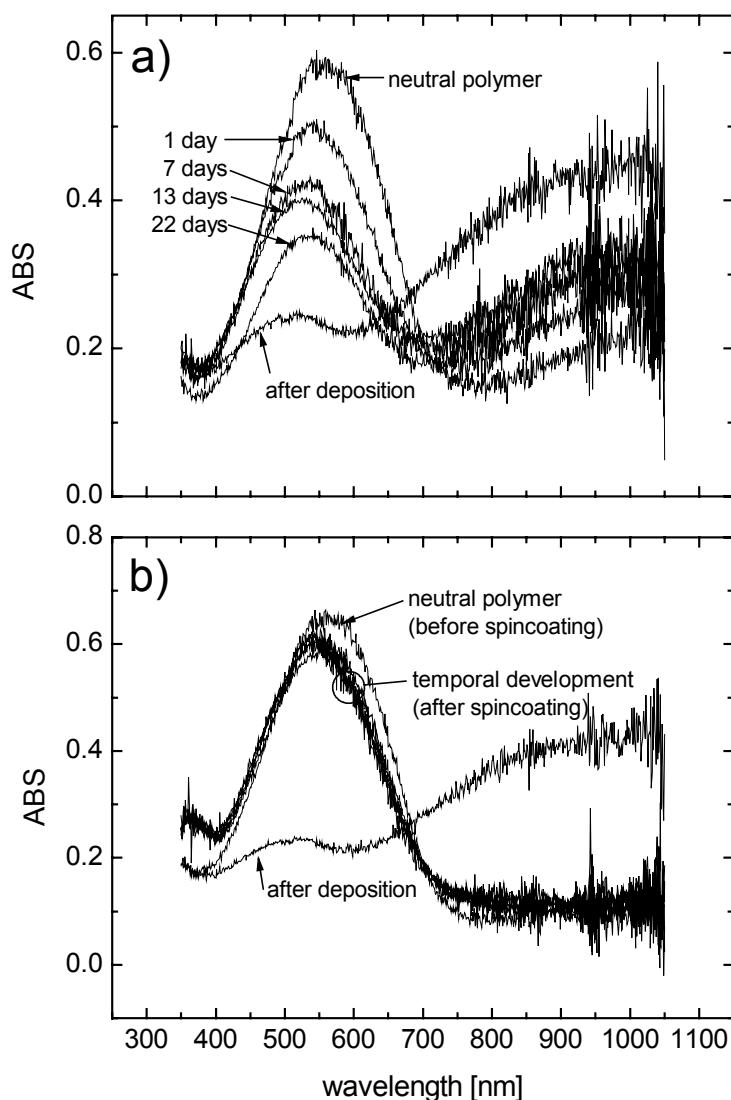
Figure 5-10: Temporal development of a dedoped PEDOT-film in a glovebox: a) bare film; b) film covered with MTDATA (see Fig. Figure 5-11) measured immediately after the spin coating process. The baseline recorded from ITO covered glass slides has been subtracted for both substrates. The baseline has been recorded for glass/ITO slides. Absorption deviations are caused by slightly different PEDOT layer thicknesses and the additional MTDATA layer for the measurements in b).

The peak at 560 nm (HOMO-LUMO transition of neutral polymer) has the lowest value in the measurement immediately after the film deposition. Thereafter the film was reduced to its neutral form and, consequently, the curve with the highest peak was measured. This film was kept inside the

glovebox. Repeating this measurement after one day, one week, two weeks and three weeks show a successive decay of the peak indicating a slow but continuous oxidation. This fact can be attributed to the minimum residual amount of oxygen (< 3 ppm) inside the box. Inside a polymer device this oxidation should be hindered due to the covering layers and the general encapsulation of the device.

In order to check the effect of a covering layer the same experiment was carried out simultaneously with a thin spin coated layer of 4,4',4''-tris(3-methylphenylphenyl-amino)triphenylamine (MTDATA, Figure 5-11) which is known as a common molecular hole conductor.[111] The advantage of MTDATA compared to MDMO-PPV is the transparency in the observed wavelength range, whereas the interfacial conditions can be assumed to be identical. In Figure 5-10b) just a slight decrease of the band gap peak can be observed after the MTDATA layer has been deposited. Thereafter the absorption does not change for weeks. Thus covering the PEDOT layer by another polymer layer is sufficient to avoid oxidation caused by the environment. Diffusion of oxygen through the covering layer cannot be excluded in general but this process is as slow that a continuous preparation of the device followed by a final encapsulation avoids this possibility.
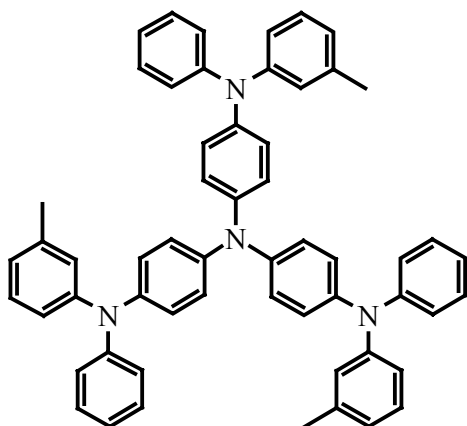
Figure 5-11: Molecular structure of the transparent hole conducting 4,4',4''-tris(3-methylphenylphenyl-amino)triphenylamine (**MTDATA**)

5.2   Utilization of PEDOT Oxidation Level for OLED Optimisation

5.2.1   Injection Barrier Heights for Electrons and Holes

In the following the barrier situation inside the tested devices will be estimated based on the results gained from the Kelvin probe, PV and CV investigations. From the results presented in Chapter 5.1 the first conclusion is that the barrier for injected *holes* at the PEDOT electrode decreases with a slope of 0.8 eV/V, if plotted against E_{eq}. The second conclusion is that this hole injection barrier is zero for $E_{eq} = E_{ox,MDMO-PPV}$ = 0.65 V, since for this situation the work function of the PEDOT layer equals the HOMO level of the MDMO-PPV in which the holes are injected (compare "PEDOT" curve in Figure 5-12). Considering these two conditions the barrier height for holes can be written as:

$$\phi_{B,h}\left(E_{eq}\right) = -0.8e\left(E_{eq} - E_{ox}\right) = -0.8eE_{eq} + 0.52\,eV \qquad \textbf{(5-2)}$$

On the other hand the injection barrier for *electrons* is the difference in energy between the work function of the evaporated metal and the LUMO level of MDMO-PPV in which the electrons are injected.
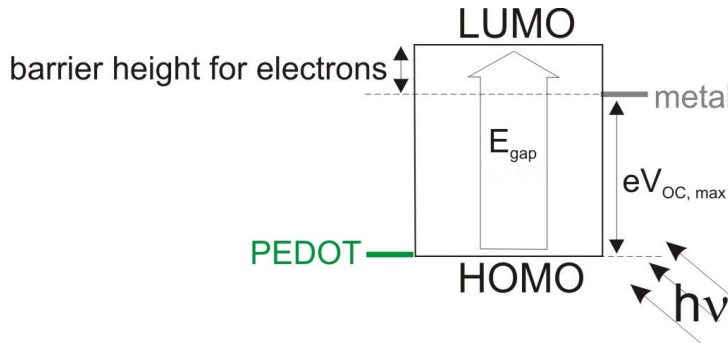
Figure 5-12: Energy sketch for the determination of the injection barrier height for electrons ($\phi_{B,e}$). This sketch displays the situation, where PEDOT is oxidized exactly to the oxidation potential of MDMO-PPV. For this situation PEDOT's work function levels exactly the HOMO level of the adjoining MDMO-PPV. Therefore, the injection barrier for holes is zero in this case ($\phi_{B,h}$ = 0).

Figure 5-12 displays the special situation, where the equilibrium potential of PEDOT equals the oxidation potential of MDMO-PPV. Exactly for this situation the extrapolated V_{oc}-regression enters the hatched area in Figure 5-8b), which is indicated by two circles marking the Ca and Al type devices, respectively.

The band gap E_{gap} corresponds to the distance between the HOMO and LUMO levels, which can obviously be written as a sum of the barriers and the open circuit voltage V_{oc}:

$$E_{gap} = eV_{oc} + \phi_{B,h} + \phi_{B,e} \qquad \textbf{(5-3)}$$

Considering the absorption edge of MDMO-PPV, a HOMO-LUMO gap of about $E_{gap} \approx 2.1$ eV can be estimated (Figure 5-13).
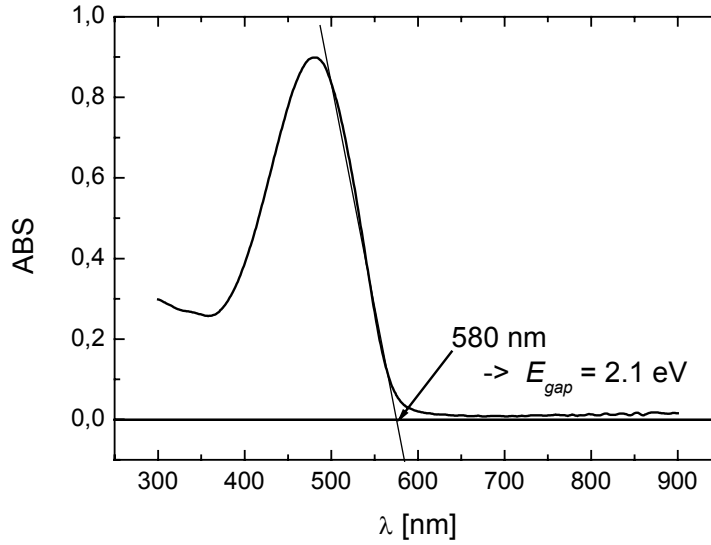
Figure 5-13: Absorption spectrum of MDMO-PPV: HOMO-LUMO gap of about $E_{gap} \approx 2.1$ eV can be estimated from the absorption edge at 580 nm

In Figure 5-8b) for the Ca-devices, $V_{oc,max}$ = 2.0 V is extrapolated. Thus, according to Figure 5-12 and Equation (5-3) the barrier for electron injection, $\phi_{B,e}$, can be estimated:

$$\phi_{B,e}(\text{Ca}) = E_{gap} - eV_{oc,\text{max}}(\text{Ca}) = 2.1\,\text{eV} - 2\,\text{eV} = 0.1\,\text{eV}\,, \tag{5-4}$$

This barrier is sufficiently low that the electron current is expected to be space-charge-limited (SCLC).[112]

For the Al-devices, $V_{oc,max}$ = 1.32 V can be extrapolated in Figure 5-8b). The barrier for electrons can be calculated according to Equation (5-3) resulting in $\phi_{B,e} \approx 0.78$ eV. This high barrier is responsible for an injection limited electron current (ILC) in Al-devices.

The dependence of the barriers on E_{eq} is summarized in Figure 5-14. The electron barrier is fixed for one sort of cathode (Al or Ca). With decreasing E_{eq} the hole barrier rises with a slope of 0.8 from an initial ohmic contact at E_{ox}. Two intersections can be determined in this graph, which display identical barrier heights for electrons and holes in the respective devices. Close to the respective intersection both barriers are IL for the Al-devices and both barriers are SCL for the Ca device. Thus, these two device types allow to study efficiency optima for different current conditions.

Theoretically an optimum can be expected for devices containing PEDOT layers, which are oxidized to an E_{eq} close to the intersections of the

corresponding barrier curves. In this case electrons and holes are balanced and an optimized recombination process should lead to an enhanced efficiency.
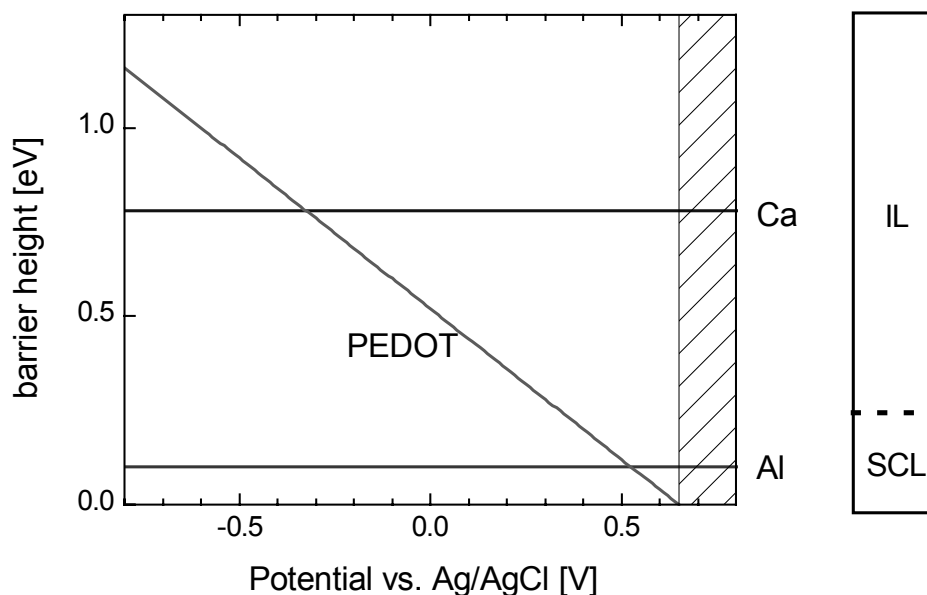
Figure 5-14: The dependence of the charge injection barriers on E_{eq} is summarized. The right box indicates the current conditions for different barrier heights, which are for space charge limited (SCL) for low barriers up to 0.3 eV and injection limited (IL) for higher barriers.

5.2.2   Optimum in Efficiency

After the work function has been determined by both Kelvin Probe and photovoltaic measurements, the same devices were driven as OLED's. The external luminescence efficiency for a constant current of 2 mA is plotted against E_{eq} in Figure 5-15b and Figure 5-17b for the two sets of devices with Al- and Ca-cathodes, respectively. In order to avoid potential heating effects constant-current conditions (I = 2 mA) were chosen for all devices. The voltages which were needed to reach the fixed current level of 2 mA decreased with increasing E_{eq} (open circles / dot dashed lines in Figure 5-15b and Figure 5-17b). This fact can be explained in terms of an increasing hole current caused by the decreasing anodic injection barrier.

In Figure 5-15 the results for the Al-devices are summarized. Their efficiency (b) at a current of 2mA (solid squares; left axis) exhibits an optimum and is in good agreement with the intersection of the barrier height estimation (a). The operating voltages of the devices (open circles; right axis) are also plotted. For comparison purposes the dashed line indicates the built-in in field corrected voltages, which considers that the built-in field has to be compensated before a net voltage can inject charge carriers (Figure 5-16).
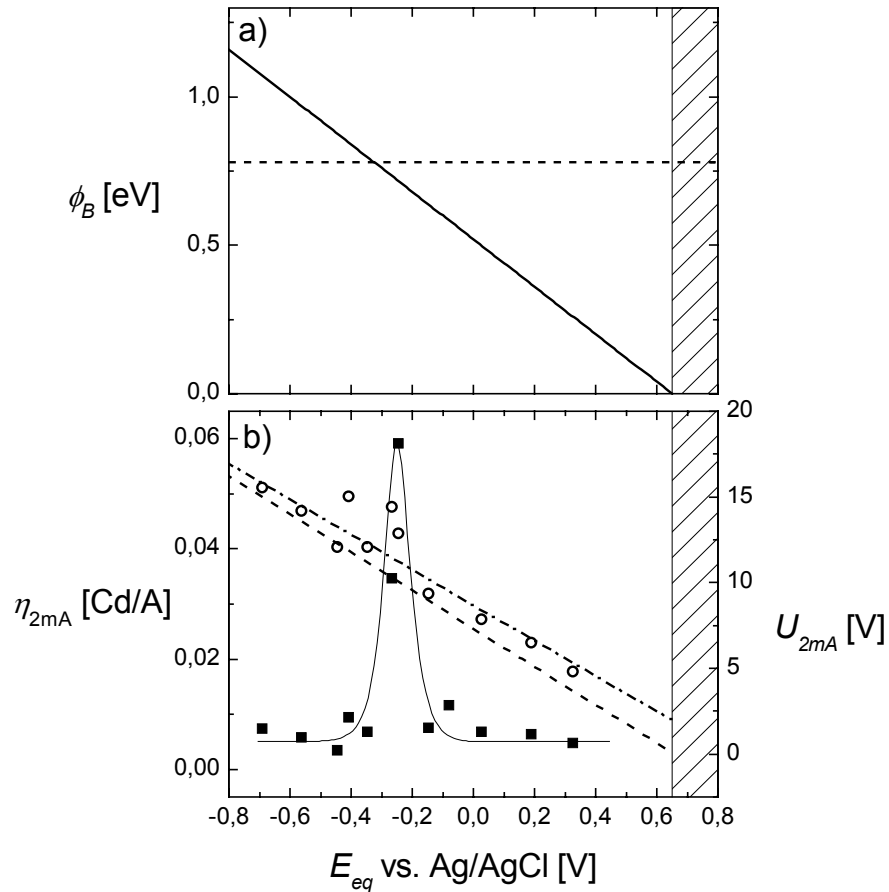
Figure 5-15: Characterization of **Al**-OLED devices of the general structure PEDOT(E_{eq})/MDMO-PPV/**Al** in dependence of the equilibrium potential E_{eq} of the PEDOT layer.
a) Estimated hole barrier heights (solid line) and estimated barrier heights for electrons in the **Al**-device (dashed line);

b) Efficiency of the **Al**-devices at a current of 2 mA (solid squares; left axis); Operating voltage of the devices (open circles; right axis). The dash dotted line represents a linear regression to the data. The dashed line indicates the built-in field corrected voltage.
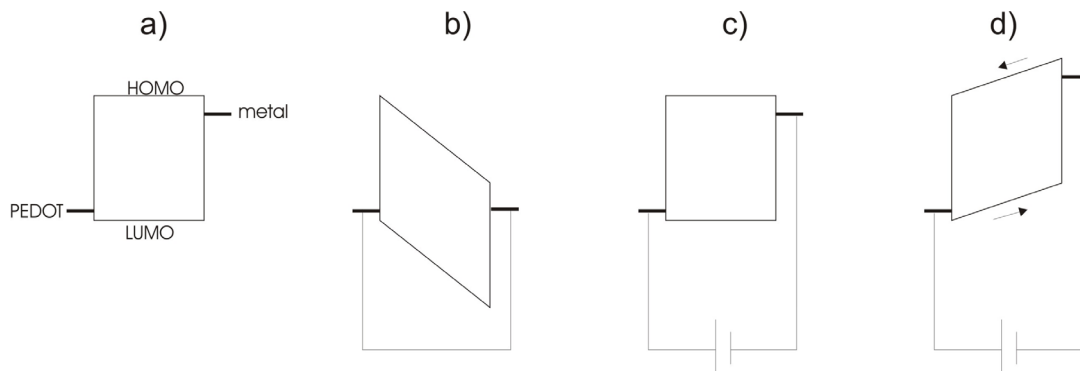
Figure 5-16: The built-in field given by the difference in work function of PEDOT and the metal (a) causes a tilt of the energy band (b) if the electrodes are connected electrically. The built-in voltage has to be applied (c) at least before the first charge injection can take place (d).

The respective built-in field changes with a changed PEDOT doping level according to Figure 5-8b). For E_{ox} = 0.65 V the built-in field is $V_{oc,max}$ = 1.32 V according to the extrapolated value from Figure 5-8. For lower potentials the built-in field decreases with the known slope of 0.8.

In Figure 5-17 the efficiency results for the Ca-devices are displayed. Their efficiency (b) at a current of 2mA (solid squares; left axis) exhibits an optimum which is also in good agreement with the intersection of the barrier height estimation in a). The measured efficiency shows a broader peak than the efficiency peak for the Al-device. This fact is explained by different current conditions. The Al-device exhibits ILC conditions close to the measured optimum, i.e. barriers for both sorts of charge carriers are high and even a small barrier change results in a distinct current change. The Ca-device exhibits SCLC conditions close to its peak in efficiency since the barriers for both sorts of charge carriers are low. For ohmic contacts or low injection barriers an accumulation region of free charge carriers is established close to the contact. This effect lowers the calculated barrier and broadens the peak in efficiency compared to the Al-device.
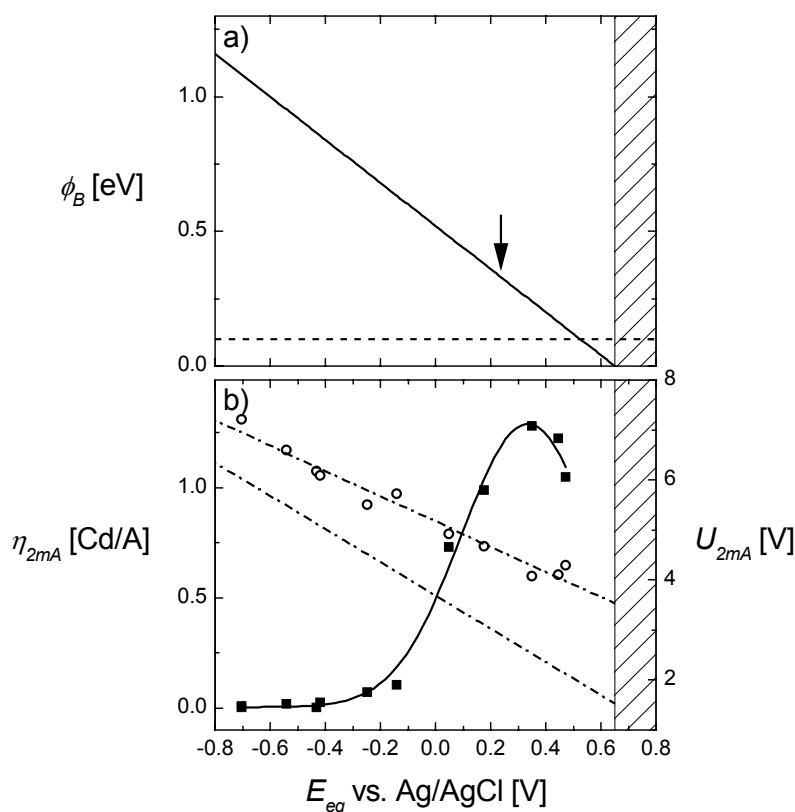
Figure 5-17: Characterization of **Ca**-OLED devices of the general structure PEDOT(E_{eq})/MDMO-PPV/**Ca** in dependence of the equilibrium potential E_{eq} of the PEDOT layer.
a) Barrier heights estimated from the UV/Vis and PV measurements for holes (solid line), for electrons in the **Ca**-device (dashed line), the arrow indicates potential of commercial PEDOT;
b) Efficiency of the **Ca**-devices at a current of 2mA (solid squares; left axis); the solid line is a guide to the eye. Operating voltage of the devices (open circles; right axis). The dash dotted line is a linear fit to the data. The dashed line indicates the BIFC voltage (see text).

The operating voltages of the devices (open circles; right axis) are also plotted and the dashed line indicates the built-in field corrected voltage. The respective built-in field changes with a changed PEDOT doping level. For E_{ox} = 0.65 V the built-in field is $V_{oc,max}$ = 2.0 V according to the extrapolated value from Figure 5-8b).

There is an obvious optimum value for E_{eq} to yield the most efficient OLED within the respective series. The devices driven at a constant current never fall below the electric field strength (35 V/µm), for which efficiency levelling was observed by Blom et al. on the similar PPV-derivative.[75] For the Al-devices a sharp optimum efficiency (0.06 Cd/A) is observed at $E_{eq} \approx$ -0.25 V. The experimental optimum for the Ca-devices occurs at $E_{eq} \approx$ +0.35 V (1.4 Cd/A).

5.2.3   Efficiency Calculated from Charge Carrier Contributions

The efficiency of an OLED is determined by the spin statistics, i.e., the probability to form singlet or triplet excitons,[113] the photoluminescence (PL) quantum yield (the probability that a singlet exciton emits light), waveguide losses,[114] which are due to light leaving the device perpendicular to the surface (compare "glowing" edge in Figure 4-6), and finally the recombination efficiency of charge carriers, η_{rec} (see chapter 4.2.3). All contributions except the recombination efficiency are kept constant for the devices studied here. According to Bäßler[115] et al. in zero-order approximation the bimolecular η_{rec} scales with the product of hole and electron charge carrier densities. Assuming uniform densities throughout the device η_{rec} is proportional to the product of the respective currents, I_h and I_e.

The Al-devices are expected to have ILC conditions for both types of charge carriers at least for the potential range where the optimum in efficiency is observed. Therefore, an optimum in efficiency can be expected for identical barriers, if any influence of different mobilities of the carriers is neglected. Following the estimations of the barriers (Figure 5-15a), this situation is fulfilled for $E_{eq} \approx$ -0.30 V, in reasonable agreement with the experimental results (-0.25 V, Figure 5-15b). The sharpness of the peak is particularly striking, but it agrees with the Fowler-Nordheim formalism,[116] despite the fact that the latter has only limited applicability to organic materials (see also next chapter).

Due to a low electron injection barrier for the Ca-devices the respective electron current is space charge limited, and therefore the simple consideration about the barriers is invalid. Nevertheless, the electron current I_e can be obtained by subtracting the hole current from the total current.

$$I_{e,Ca}(E_{eq}, U_{2mA,Ca}(E_{eq})) = 2 \text{ mA} - I_{h,Ca}(E_{eq}, U_{2mA,Ca}(E_{eq})) \tag{5-5}$$

$U_{2mA,Ca}(E_{eq})$ is the built-in-field-corrected (BIFC) voltage (= $U - U_{bi}$; dashed line Figure 5-17b), which is necessary to pass 2 mA current through the Ca-

devices for a certain E_{eq}. A certain simplification was made assuming that bipolar SCLC's equal the sum of electron and hole current, although space charge effects might lead to slight changes.[116]   The hole current can be estimated by the following assumptions: Firstly, for a given E_{eq} and a given BIFC-voltage the hole injection conditions should be identical in the Al- and Ca-devices. In other words the hole current should be identical in both types of devices if the injection barriers on the PEDOT side and the tilt of the energy bands are identical. This assumption neglects any influence of the presence of electrons on the hole injection process. Secondly, it can be assumed that the Al-devices are "hole-only" devices at least for E_{eq} > -0.25 V, where the barrier height for holes ranges below the barrier height for electrons (Figure 5-15a). Considering hole-only conditions for the Al-device $I_{h,Ca}$ can be replaced in Equation (5-5) by the hole current $I_{h,Al}$ of the aluminium device.
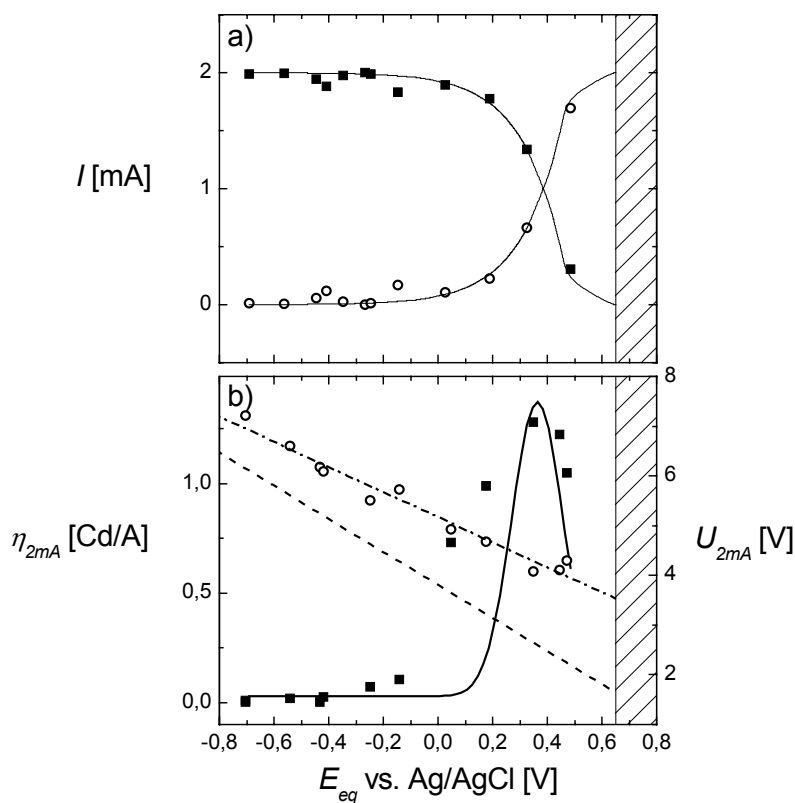
Figure 5-18: Estimation of the individual contributions of the charge carriers to the total current in **Ca**-devices.
a) Current contributions, which are necessary to calculate the current efficiency. Hole-only current I_h in **Al**-devices (open circles) and estimated electron current I_e (solid squares) obtained from the difference between the overall current in **Ca**-devices I_h (see text for details). The lines are guides to the eye.
b) Same graph as in Figure 5-17b), but plotted together with calculated current efficiency (solid line)

Accordingly, the individual hole and electron currents for the Ca-device are obtained as displayed in Figure 5-18a). As expected, I_h increases with increasing E_{eq} due to the continuously reduced injection barrier. This is

despite the decreasing voltage for reaching the constant current level. Due to the increasing hole contribution to the constant current of 2 mA the electron contribution decreases accordingly. As a zero-order approximation for η_{rec},[115] the product $I_h I_e$ is plotted in Figure 5-18b). There is a good agreement with the experimental data concerning the optimum position (+0.35 V), although disparate mobilities for charge carriers ($\mu_h \gg \mu_e$) or screening effects (zero-order approximation) are neglected.

However, the experimental optimum peak is much broader than the simple product of current contributions. This fact is attributed to an increased field caused by space charge effects of electrons, which enhance the hole injection in the Ca-devices rather than in Al-device, in which currents are IL.

The optimum efficiency of the Ca-devices with electrochemically deposited PEDOT is about half the value for the reference device using commercial spin coated PEDOT/*Baytron P®* ($\approx$ 3 Cd/A; not shown). This finding may be a result of a higher PEDOT film thickness (100 nm compared to 20 nm), yielding higher absorption losses, and the higher surface roughness of the electrochemically deposited PEDOT films as determined by AFM (10 nm compared to 2-3 nm for *Baytron P®*). Note, that the work function of *Baytron P®* is close to the one necessary to obtain optimum performance in the Ca-devices (compare Figure 5-8a) and Figure 5-17a)).

5.2.4 Fowler Nordheim Formalism

The results of a tuneable efficiency are in accordance with further theoretical calculations. Using the Fowler-Nordheim equation,

$$ j_{FN} = \frac{q^3}{8\pi h \phi_B^0} E^2 \exp\left(-\frac{8\pi (2m^*)^{1/2} \left(\phi_B^0\right)^{3/2}}{3qh} \frac{1}{E} \right), \tag{5-6} $$

electron and hole current densities were calculated separately and plotted against E_{eq} of the PEDOT layer in Figure 5-19. For the *electron* current density a constant energy barrier ϕ_B was assumed according to the difference between the MDMO-PPV LUMO-level and the work function of the used metal. For the *hole* current density the Kelvin probe result could be applied. Thus, 0.8 times the PEDOT E_{eq} as potential dependent barrier was used, which was shifted to zero for the ohmic contact at the MDMO-PPV oxidation potential of 0.65 eV according to Equation (5-2). The electric field strength E was calculated from the measured voltage for 2 mA, which was already plotted in Figure 5-15 and Figure 5-17.

Then a theoretical efficiency was calculated from the hole and electron current densities assuming a bimolecular reaction:

$$ \eta \propto \frac{j_e \cdot j_h}{j_{tot}} \tag{5-7} $$

The calculated efficiencies for Ca and Al-devices are plotted in Figure 5-19a) and b) (solid line) together with the experimental results. Their peaks mark the same positions as the experimental data, which is due to the used barrier assumption. The Fowler Nordheim equation is best suited for higher electrical field strengths. And indeed, the sharp peak for the Al-device, which is in accordance with the experimental shape, pronounces that Fowler-Nordheim is better suited for IL (Al-devices) rather than SCL conditions (Ca-devices). The fact that the measured efficiency does not drop down to zero akin the Fowler-Nordheim prediction is most likely due to noise. Mathematically the measured efficiency cannot be zero since the brightness of the emitted light is divided by the total current and both properties were non-zero for these devices. The current density of the Fowler-Nordheim plot is displayed in arbitrary units (y-axes in Figure 5-19) since the amount of current is different from the measured current. The actual current is not necessary in order to discuss the shape of the resulting efficiency profile. However, it was ensured that hole and electron currents were obtained by the same method (FN).
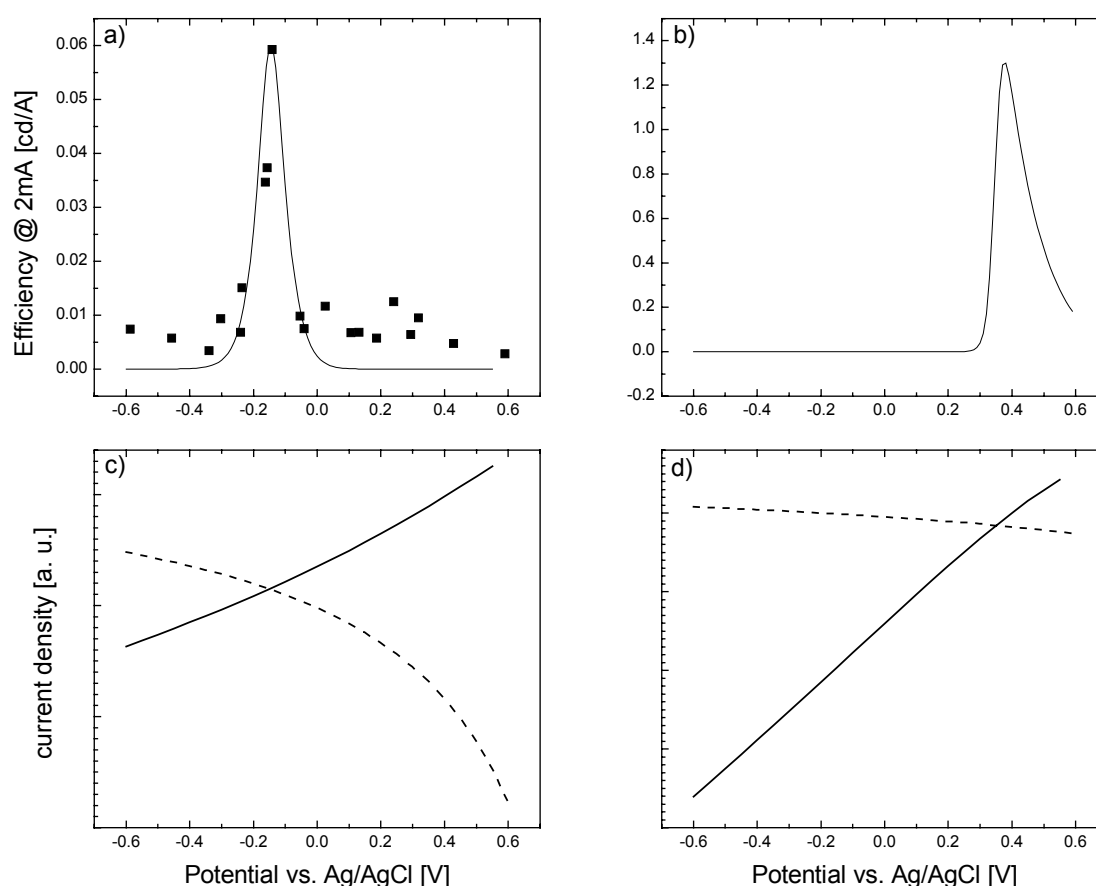
Figure 5-19: Fowler Nordheim calculations: Every graph is plotted against the E_{eq} of the adjusted PEDOT layer. The left graphs belong to the Al-device, the right graphs to the Ca-device;
a) + b) Efficiency at a current of 2 mA (solid squares), needed voltage to reach this current (open circles), efficiency calculated from Fowler Nordheim plots (solid lines)
c) + d) current densities using the Fowler Nordheim equation for holes (solid lines) and electrons (dashed lines), respectively.

5.3 Influence of an Altered Anodic Work Function on OSC's

In this chapter bulk-heterojunction OSC's (for details see Chapters 4.3.2 and 7.3.1) containing differently doped PEDOT anodes were investigated. Similar to the results already achieved for OLED's an influence on the device properties was expected.

5.3.1 Photovoltaic Measurements
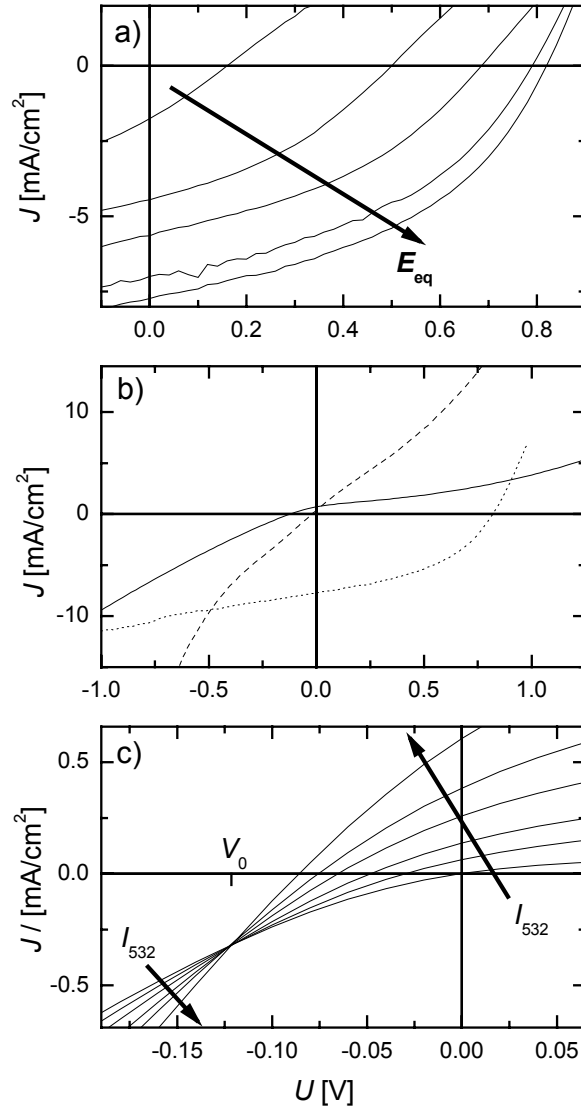
Figure 5-20: J-V curves of OSC devices of the general structure PEDOT(E_{eq})/MDMO-PPV:PCBM/Al in dependence of the equilibrium potential E_{eq} of the PEDOT layer.

a) E_{eq} of PEDOT layer following the arrow: -0.21 V, -0.01 V, +0.18 V, +0.39 V and +0.53 V vs. Ag/AgCl; I_0 = 200 mW/cm^2 (532 nm).

b) E_{eq} of PEDOT layer: -0.81 V ("inverted" OSC; solid line), -0.57 V ("zero-built-in-field" OSC; dashed line), +0.53 V ("normal" OSC; dotted line). I_0 = 200 mW/cm^2 (532 nm).

c) "Inverted" OSC (V_{bi} = -0.12 V), I_0 = 0 mW/cm^2, 45 mW/cm^2, 70 mW/cm^2, 120 mW/cm^2, 200 mW/cm^2, and 330 mW/cm^2 (532 nm; sequence is indicated by the arrows).

Bulk-heterojunction OSC's consisting of PEDOT films with varying oxidation levels have been illuminated with a 532 nm laser. Figure 5-20 shows J-V-curves of the illuminated devices. The incident laser intensity for (a) and (b) was I_0 = 200 mW/cm^2. Obviously, the open-circuit voltage V_{oc} of the devices increases with an increasing oxidation level of the PEDOT layer (slope 0.8) – the sequence of rising oxidation potentials is indicated by the arrow in Figure 5-20a).

Figure 5-20c) shows J-V-curves of a device with a low built-in-field. This device has been illuminated with several intensities I_0 between 0 and 330 mW/cm^2 (sequence is indicated by arrows). It is remarkable that the respective J-V-curves do not pass the x-axis at a single V_{oc}, but that they seem to have another common data point at which the current density is independent of the incident light intensity I_0. The current at this particular voltage is not zero, but has a finite value. Instead V_{oc} does change with I_0 unlike in OSC's with a higher PEDOT E_{eq}, for which a levelling of V_{oc} can be observed after a certain saturation illumination is reached. The dark current (I_0 = 0) also coincides with all other data sets at the common data point, which is an indication that there is a current contribution to the overall photocurrent originating from charge injection processes rather than from photogenerated charges. Recognizing that this current contribution plays an important role at least for small $\Delta\phi_W$ the known nomenclature V_0 for the compensation voltage is adapted at which the *net* photocurrent (the photocurrent minus the dark current) is zero.[108]

5.3.2   Electrochemical Interplay of Involved Polymers

Figure 5-21a) shows the dependency of the compensation voltage V_0 on E_{eq}. Again a linear dependence with a slope of 0.8 was obtained akin the photovoltaic studies carried out for OLED devices using pure MDMO-PPV (compare Chapter 5.1.4). This fact emphasizes that the ϕ_W of the PEDOT layer is not pinned to any of the energy levels of the active layer blend. However, the PV results deviated from the linear dependency (Figure 5-21a) whenever E_{eq} of the PEDOT anode approached or even exceeded the oxidation potential E_{ox} of MDMO-PPV, which was determined by cyclic voltammetry in solution (Figure 5-21c). Again, this fact is attributed to redox reactions across the interface between MDMO-PPV and the highly oxidized PEDOT layer. Due to these redox reactions, the range $E_{eq} > E_{ox}$ cannot be utilized for device operation (shaded area in Figure 5-21a). In contradiction, passing the reduction potential of PCBM (Figure 5-21d) does not seem to harm V_0, although PEDOT dedoped below the reduction potential of PCBM could have the ability to reduce the PCBM across the interface in principle. This reduction does not occur and this finding can be explained in terms of missing redox states for dedoped (nearly neutral) PEDOT (compare left dashed vertical line in Figure 5-21b) and, therefore, missing counter ions, which are necessary to compensate redox reactions across the interface. Exact correlations between the redox potentials determined in solution (Figure 5-21c, d) and the situation in a real device is not possible. However,
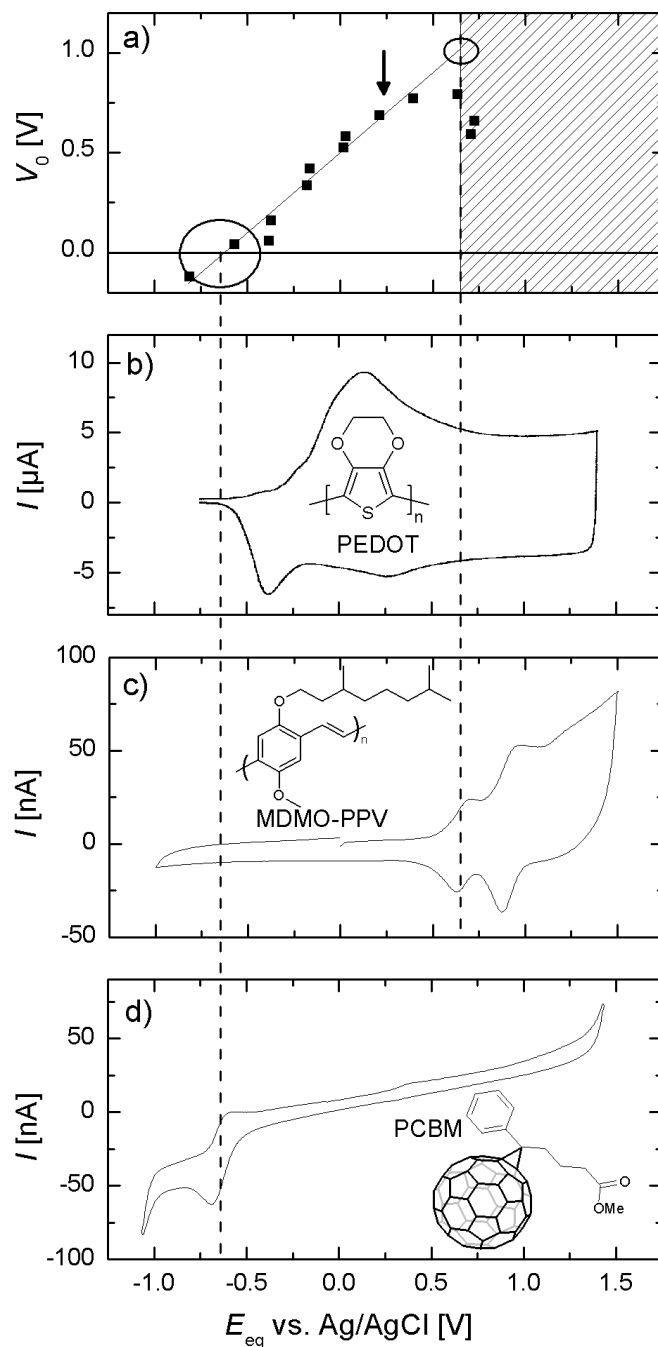
Figure 5-21: Comparison of OSC device performance with electrochemical properties of involved compounds.

a) Compensation voltage V_0 in devices PEDOT(E_{eq})/MDMO-PPV:PCBM/Al as a function of the pre-adjusted E_{eq} of the PEDOT layer. The shaded area indicates a potential range, in which PEDOT is able to oxidize MDMO-PPV acros their interface (see "doped" OSC's). The arrow indicates the commercial PEDOT (Baytron®).

b) Cyclic voltammogram of a PEDOT-film atop the Pt work electrode in acetonitrile with tetrabutylammonium hexafluorphosphate (TBAPF$_6$, 0.1 M). The scan rate was v = 10 mV/s .

c) Cyclic voltammogram of MDMO-PPV in methylene chloride with TBAPF$_6$ (0.1 M), v = 100 mV/s. The right-hand vertical dashed line indicates the first oxidation potential (defining the beginning of "forbidden" potential range).

d) Cyclic voltammogram of PCBM in methylene chloride with TBAPF$_6$ (0.1 M), v = 100 mV/s. The left-handed vertical dashed line indicates the first reduction potential.

electrochemical investigations of solid films of the respective materials will be similarly problematic due to slow electron transfer kinetics, generally leading to scan-rate dependent overpotentials.

5.3.3 Device Properties as a Function of the Internal Field

In Figure 5-22 the key device properties of the OSC's are displayed. Here they are plotted against the experimentally determined V_0 rather than against E_{eq} (compare Figure 5-21), since V_0 enables direct energy considerations, whereas E_{eq} is an impractical and indirect value in terms of device properties. For V_0 = 0, all characteristic device parameters are zero, since the driving force for transportation of photogenerated charge carriers is missing. In this case the respective device exhibits a built-in flat band condition. The open squares display the properties for the spincoated Baytron® PEDOT.

In Figure 5-22a,b) the absolute short-circuit current density J_{sc} and the fill factor FF increase monotonically with increasing V_0 unlike the energy conversion efficiency η_{conv} (Figure 5-22c), which remains negligibly small for V_0 < 0.3 V and only then increases, reaching a maximum of about 2 percent shortly before reaching the hatched area. The origin behind the onset behaviour seems to be related to the absence (V_0 > 0.3 eV) or presence (V_0 < 0.3 eV) of injection currents (Figure 5-20c) in the devices. These injection currents arise if the barrier for injected charge carriers is low *and* if the bands are tilted to a favourable direction in the voltage range of OSC operation (|U| < V_0). Any light-independent contribution to the overall current will reduce the devices efficiency.

The reference device using a Baytron® PEDOT anode yields V_{oc} = 0.74 V, J_{SC} = 6.5 mA/cm^2 (200 mW/cm^2 @ 532 nm), FF = 0.4, and η = 1.4 % (open squares in Figure 5-22). The differences in device performance are attributed to differences in the experimental procedure (laser illumination here vs. AM1.5 in Ref. [80]) as well as the morphology of both the PEDOT and the photoactive layers. If the V_{oc} data is extrapolated to E_{eq} = $E_{ox,PPV}$ an open circuit voltage of $V_{oc} \approx$ 1.0 V, and a short circuit current density of $J_{SC} \approx$ 8 mA/cm^2 can be gained. The corresponding fill factor was $FF \approx$ 0.44, and the efficiency $\eta \approx$ 2 %. This results indicate a substantial overall improvement over the reference device using commercial PEDOT. Katz et al. had reported $V_{oc} \approx$ 1.2 V for temperatures below 200 K,[118] We attribute the difference to the disparate temperature at which the experiments were performed (room temperature here vs. liquid helium conditions in Ref. [118]).

5.3.4 Energy Conditions Inside Differently Doped Devices

Four energy situations in the devices depending on the PEDOT doping level will be discussed in more detail. Typical OSC's exhibiting relatively large open-circuit voltages and short-circuit currents (#1). Two novel device types will be presented subsequently, which are a "zero-built-in-field" OSC's (#2) and an "inverted" OSC's (#3). Finally, OSC's which experienced redox-
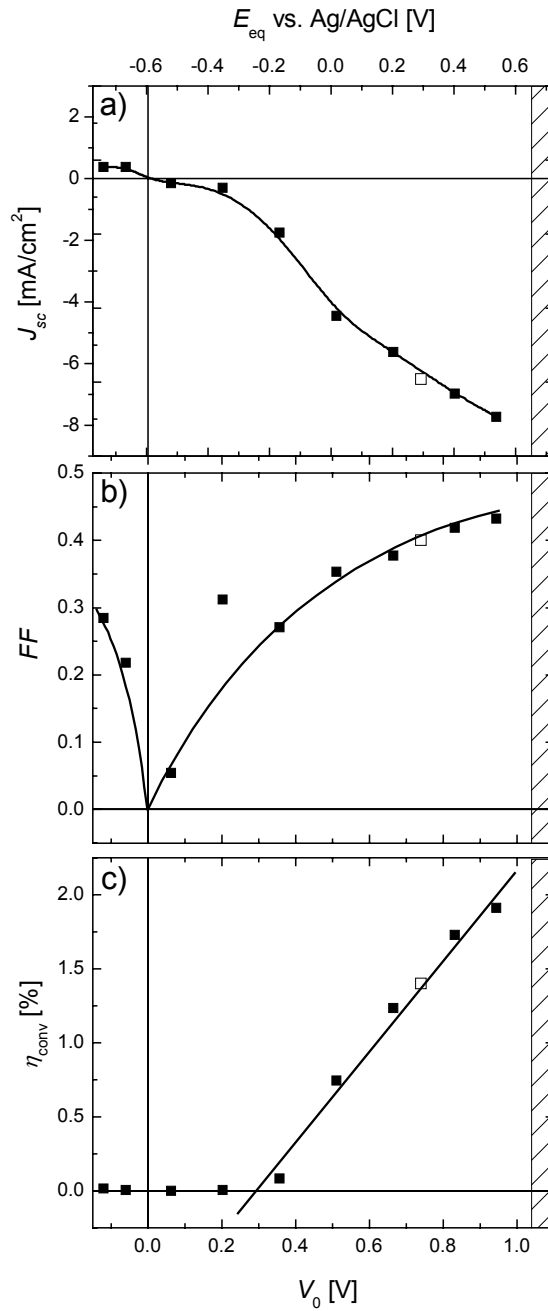
Figure 5-22: Dependence of OSC properties on the built-in voltage V_0 (bottom axis) and E_{eq} (top axis), respectively, in OSC devices of the general structure PEDOT(E_{eq})/MDMO-PPV:PCBM/Al (I_0 = 200 mW/cm^2 @ 532 nm). The lines are guides to the eye. a) Short circuit current density J_{sc}; b) Fill factor FF; c) Energy conversion efficiency η_{conv}.

reactions across the PEDOT/MDMO-PPV interface are discussed (#4). Although all of these devices apart from the normal devices (#1) are of limited practical use, they are of high scientific interest for the understanding of the device physics.

Typical OSC's (#1) with a high built-in-field are commonly built using a highly doped PEDOT layer as the polymeric contact. This aim can, for example, be

realized by using commercial PEDOT (see arrow in Figure 5-22a). Due to the relatively large difference in work functions of the two contacts (Figure 5-23, Ia) these normal OSC exhibit the strongest diode rectification among the devices studied here. The injection current for holes and electrons in the operating range relevant for OSC's ($U < V_0$) is negligible due to the tilt of the levels in the unfavourable direction (see Figure 5-23, Ic).

The measurements presented in Figure 5-21 verify that the built-in field V_{bi} becomes zero when E_{eq} of the PEDOT contact equals the PCBM reduction potential (Figure 5-22a; $E_{eq} = E_{red,PCBM}$). This finding proves that the pinning of thermally evaporated metal cathodes[106b] occurs exactly at the PCBM LUMO level and not below. Zero-built-in field OSC's (#2) exhibit ohmic contacts for electrons at both electrodes (see Figure 5-23, II). The corresponding symmetrical energy diagram is responsible for symmetrical electron current observed in Figure 5-20b - holes are blocked due to the high injection barriers. Nevertheless, the total (electron-only) current is even higher than for other devices, since the barrier for electron injection is zero for both directions of biasing. SCL electron-only currents passing the PCBM LUMO are responsible for this high symetrical current.

Dedoping the PEDOT-layer below the PCBM acceptor level ($E_{eq} < E_{red,PCBM}$), resulted in devices for which J_{sc} and V_0 have opposite signs compared to normal OSC's. Energetically the PEDOT contact became the cathode rather than the usual anode. This finding gives evidence for the fact that dedoped PEDOT can serve as cathode unlike in normal OSC's or organic light-emitting diodes (OLED's), where highly doped PEDOT layers typically serve as the anodic contact. The inverted OSC's have a small internal barrier for photogenerated electrons leaving at the PEDOT contact (see Figure 5-23, IIIb). Therefore, the total current is reduced compared to the zero-built-in field device. Due to the absence of more negative redox states in the PEDOT (Figure 5-21b) devices with $V_0 < -0.12$ are experimentally not accessible. However, even if a π-conjugated polymer with such negative redox states existed, doping problems can be expected similar to those anticipated for high doping levels of the PEDOT.

The devices, for which the PEDOT-layer exceeded the oxidation potential of the MDMO-PPV ($E_{eq} > E_{ox,PPV}$), exhibit redox processes between the PEDOT and the adjoining MDMO-PPV layer. Thermodynamic reasons lead to an exchange of charges. Thus, the MDMO-PPV becomes oxidized and the PEDOT reduced until an equilibrium state is reached. As a result the reduction of the PEDOT layer is accompanied by a reduction of E_{eq} and thus ϕ_w. In addition even slight oxidation of the MDMO-PPV may cause a higher conductivity[25] and result in an additional non-intensity-dependent current. Both factors lead to the reduction of the OSC performance parameters, and thus explain deviations from the linear dependence in Figure 5-20a) as well as the "forbidden" range for $E_{eq} > E_{ox,PPV}$.

Figure 5-23 shows simplified energy diagrams of the mentioned devices enabling direct comparison. The metal electrode (aluminium) always provides ohmic contacts for electrons due to the pinning effect.[119-120] Therefore,

electrons are injected from the Al side under reverse bias in all devices. Injection of electrons from the PEDOT may occur in OSC's with $V_{bi} \approx 0$, even under forward bias. The injection of holes by the PEDOT only comes into play for highly doped PEDOT, i.e., in normal OSC's for $U > V_0$.
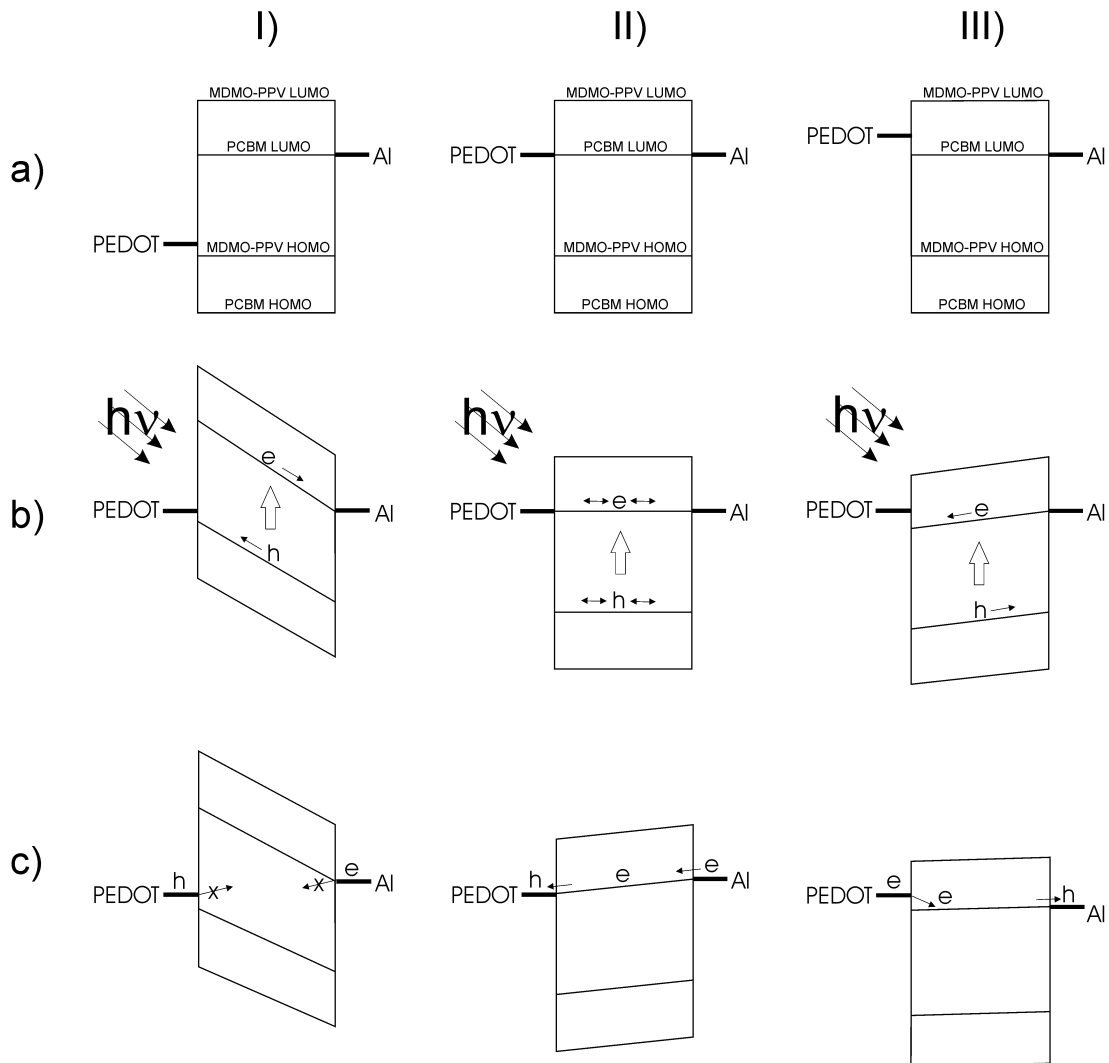
Figure 5-23: Idealized energy diagrams for OSC devices

I)   typical OSC.

II)   zero-built-in-field OSC.

III)   inverted OSC.

a)   open-circuit conditions ($U = V_{bi}$).

b)   short-circuit conditions under illumination ($U = 0$ V).

c)   (dark) injection; a small external voltage was "applied" in forward direction.

5.4 Estimated Range of Adjustable PEDOT Work Functions

Since the exact correlation between the electrochemical equilibrium potential and the PEDOT work function for the investigated films has not been given so far, the accessible energy range will be determined in the following. It is a great advantage that two energy levels coincide with already determined potentials:

1) The HOMO level of MDMO-PPV is given by the first oxidation peak of the respective cyclic voltammogram (beginning of the 'forbidden' potential range).
2) The LUMO level of PCBM is given by the first reduction peak, which coincides with the zero crossing of the V_{oc} measurement.

The following table gathers the involved energy levels and their known electrochemical counterparts.

	Energy level	E_{eq}	correlation
LUMO MDMO-PPV[79]	2.8 eV	-	
LUMO PCBM[79]	3.7 eV	-0.65 V	zero-crossing of V_{oc}
zero-crossing[26]	4.45 eV	0 V	generally assumed
HOMO MDMO-PPV[79]	5 eV	0.65 V	beginning of 'forbidden' range
HOMO PCBM[79]	6.1 eV	-	

Figure 5-24 shows the three allocatable energy levels in one graph. The *linear regression*, which was forced to a slope of 0.8, passes nearly exactly the given energy levels:

$$\phi_w = 4.4\ eV + 0.8\ eE_{eq}$$
(5-8)

The slope is 0.8 according to the Kelvin probe and photovoltaic measurements. For comparison purposes the dashed line in Figure 5-24 indicates the generally assumed slope of 1 eV/V. Note that 4.4 eV is *not* the correlation between the electrochemical potential and the vacuum energy scale ("offset"), but a result of the linear regression. According to the lowest and highest adjustable electrochemical potentials for PEDOT used in organic devices, which range from -0.8 up to 0.7 V, the reachable work functions range from 3.75 up to 5.0 eV. Although PEDOT can be adjusted to an even larger range of electrochemical potentials (compare Figure 3-1), just the mentioned range is stable enough to remain *after* the film has been adjusted. The left end of this adjustable range is given by missing redox states for $E_{eq} <$ -0.8 V and the right end is given by a subsequent film reduction after a highly oxidized film is removed from solution and during the drying process with clean nitrogen.

For the C_{60}-Pd-films the adjustable range is even larger (-0.93 up to 1.3 V) and their work functions start at 3.65 eV rising up to 5.44 eV.
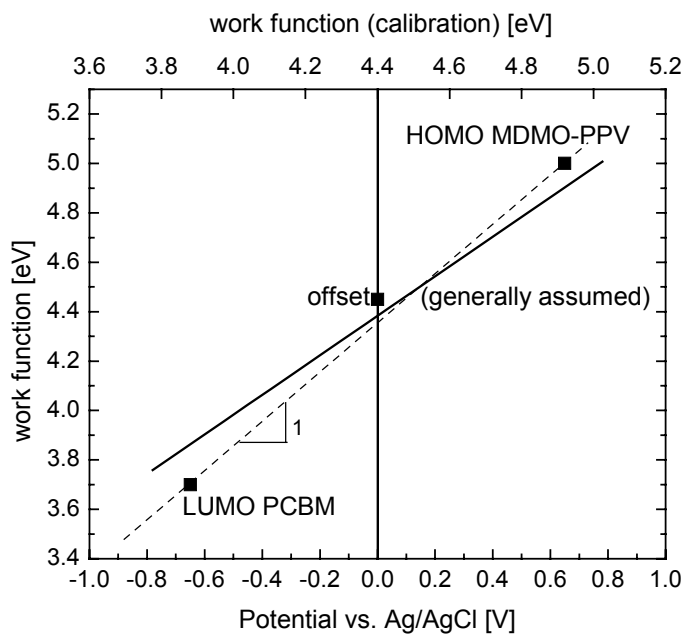
Figure 5-24: Energy calibration for PEDOT films. The calibration of the linear regression with a slope of 0.8 (solid line) is translated to the upper x-axes, which displays the corresponding energy values for the potentials of the lower x-axes. For comparison purposes the dashed line indicates the generally assumed slope of 1 eV/V.

5.5 Evidence for Surface States at PEDOT Layers in Air

In this chapter, results for identical device architectures are reported, which were fabricated in air. In contrast to the devices fabricated in N_2 (chapter 5.2 and chapter 5.3), the devices fabricated in air exhibit very little change in V_{oc}, but do demonstrate a systematic change in I_{sc}. These results are explained in terms of the creation of a reacted layer at the PEDOT/MDMO-PPV interface.

5.5.1 Photovoltaic Measurement of Devices Produced in Air

Figure 5-25 shows a typical set of IV-curves for four **ITO / PEDOT(E_{eq}) / MDMO-PPV / Al** cells prepared in air and initially doped at electrochemical potentials E_{eq} of -0.8 V, -0.5 V, +0.3 V, and +0.7 V vs. the Ag/AgCl reference electrode. The data indicate that while there is very little variation in V_{oc} between the four solar cells ($\approx$50 mV), there does appear to be a correlation between the measured I_{sc} and the doping voltage.
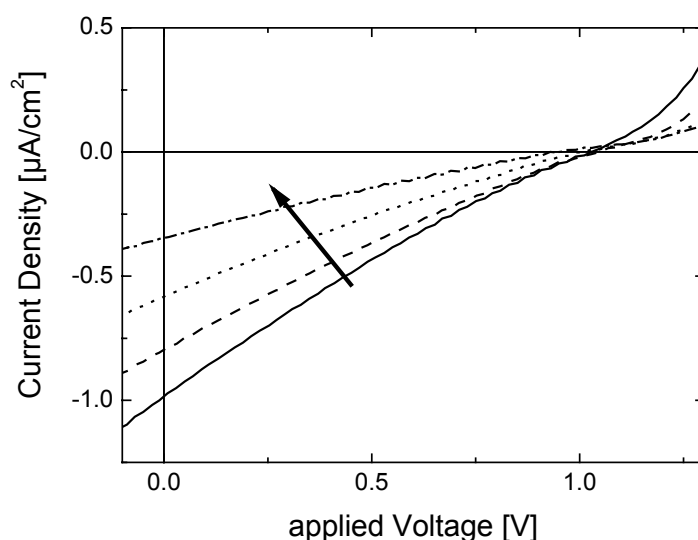
Figure 5-25: IV-curves of ITO / PEDOT(E_{eq}) / MDMO-PPV / Al solar cells illuminated with a quartz halogen lamp at a power density of 60 mW/cm^2, sequence of further dedoped films is indicated by the arrow (E_{eq}: + 0.7 V, + 0.3 V, − 0.5, and − 0.8 V)

The same trends for both V_{oc} and I_{sc} with doping voltage were observed consistently from substrate to substrate.

5.5.2 AFM and EFM Measurements

Therefore, PEDOT films were investigated in air by direct measurements of the *CPD* using an EFM (chapter 3.4) across the border between a doped and an undoped region of PEDOT. This border was searched using the optical microscope of the AFM setup, which gave a rough orientation where to approach the tip. Then the scan field was shifted as long as the border came into the focus. In order to get accurate results the border was investigated with

different scan angles (0°, 90°, and 270°; see Chapter 3.3) and with different sizes of the scan fields (30 x 30µm, 20 x 20 µm, and 10 x 10 µm)
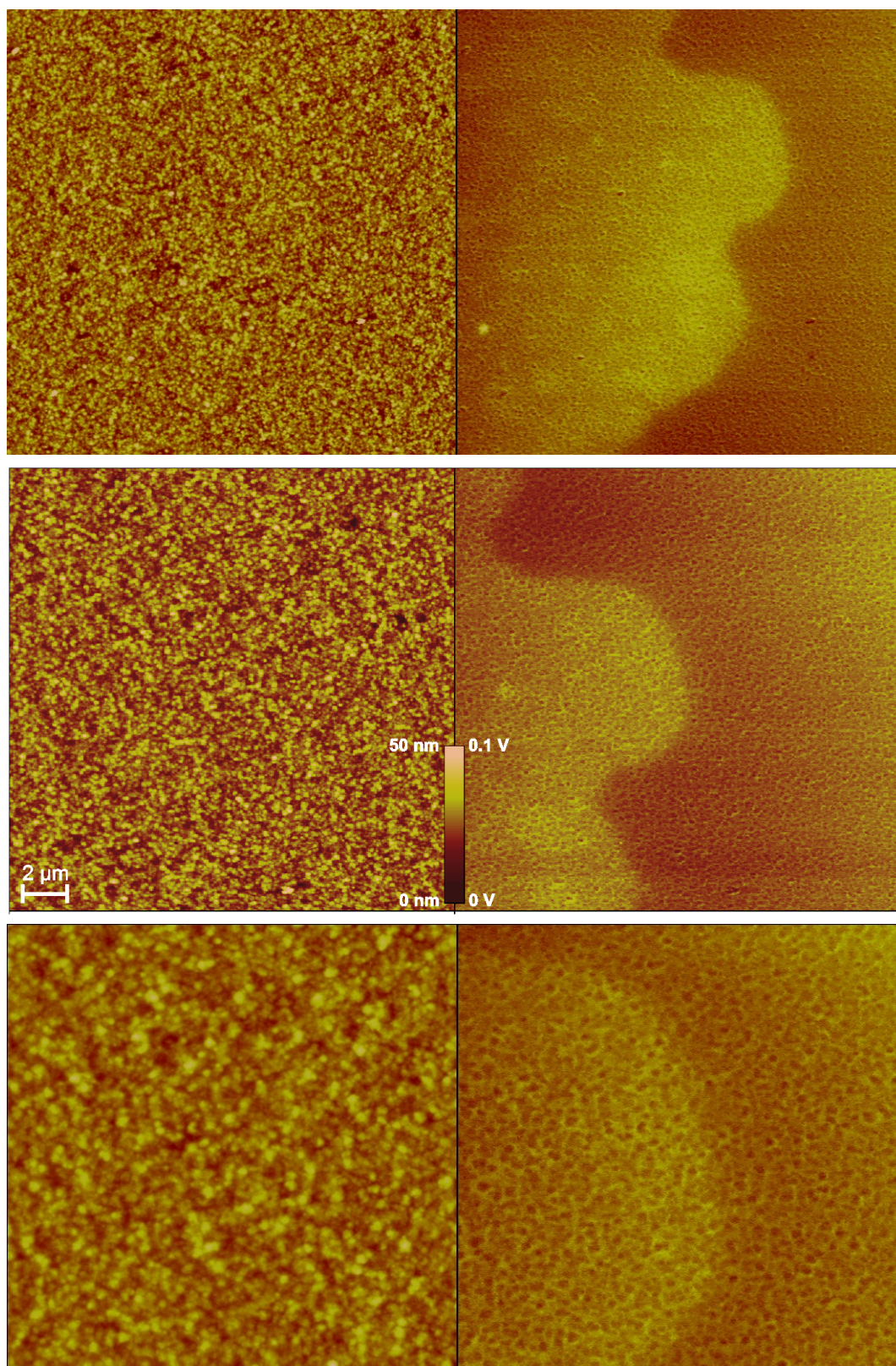
Figure 5-26: AFM-images (left) and EFM- images (right) of the same PEDOT film area: 30 x 30 µm (0°), 20 x 20 µm (90°), and 10 x 10 µm (270°). The right part of the film was dedoped.

Figure 5-26 shows both the AFM images (morphology) and EFM images (*CPD*). The border is only discernable in the EFM image, thus confirming that the electrochemical contrast observed is a consequence of the *CPD* rather than from any topographical changes in this region. There is a distinct correlation on a smaller scale between the morphology and the surface potential. "Hills" seem to have a lower doping level (darker in EFM-image), whereas "valleys" seem to exhibit higher doping levels (brighter in EFM-image). It is difficult to find out if this interplay is an artefact or caused by a real surface potential distribution. Nevertheless, the step in surface potential across the doping border is sufficient for the conclusions made here.

Quantitative analysis of line scans across the two regions reveals that the difference in *CPD* between the two regions is approximately 50 mV akin the V_{oc} measurements. This potential difference is an order of magnitude smaller than the anticipated difference in ϕ_W between the two regions according to measurements in nitrogen.

These results are in contradiction with earlier results which have clearly demonstrated that for solar cells prepared in inert atmospheres the V_{oc} is linearly dependent upon E_{eq} of the doped PEDOT layer with a slope of 0.8.

5.5.3 UV/Vis Measurements

Conjugated polymers are known to change their degree of oxidation when exposed to air and moisture, which for example has been utilized in redox-sensors.[6]
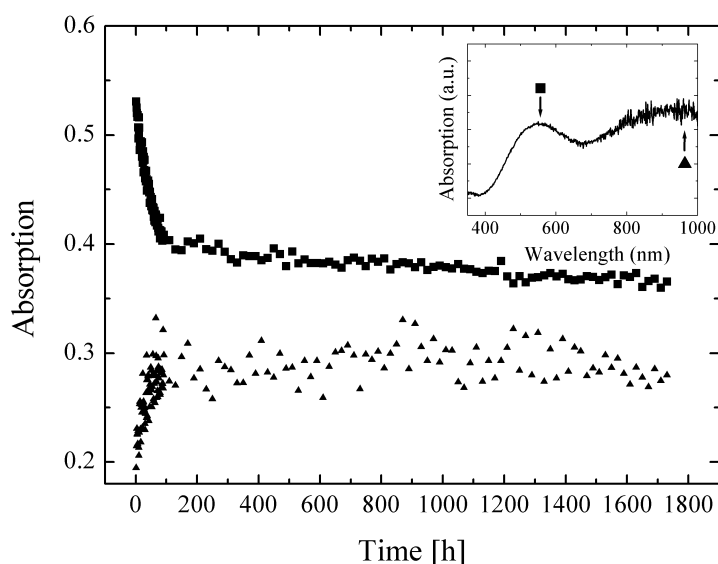
Figure 5-27: Time resolved absorption measurement (every minute for 2 hours and, thereafter, every 20 min for another 30 hours) in air of an initially dedoped PEDOT film deposited on ITO-glass at wavelengths of the HOMO-LUMO transition (solid squares) and of inter-gap doping states (solid triangle). Inset: whole spectrum, solid square and triangle mark the peaks of interest (investigated wavelengths).

Figure 5-27 shows the temporal development of the absorption at 560 nm (corresponding to the HOMO-LUMO transition of the non-doped PEDOT) and 970 nm (stemming from doping-induced mid-gap states) of an initially dedoped film. Clearly, the absorption at 560 nm decreases, while it increases at 970 nm, indicating that the PEDOT layer is oxidized. It can be presumed that this is due to a redox reaction with oxygen. Saturation is reached for both peaks after 2 hours. The total absorption changes during air exposure amount to $\approx$ 20 %, thus taking into account the film thickness of about 100 nm the thickness of the reacted layer can be estimated to about 20 nm at the most.

Thus, it seems highly probable that a reacted surface layer forms on the PEDOT film upon exposure to air. Electronically, this thin layer will provide a fixed ϕ_W (independent from the initial bulk doping level) at the PEDOT – conducting polymer interface that causes the Fermi level of doped PEDOT layer to end up at a fixed position regardless of the initial (homogenous) doping level. As such, little variation in ϕ_W is observed. For the solar cells prepared in inert atmospheres, this interfacial layer is not formed, and ϕ_W of PEDOT is not tied to a fixed position.

5.5.4   Kelvin Probe Measurements

This assumption is supported by Kelvin probe measurements (Figure 5-28b). The same saturation time of about 2 hours akin the UV/VIS experiments is confirmed by Kelvin Probe measurements performed in air. The slope of *CPD* plotted against E_{eq} immediately after doping the PEDOT film shows the known slope of 0.8 (solid circles), but during exposure to air the *CPD*-slope drops via 0.6 after 5 minutes (triangles) down to almost zero after 36 hours (solid squares). The same result was obtained by calculating the average *CPD* of EFM-images in initially homogenously doped areas after 2 hours in air (open squares). It is particularly noteworthy that spin coated commercial PEDOT (solid star) exhibits a *CPD* very close to the value all other samples approach after having been exposed to air. Irreproducible results were obtained whenever the ϕ_W of PEDOT exceeds the oxidation potential of MDMO-PPV (compare right-hand solid circle) in Figure 5-28a). Such observations were not made after the PEDOT was exposed to air, which can be attributed to the fact that the interfacial layer provides a doping level below the oxidation potential of MDMO-PPV in accordance with our Kelvin probe measurements.
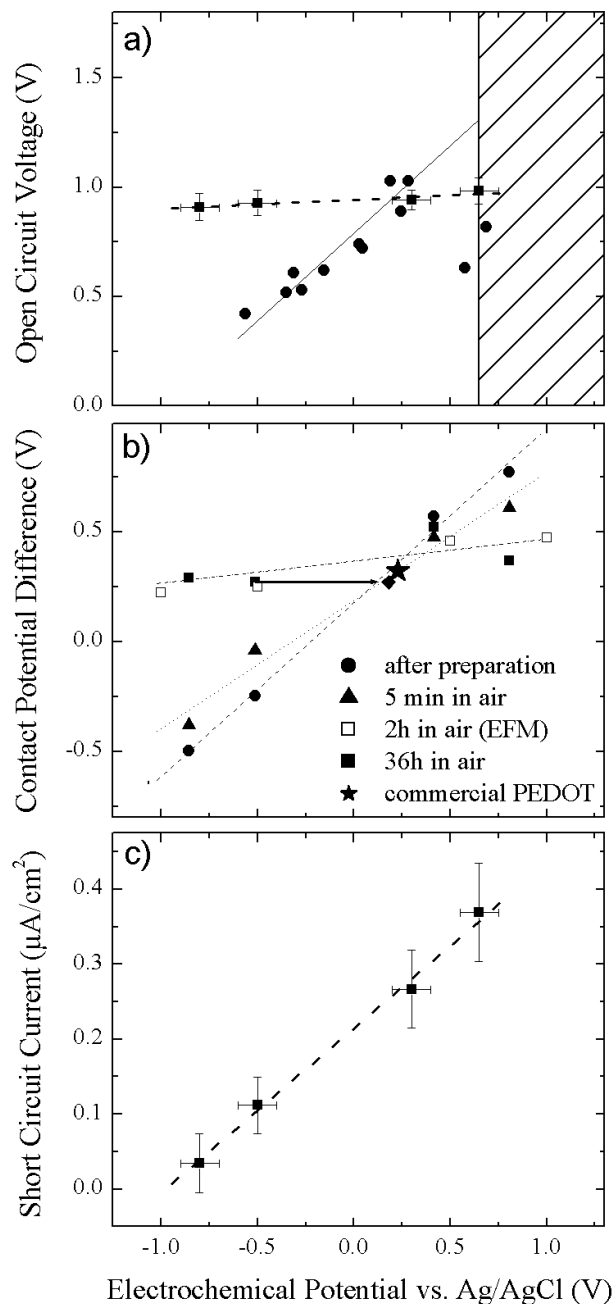
Figure 5-28: Property differences of devices (ITO / PEDOT(E_{eq}) / MDMO-PPV / Al) prepared in N_2 and air, respectively

a) open circuit voltages of devices prepared in inert atmosphere (discs) and of devices prepared in air (solid squares).

b) Kelvin-probe measurements of adjusted PEDOT films. The initial slope of 0.8 is tilted horizontal to nearly zero after 2 hours.

c) short circuit currents of devices prepared in air shows a pronounced slope.

5.5.5 Energy Alignment of Fermi and Vacuum Levels

The energy level alignment diagram for the two situations (inert gas or air) is illustrated in Figure 5-29. Previous UPS measurements have shown the

existence of a Fermi edge for PEDOT and thus the energy level diagram for PEDOT is drawn as if it is a metal with a Fermi energy defined by the pre-adjusted electrochemical potential.

Figure 5-29a) shows the case for PEDOT prepared in N_2 at the most negative value of E_{eq} (Figure 5-28) resulting in a low $E_{F,eq}$. The high carrier density in the doped PEDOT material allows the Fermi levels of the ITO and PEDOT to equilibrate. However, it is the vacuum levels (E_{vac}) of the PEDOT, the Al electrode and MDMO-PPV that align as a consequence of the low carrier density for MDMO-PPV. Consequently, a low open circuit voltage (V_{oc}^1) is measured.

Figure 5-29: Schematic energy level alignment diagrams for doped PEDOT samples prepared under different conditions. a) PEDOT prepared in N_2 at $E_{F,eq}^1$, b) PEDOT prepared in N_2 at $E_{F,eq}^2$, c) PEDOT prepared in air at $E_{F,eq}^1$, and d) PEDOT prepared in air at $E_{F,eq}^2$. $E_{F,eq}^1$ and $E_{F,eq}^2$ refer to the most negative and positive values of pre-adjusted equilibrium potential (E_{eq}), respectively. E_F^{ITO} and E_F^{Al} refer to the Fermi levels of the ITO and Al electrodes respectively. CB and VB are the conduction and valence band edges of the PPV polymer.

Figure 5-29b) shows the case for PEDOT prepared in N_2 at the most positive value of E_{eq} (Figure 5-28) resulting in the lowest $E_{F,eq}$. Again, the Fermi levels of the ITO and PEDOT equilibrate whilst the E_{vac}'s of the PEDOT, the Al electrode and MDMO-PPV align. However, in this case the Fermi level of the PEDOT has increased and so a larger open circuit voltage (V_{oc}^2) is measured.

Figure 5-29c) and d) show the case for PEDOT prepared in air at the two extreme values of $E_{F,eq}$. The interface between the PEDOT and MDMO-PPV can be considered to consist of an interfacial layer whose effective Fermi level is pinned to a fixed value (E_{eq}^{ox}) by the presence of surface states. Again, the high density of states for the ITO, PEDOT and interfacial layer causes their respective Fermi levels to equilibrate, while it is the vacuum levels of the interfacial, MDMO-PPV and Al layers that align. However, although the value

of E_{eq} changes from c) to d), the presence of the interfacial layer with an almost constant work function, E_{eq}^{ox}, means that an almost constant open circuit voltage (V_{oc}^{ox}) is measured.

It is actually possible to propose a rather simple explanation for the observed increase in I_{sc} with increasing doping level (Figure 5-28c). Given that the V_{oc} of these devices is approximately constant for all doping voltages, and that increasing E_{eq} is known to lead to increased PEDOT conductivity, it seems reasonable to speculate that the observed increase in I_{sc} of the devices is simply due to the fact that the effective resistance of the PEDOT film has decreased with increasing doping level.

The change in transmission of the PEDOT layer (as revealed by the colour change) could also result in a change in the I_{sc} of the devices. However, these effects are too small to explain the experimental observations.

5.5.6   Spectral Response Measurements

Spectral response measurements were performed with PEDOT/MDMO-PPV/Al devices with differently doped PEDOT layers serving as anodic contacts.
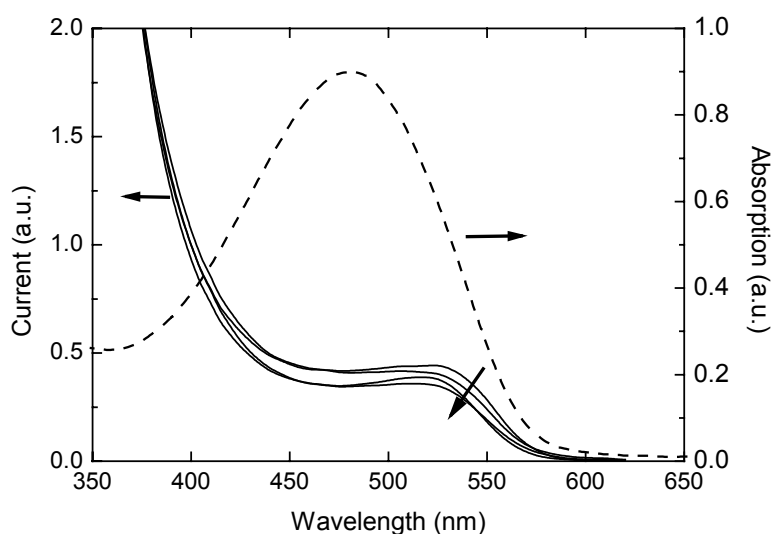
Figure 5-30: Normalised (at 375 nm) photo action spectra for solar cells with pre-adjusted equilibrium potentials E_{eq} of the PEDOT injection layer: 0.7 V, 0.3 V, – 0.5 V and – 0.8 V vs. Ag/AgCl (arrow indicates sequence of an increased doping level). Shown also is the absorption profile (ABS; dashed line) of MDMO-PPV for comparison.

It is well known for conjugated polymers in general that doping leads to increased bulk conductivity.[2] Therefore, it seems reasonable to assume that the observed increase in I_{sc} of the devices prepared in air is due to the fact that the effective resistance of the PEDOT film has decreased with increasing doping level. Qualitative observations of the PEDOT film support this hypothesis, since the PEDOT film changes colour as a function of doping voltage, in agreement with the known electrochromic response of this material (see Chapter 5.1.1), indicating that the PEDOT film's electrical conductivity

has indeed increased with increasing doping level. However, the change in light absorption (as revealed by the slight change) could also result in a change in the I_{sc} of the devices. Indeed, this electrochromic effect is observed in the normalised photoaction spectrum, since the peak at approximately 525 nm decreases systematically with doping voltage, whereas the response at about 390 nm remains constant. However, the change in PEDOT absorption as a function of doping voltage alone is insufficient to account for the significant changes in I_{sc} that are observed. Thus, it is the change in conductivity of the material, rather than its change in light absorption, which dominates the observed change in I_{sc}.

The visible "dent" in the photoaction spectra with a minimum at about 480 nm can be explained in terms of a competition between necessary absorption and remaining intensity close to the cathode. Two reasons are responsible for this filter effect:

- MDMO-PPV is a p-type semi-conducting polymer. Therefore, effective charge splitting from excitons takes place just close to the cathodic contact, since electrons are directly at their destination and holes can easily travel through the polymer film to the anode.
- The PPV between the PEDOT and the cathode filters the light. At 480 nm the highest absorption is reached. Now, the highest amount of excitons is produced, but due to the high absorption they are produced close to the anode and the resulting current is reduced.

6   Conclusion and Outlook

In conclusion, a linear correlation between the electrochemical equilibrium potential E_{eq} of a π-conjugated polymer and its work function ϕ_w has been demonstrated. This correlation could be extended to a C_{60}-derivative, which has a completely different structure.

However, unlike commonly assumed throughout the literature the slope for this linear correlation is below the ideal unity value for these materials. The surface potential determined by the Kelvin probe technique directly translates to the internal interface as determined by open-circuit potential with one constant contact, rendering *CPD* measurements a powerful tool for screening purposes.

It has been shown that the PEDOT doping level is stable for weeks inside a glovebox if it is protected by at least one other layer spincoated on top. A spincoating process does not change the oxidation potential of the PEDOT film significantly.

It was demonstrated experimentally that an OLED reaches an optimum efficiency whenever hole and electron densities are balanced. This was possible by adjusting the hole-injection properties of the polymeric anode to the given electron current, which originates from the fixed barrier at the cathode. In summary, it could be shown in this thesis that redox-chemical tuning of the anode provides a strong tool which beside OLED's allows optimization of other organic devices such as organic solar cells, organic transistors, and organic lasers.

It has been demonstrated that the controlled adjustment of organic electrodes is a powerful tool to investigate organic solar cells. Typical OSC's utilizing commercial PEDOT can be improved by increasing the work function (doping level) of PEDOT. The fact that a zero-built-in-field OSC is realized when the work function of the PEDOT equals the reduction potential of PCBM demonstrated that the pinning of the cathode (here Al) occurs exactly at the LUMO level of the PCBM acceptor. Inverted OSC's have been realized for the first time. No pinning of the PEDOT energy levels to the PCBM LUMO level was observed unlike anticipated for the metal cathode. However, the latter is a result of the thermal evaporation process.[106b] Inverted OSC's in general have two technical shortcomings: 1) the internal barrier for extraction of photogenerated electrons reduces the short-circuit current; 2) the high series resistance of the undoped PEDOT limits the performance.

A mathematical approach is presented to separate injection from photogenerated currents in OSC's. Non-negligible injection currents were determined, which are incident intensity dependent. The typical injection current for higher V_{bi}'s could be calculated, which is due to the diode rectification.

Future work should include further polymers in order to extent the range of adjustable work functions. As shown in this thesis the work function of a C_{60}-derivative could be adjusted as well. Considering that C_{60} can be reduced six times these derivatives are interesting compounds for the cathodic range of work functions. It is possible to think of devices built "up-side down" in order to have a transparent and energetically adjustable cathodic contact.

Beside optimising the material properties, further applications will be taken into account. These energetically adjustable polymer films can be used for other electronic devices in addition to the presented OLED's and OSC's. Namely, organic lasers or organic field effect transistors (OFET) are organic devices which can most likely be improved using adjustable electrodes. Even inorganic semiconducting applications could benefit from these adjustable polymer films (hybrid devices). The low production cost combined with the simple way of processing of these polymeric materials will spark inventions for other areas of electronics (e.g. biosensors, lasers).

For OLED and OSC production the cathode *and* the anode could be adjusted to optimized energy levels in a next step. Subsequently this optimized polymeric electrodes can be laminated sandwiching the active layer. This approach has the opportunity that both interfaces and their respective energy barriers are fully controlled. Polymeric electrodes have the potential to provide the best possible electronic contact to the active material having similar specifications (e.g. flexibility).

7 Experimental Part

7.1 Substrate Preparation and Characterization

Figure 7-1 shows the general processing steps for the combinatorial devices used throughout this thesis. First, ITO covered glasses are cut into squares with an edge length of 1 inch. Glass splints and other impurities are removed carefully.
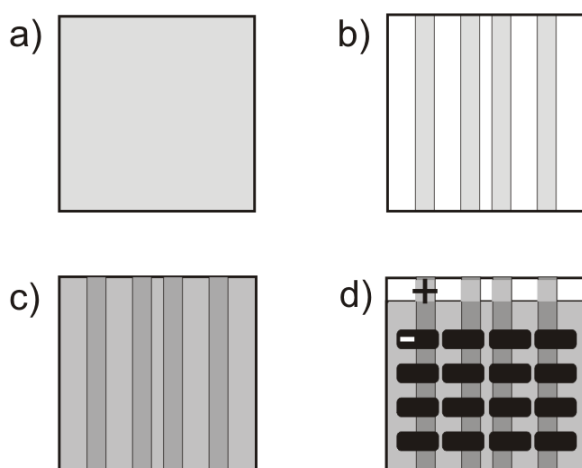
Figure 7-1: a) ITO covered glass plates are cut into pieces of an inch square; b) stripes of 2 mm are etched to form the anodic contacts; c) PEDOT is deposited and the photo-luminescent polymer is spun cast; d) 16 metal contacts are evaporated as a cathodic electrode (-) and the polymer is removed from the ITO contact positions (+).

Patterning the ITO is necessary in order to avoid short circuits, which can occur during contacting the evaporated metal. If no ITO is underneath the metal contact areas, connecting an external clamp or spring pin can generate no short circuit.

ITO can be structured by an etching process in a 5 n aqueous $FeCl_3$-solution with a small ratio of concentrated HCl. A resistant tape is used to cover the structure, which shall remain after the etching process. The surrounding ITO can be removed completely within 2 minutes if the solution has a temperature of about 60°C. Thereafter, the substrate is rinsed with water and the tape is removed. Remaining glue is removed in a soapy solution (3% of "Mucasol" in water) at a temperature of 70°C in an ultrasonic bath for 10-15 minutes. At last the substrates are rinsed with clean distilled water and dried with a stream of clean air. In Figure 7-1b) the finished ITO-pattern for a combinatorial device is shown.

As indicated in Figure 7-1d) the four devices on a single stripe have different distances to the anodic spring pin, which contacts the ITO at the upper end of the stripe. Therefore, certain resistances have to be considered depending on the device position. In order to measure the resistances 200 nm Al were evaporated directly onto the ITO-stripes according to the positions determined in Figure 7-1d). Figure 7-2 shows IV-curves, which were taken for the four

device positions on a single stripe. Device resistances R_{device} of 33, 44, 54 and 65 $\mathbb{W}$ can be calculated from the respective linear regressions. These resistances can be used to correct the applied voltage U_{SMU} for the device positions:

$$U_{cor} = U_{SMU} - R_{device} I_{SMU} \qquad \text{(7-1)}$$
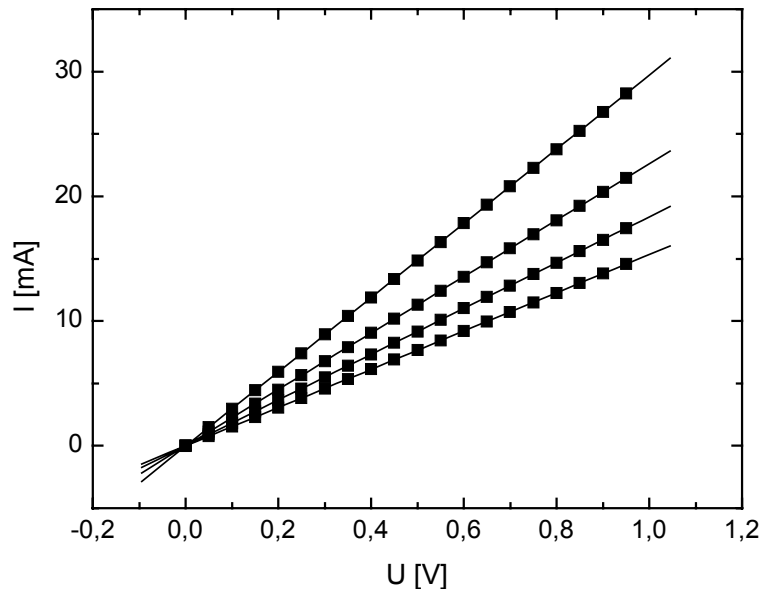
Figure 7-2: Combinatorial substrates have different ITO resistances depending on the distance of the device from the anodic contact. The resistances of 33, 44, 54 and 65 $\mathbb{W}$ have to be considered.

After etching and cleaning of the ITO substrates PEDOT is deposited either by spin casting the appropriate PEDOT solution or by electrochemical polymerisation from the monomer EDOT (chapter 7.2.1). This PEDOT layer is adjusted electrochemically and characterized by Kelvin probe, AFM and EFM measurements.

Thereafter the electroluminescent/photosensitive polymer is spun cast on top (Figure 7-1c) followed by evaporation of metal electrodes (Figure 7-1d). Where the anodic ITO contact pins will contact the ITO-stripes, the polymer is scratched away uncovering the ITO. Then every single OLED/OSC can be contacted via the respective ITO stripe (+) and the corresponding metal electrode (-). The metal is contacted beside the ITO stripe in order to avoid short circuits.

7.2 Preparation and Characterization of the Polymeric Anode

7.2.1 Electrochemical PEDOT Deposition and Adjustment

Simultaneous cyclic voltammetry and piezoelectric microgravimetry experiments were carried out with a EG&G PARC283 potentiostat and the electrochemical quartz crystal microbalance, EQCM 5710, of the Institute of Physical Chemistry (Warsaw, Poland). The 14 mm diameter, plano-convex quartz crystals with a resonant frequency of 5 MHz were purchased from Omig S. A. (Warsaw, Poland). A 100 nm thick gold film, which was vacuum deposited over 10 nm Cr underlayer onto the quartz crystal, was used as the working electrode.

For the utilization in the devices the PEDOT films were deposited onto ITO-coated substrates (Figure 7-3) by potentiostatic electropolymerization of the monomer EDOT (Bayer corporation), at 1 V in water containing sodium poly(styrene sulfonate) (NaPSS, Aldrich, MW = 70,000 g/mole) as the supporting electrolyte. For these electrochemical measurements at ITO-stripes the potentiostat with the model number 263A produced by EG&G was used. We used combinatorial substrates structured with four stripes of ITO (chapter 4.2.4) and contacted each stripe outside the solution.
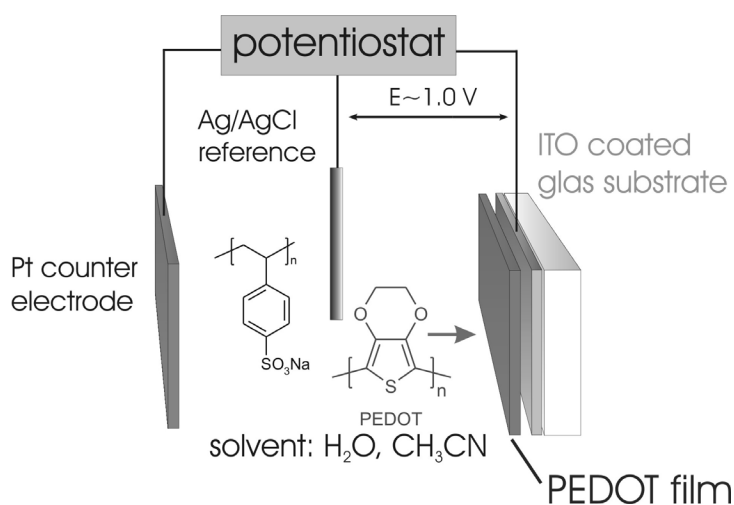
Figure 7-3: PEDOT deposition in a 3-electrode electrochemical cell.

The thickness of the PEDOT layer was adjusted to about 100 nm. The film thickness was measured with the profilometer Dektak[3] from Veeco. For this measurement the polymer film is scratched with a scalpel at different positions. Then the resulting scratches are sampled mechanically with a thin tip scanning laterally perpendicular to the direction of the scratch. By determining the height difference between the substrate, i.e. the bottom of the scratch, and the surrounding film the film thickness can be calculated. Note that ITO cannot be removed by simply scratching the surface. Thus the bottom of the scratch corresponds exactly to zero film height. It has to be ensured that the load on the tip does not cause penetration into the film.

After preparation the substrates were dried at 80°C in vacuum and then transferred into nitrogen atmosphere. The doping level of the PEDOT films was adjusted electrochemically to different values in a monomer-free nitromethane/NaPSS solution. This doping process is stabilized by penetrating counter ions, which can balance the charge caused by doping (oxidation) or dedoping (reduction) of the PEDOT polymer.

Thereafter, the films were carefully dried with a flux of nitrogen. The electrochemical equilibrium potential E_{eq} was determined. The potential scale was calibrated using the ferrocene/ferrocenium redox couple (see chapter 7.5 for details).[26]

7.2.2 Electrochemical C_{60}-Pd Polymer Deposition and Adjustment

Fullerene, C_{60}, used for polymerisation was from Fluka (Buchs, Switzerland), $[Pd^{II}(CH_3COO)_2]_3$ was from Alfa Aesar (Karlsruhe, Germany). The supporting electrolyte salt, tetra(n-butyl)ammonium hexafluorophosphate, $(TBA)PF_6$, and solvents, i.e., toluene and acetonitrile, were from Fluka (Buchs, Switzerland).

The same experimental setup as in the previous chapter was used to polymerize a redox active C_{60}-Pd polymer.[103] 0.3 mMol C_{60} was mixed with 1.8 mMol $[Pd(CuCOO)_2]_3$ and 0.1 Mol $(TBA)PF_6$ in acetonitrile/toluene (1:4, v:v). The C_{60}/Pd film was prepared under cyclic voltammetry conditions. The cell was covered with Argon and the solution was purged for several minutes in order to get rid of oxygen. The ITO electrode with the deposited C_{60}/Pd film was removed from the solution for electropolymerization, rinsed with acetonitrile. The film was mechanically stable in air and fairly smooth. The molecular weight M_w of the resulting polymer cannot be determined easily since the film cannot be dissolved from the substrate. [103]

The final film was adjusted in 0.1 M $(TBA)PF_6$ in acetonitrile/toluene (1:4, v:v) to the desired potential.

7.2.3 UV/Vis Measurements

For the UV/Vis measurements the spectrometer Cary 50 produced by Varian was used. Fibre optics allowed measurements under inert gas conditions inside a glovebox. The Cary 50 Spectrophotometer incorporates a Xenon flash tube with a maximum scan rate of 24,000 nm per minute which means that the whole wavelength range of 190 – 1100 nm can be scanned in 3 seconds. Photosensitive samples are not exposed to continuous light as the Xenon lamp flashes only when acquiring a data point.

7.2.4   Kelvin Probe and EFM Measurements

Kelvin probe measurements (Figure 3-4) were used to determine changes of the work function ϕ_W. We designed a Kelvin probe setup based on the core from Besocke DELTA PHI GmbH. Hereby, the contact potential difference (*CPD*) between a vibrating (170 Hz) gold grid (reference) and the PEDOT-films (material of interest) is measured. A lockin amplifier compensates the *CPD* nulling the current, which is produced by the vibrating plate distance of the capacitor. Due to the fact that the work function of the gold grid (reference) is ill defined, only relative data can be obtained. It was confirmed that the work function of the reference did not change with time.

Figure 7-4 shows the *CPD* signal for four stripes on a single substrate. The first stripe is highly doped and the following stripes form a sequence down to the nearly neutral last film. It is discernable that equilibrium has to be reached before the respective value can be collected. The time frame for this equilibration ranges from 3 to 15 minutes. The peaks indicate the change from the current stripe to the next one. After every change the equilibrium has to be reached again. For every *CPD* measurement in this thesis we waited until the saturation was reached.
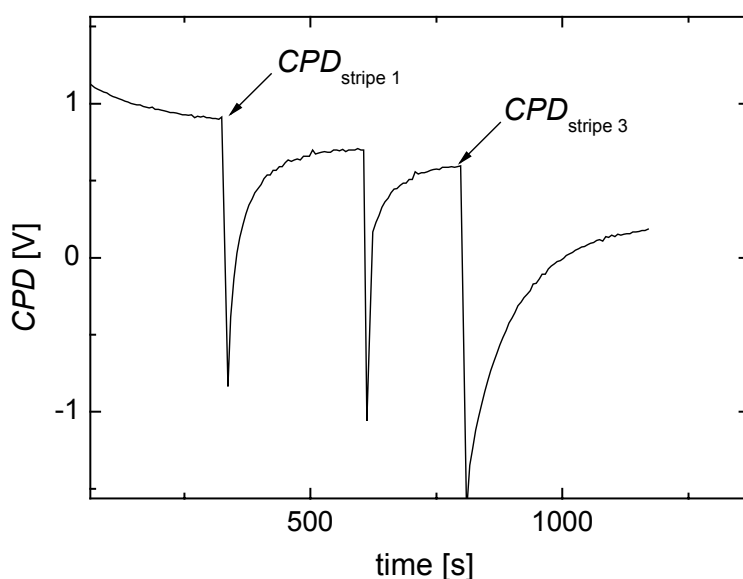
Figure 7-4: CPD-measurement on a single substrate with four differently adjusted PEDOT-stripes. The peaks in-between the measurements indicate the change of the stripe.

An electrostatic force microscope (EFM; Multimode Nanoscope IIIa, Digital Instruments) was used to obtain the lateral distribution of the *CPD* across the PEDOT surfaces. Magnetic force etched silicon tips (MESP) were used as reference probe for all EFM measurements. The charged PEDOT stripes were investigated in the area between the as grown and the adjusted PEDOT area. In order to get accurate potential images the stripe was connected to the feedback circuit with conductive silver paint.

The measurements were performed in inert gas atmosphere under conditions identical to the preparation process of solution-based OLED's.

7.3 Device Preparation

7.3.1 Spin Coating of the Electroluminescent Polymer

Thin polymer films were produced by a technique called spin coating. In this thesis the spin coaters from Convac (model 1001) and SCS (model P6204) were used. First a solution of the desired polymer is produced. Thereafter the substrate is sucked on the spin chuck of the spin coater by vacuum. Then the solution is dropped onto the substrate and the spin coating process is started. The spin speed can be adjusted between 250 and 8000 rpm. During the rotation most of the solution is hurled away. The remaining solvent is forming a smooth and homogeneous thin film, which dries slowly within about 20 s.

For the OLED's MDMO-PPV was spin coated on top of the PEDOT/ITO-coated glass substrates. MDMO-PPV can be dissolved in several solvents. The resulting films after spin coating depend on the MDMO-PPV concentration the spin speed and the solvent itself. Figure 7-5 shows the correlation between the spin speed and the resulting film thickness for two MDMO-PPV solutions and one MDMO-PPV:PCBM blend. The concentration of 5 mg/ml was identical for both MDMO-PPV solutions, but the solvent was on the one hand chlorobenzene (squares) and on the other hand toluene (circles). Obviously, the average thickness of the resulting layers differs for the same spin speed. It is also known that the morphology is different for different solvents.[80]
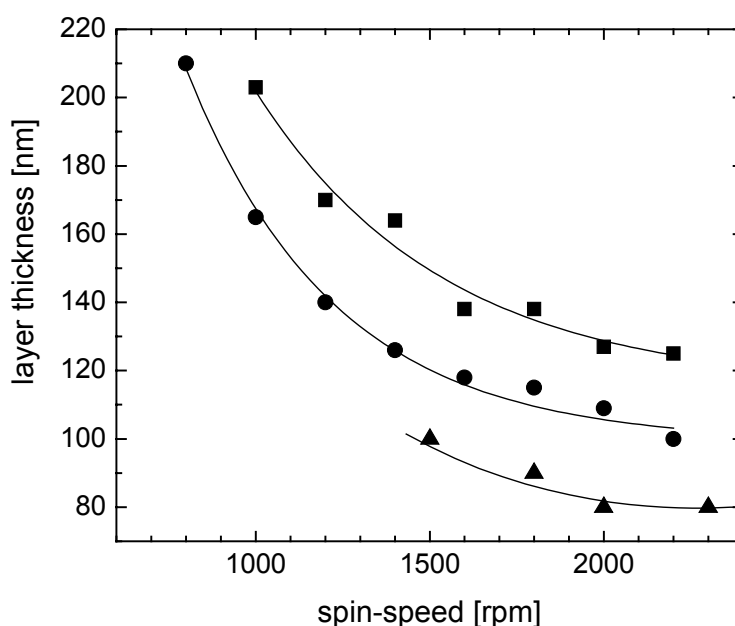
Figure 7-5: Correlation between spin coating speed and the resulting polymer film thickness. Squares: 5 mg/ml in chlorobenzene; Circles: 5 mg/ml in toluene; Triangles: MDMO-PPV:PCBM (1:4) 12.5 mg/ml in chlorobenzene.

For the devices in this thesis we spin coated from a toluene solution (5mg/ml, 2200 rpm), resulting in films of about 100 nm thickness. Since PEDOT is insoluble after film formation, the solution could not dissolve the underlying PEDOT layer. For the OSC a solution of MDMO-PPV and PCBM (1:4 by weight) in chlorobenzene[80] was spin coated at 1500 rpm, resulting in films of about 100 nm thickness (triangles).

7.3.2   Evaporation of the Cathodic Metal Contacts

Finally, four metal stripe electrodes with a thickness of 200 nm were evaporated perpendicularly to the ITO stripes (Figure 7-1d), yielding 16 individually addressable devices each with an active area of 6.3 mm^2.

The evaporation of the cathodic contact was carried out with an evaporation chamber from Leybold. The used metals from Balzers had a purity of more than 99.95%. The spincoated substrates were mounted into a structured shadow mask. This mask was fixed in the chamber in a distance of 30 cm from the evaporation source. The mask holder enables to adjust the temperature of the mounted substrates by controlled heating cartridges and cooling water. The metals are evaporated from electrically heated sources at a pressure lower than $5 \cdot 10^{-6}$ mbar. For Ca the source containers are made from molybdenum, whereas for Al, Ag or Au they are made from tungsten. Before the evaporation process is started the substrates are annealed for one hour at a temperature of 80°C in vacuum. During this time the film gets rid of remaining solvents. Thereafter the substrates are cooled down to 6°C. The deposition rate is monitored by a piezo element, which calculates the increased thickness by the change of its normal frequency (compare microbalance measurements). This thickness detector is mounted close to the substrates. In general the metal films are deposited with a constant rate of 1 nm/s. In case of Au using very low rates of 0.1-0.2 nm/s can minimize the diffusion of atoms into the polymer film. For low work function metals (e.g. Ca) the thickness is kept below 40 nm covered by a protecting layer of Al or Ag. The total metal layer thickness is always 200 nm.

7.4   **Device Characterization**

7.4.1   Current-Voltage-Brightness Setup

All devices were characterized in nitrogen atmosphere in electrically shielded measurement boxes. Figure 7-6 shows a sketch of the experimental setup for the combinatorial devices.

The 16 metal contacts and the four ITO-stripes were contacted with spring pins, which are covered with indium. Indium is sufficiently soft and produces best contact interfaces between the tip and the respective electrode on the substrate. The ITO stripe for the current device under test was chosen by a

computer-controlled distributor in order to avoid cross talk between adjoining devices.
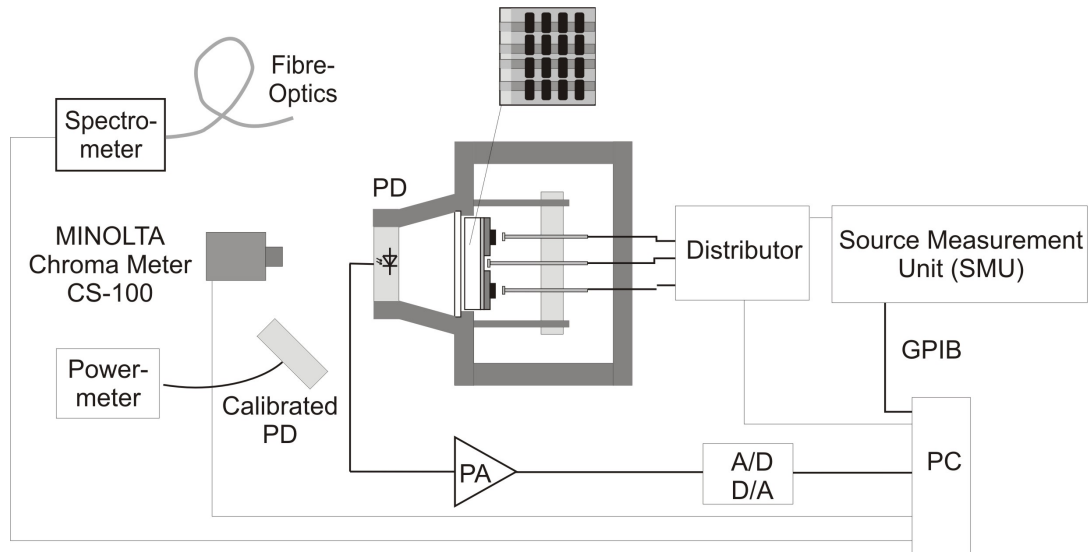

Figure 7-6: Sketch of the used setup for I-V-EL-measurements.

In order to characterize the OLED's and OSC's I-V-curves were measured using a computer controlled (via GPIB) source measurement unit (SMU238 from Keithley). Since the SMU has just one input the desired device out of 16 possible devices was chosen by another computer controlled distributor. The EL brightness of the OLED's was measured with an inorganic photodiode (PD). The produced photovoltage was pre-amplified and translated by an AD-converter, which is part of a DAQ-card (PC-1200 from National Instruments) in the computer. This brightness signal was calibrated with the chromameter CS100 (Minolta) or with a powermeter.
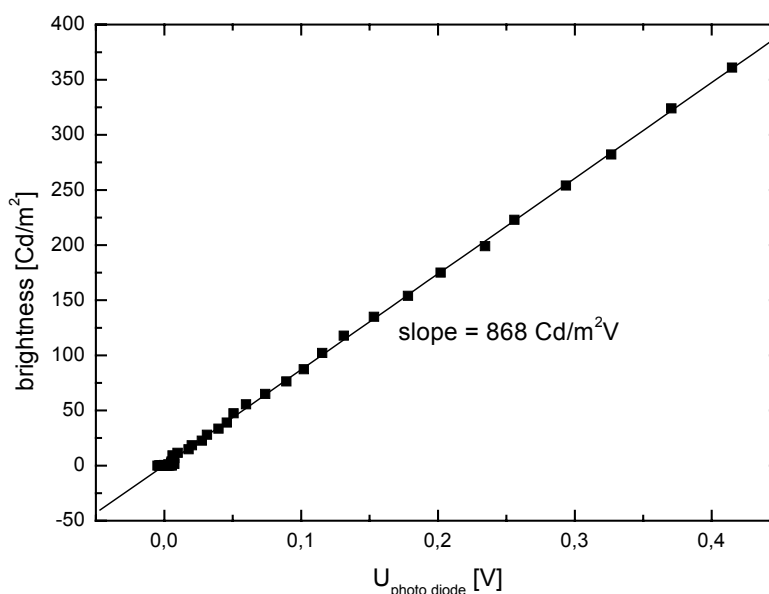

Figure 7-7: Calibration of the inorganic photodiode for MDMO-PPV

The reason for the use of an inorganic photodiode rather than the chromameter is the speed of measurements. Although we managed to read and decode the data supported from the chromameter by the computer the measurements with this instrument are comparatively slow since a certain time is needed for the integration period. For the calibration a single OLED was successively measured with the PD, with the chromameter and with the PD again. It was ensured that the PD measurements produced identical results in order to avoid that aging or degradation effects influence the calibration. The brightness determined by the chromameter at a certain voltage applied to the device was plotted against the voltage of the photodiode (Figure 7-7) at the same device voltage. The slope of the linear regression then gives the calibration. According to Figure 7-7 this slope amounts to 868 Cd/m^2 per 1 V pre-amplified photovoltage delivered from the used PD. Note, however, that this calibration has to be repeated if another EL spectrum from another electroluminescent polymer is under test.

7.4.2   Photovoltaic Setup

The combinatorial devices, which consist of 4 different adjusted PEDOT stripes and four devices per stripe, were illuminated from the ITO-side by a 532 nm laser beam in nitrogen atmosphere. The laser driver allowed controlling the current, but the power output was not defined properly. Therefore, the output was calibrated with a power meter (Figure 7-8).
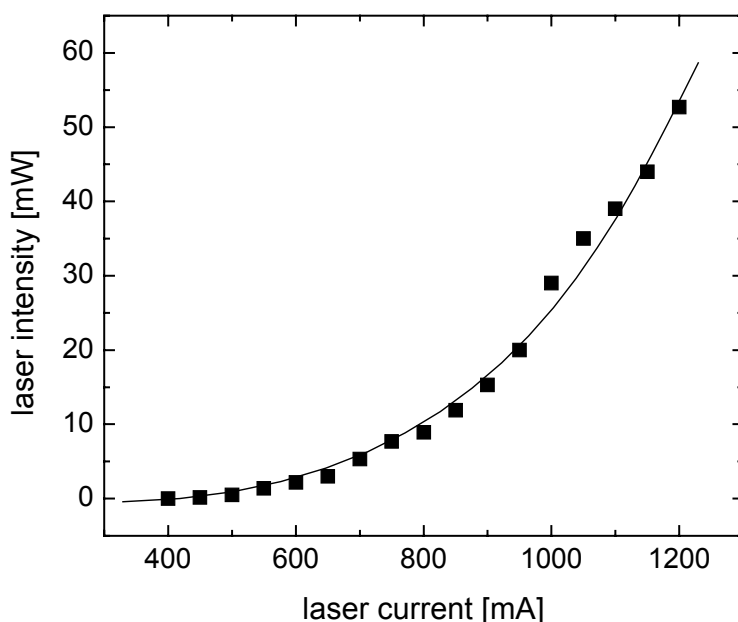
Figure 7-8: Power calibration of the laser with a power meter.
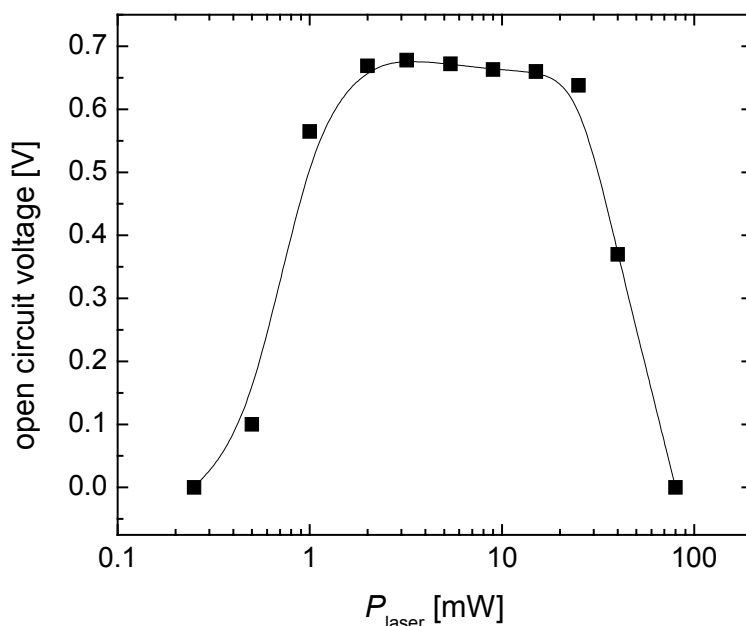
Figure 7-9: Open circuit voltage of a bulk-heterojunction OSC in dependence on the incident laser power. For sufficient intensities the photogenerated charges cause the saturation open circuit voltage. For the highest intensities the device is photochemically destroyed.

I-V-curves were recorded in the electrically shielded measurement boxes during illumination using a source measurement unit (SMU238 from Keithley). From these curves the voltage V_{oc} at which the current is zero is determined (flat band condition). Since V_{oc} increases with increasing light intensity and since V_{oc} reaches a saturation after passing a certain intensity, we ensured for each device under test that the intensity of the laser was large enough to be in the intensity-independent regime, but without photochemically destroying the devices (Figure 7-9).

7.4.3   Spectral Response Setup

For the photoaction spectra measurements a Solux quartz halogen lamp (10° beam spread) was used, which, when placed at 300 mm from the device, delivers a power density of 60 mW/cm^2. The intensity of the light incident upon the photocells was measured using a Pin 10D photodiode calibrated using a Photodyne 150 detector. Measurements of the spectral response were made by illuminating the diodes with light passed through an automatically tuneable Oriel 8098 monochromator. The corresponding voltages across the device were observed across a 65.4 MΩ load.

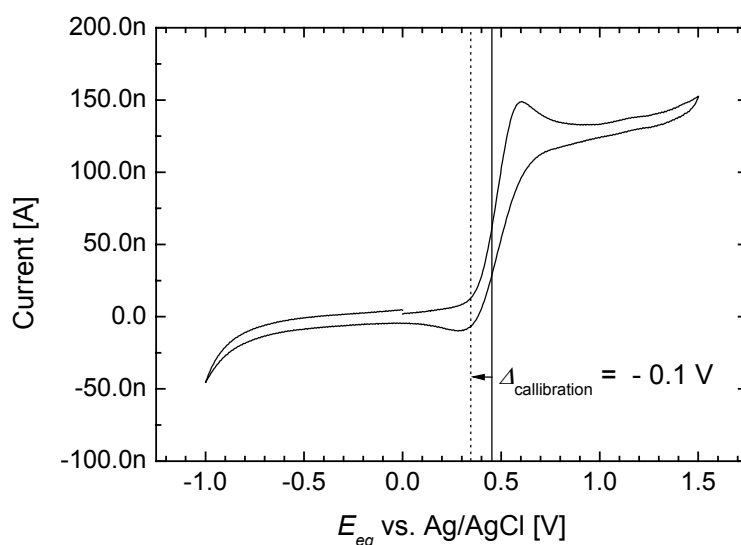## 7.5 Cyclic Voltammetry

Cyclic voltammetry was carried out at room temperature in a three-electrode cell, which contained methylene chloride and tetrabutylammonium hexafluoro-phosphate (TBAPF$_6$, 0.1 M) as supporting electrolyte. Figure 7-10 shows the electrochemical setup. The computer controls a function generator. The generated function is amplified by the potentiostat, which is connected to the

cell. The potential is measured current free between the reference (RE) and the working electrode (WE), whereas the current is measured between the working and counter electrode (CE).
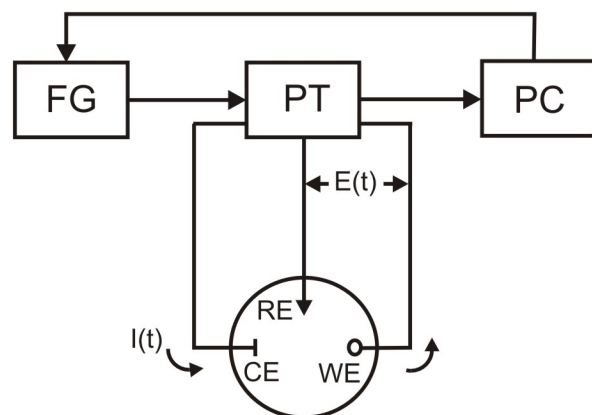
Figure 7-10: Three electrode electrochemical setup: A computer (PC) controls the function generator (FG). The signal is amplified by the potentiostat (PT), which is connected to the cell. The potentiostat measures the current and transmits the result back to the PC.[122]

The potential scale for every electrochemical measurement presented in this thesis was calibrated using the ferrocene/ferrocenium redox couple (0.35 vs. Ag/AgCl).[26] Due to infinitesimal impurities in the electrochemical cell the electrochemical potential can be changed to slightly shifted values. In order to control this effect standard systems have been introduced for the calibration of the scale. For this thesis a silver wire covered with AgCl was used as the electrochemical reference. The reference of such an electrode is assumed to be stable for the acquisition duration of a common cyclic voltammogram, but it can change on a longer time scale.

Figure 7-11: Example for a ferrocene calibration (here: cyclic voltammogram in methylene chloride with $TBAPF_6$ (0.1 M), v = 100 mV/s, work electrode: platinum). The measured oxidation peak at 0.45 V (vertical solid line) is expected to occur at 0.35 V. Therefore, the whole scale has to be shifted left by 0.1 V.

Therefore, our measurements have been calibrated by subsequently measured cyclic voltammograms of ferrocene. Due to its sandwich structure ferrocene is fairly independent of ambiguous conditions having its first oxidation peak at +0.35 V vs. Ag/AgCl.[26] Figure 7-11 shows exemplarily a certain ferrocene calibration. The measured centre between forth and back peak (oxidation and re-reduction) occurs at 0.45 V (vertical solid line) is expected to occur at 0.35 V (vertical dotted line). Thus the whole scale has to be shifted left by 0.1 V. The shape of this curve deviates slightly from typical measurements for which a peak separation of 59 mV can be observed and for which the hysteresis is more pronounced. This difference is most likely due to an ITO work electrode (stripe on a glass slide) instead of a for example (standard) platinum electrode.

8 References

1   C. K. Chiang, C. R. Fincher, Y. W. Park, A. J. Heeger, H. Shirakawa, E. J. Louis, S. C. Gau, A. G. MacDiarmid, *Phys. Rev. Lett.*, **39** 1098 (1977).
2   H. Shirakawa "Synthesis of Polyacetylene", in *Handbook of Conducting Polymers*, 2nd Edition (T. A. Skotheim, R. L. Elsenbauer, J. R. Reynolds editors), Marcel Dekker, New York (1998).
3   W. Helfrich, W. G. Schneider, Phys. Rev. Lett. 14, 229-231 (1965).
4   M. Pope, H. P: Kallmann, P. Magnante, *J. Chem. Phys.* **38**, 2042-2043 (1963).
5   C. W. Tang, S. A. Van Slyke, *Appl. Phys. Lett.* **51**, 913-915 (1987).
6   G. A. Sotzing, S. M. Briglin, R. H. Grubbs, N. S. Lewis, *Analytical Chemistry*, **72**, 3181 (2000).
7   F. Garnier, R. Hajlaoui, A. Yassar, P. Srivastava, *Science* **265**, 1684-1686 (1994).
8   P. Ostoja, S. Guerri, S. Rossini, M. Servidori, C. Taliani, R. Zamboni, *Synth. Met.* **54**, 447-452 (1993).
9   L. Torsi, A. Dodabalapur, L. J. Rothberg, A. W. P. Fung, H. E. Katz, *Science* **272**, 1462-1464 (1996).
10 Y. Yang, A. J. Heeger, *Nature* **372**, 344-346 (1994).
11 R. Brown, A. Pomp, C. M. Hart, D. M. Deleeuw, *Science* **270**, 972-974 (1995).
12 H. Sirringhaus, N. Tessler, R. H. Friend, *Science* **280**, 1741-1744 (1998).
13 G. Yu, J. Gao, J. C. Hummelen, F. Wudl, A. J. Heeger, *Science* **270**, 1789-1791 (1995).
14 M. Granström, K. Petritsch, A. C. Arias, A. Lux, M. R. Andersson, R. H. Friend, *Nature* **395**, 257-260 (1998).
15 J. H. Burroughes, D. D. C. Bradley, A. R. Brown, R. N. Marks, K. Nackay, R. H. Friend, P. L. Burns, A. B. Holmes, *Nature* **347**, 539-541(1990).
16 P. L. Burn, *Nature* **356**, 47-49 (1992).
17 N. C. Greenham, S. C. Moratti, D. D. C. Bradley, R. H. Friend, A. B. Holmes, *Nature* **365**, 628-630 (1993).
18 D. Braun, A. J. Heeger, *Appl. Phys. Lett.* **58**, 1982-1984 (1991).
19 G. Gustafsson, Y. Cao, G. M. Treacy, F. Klavetter, N. Colaneri, A. J. Heeger, *Nature* **357,** 477-479 (1992).
20 F. Hide, M. A. DiazGarcia, B. J. Schwartz, M. R. Andersson, Q. B. Pei, A. J. Heeger, *Science* **273,** 1833–1836 (1996).
21 F. Hide, B. J. Schwartz, M. A. Diaz-Garcia, A. J. Heeger, *Chem. Phys. Lett.* **256**, 424– 430 (1996).
22 N. Tessler, D. J. Denton, R. H. Friend, *Nature* **382,** 695–697 (1996).
23 J. Bharathan, Y. Yang, *Appl. Phys. Lett.* **72**, 2660-2662 (1998).
24 N. Tessler, P. K. H. Ho, V. Cleave, D. J. Pinner, R.H. Friend, G. Yahioglu, P. Le Barny, J. Gray, M. de Souza, G Rumbles, *Thin Solid Films* **363**, 64-67 (2000).
25 Skotheim, T. A. Handbook of Conducting Polymers (Dekker, New York, 1986).
26 J. Bard, L. R. Faulkner, *Electrochemical Methods – Fundamentals And Applications*, Wiley (1980).

27 K. Z. Xing, M. Fahlman, X. W. Chen, O. Inganäs, W. R. Salaneck, *Synth. Met.* **89**, 161-165 (1997).

28 T. M. Brown, J. S. Kim, R. H. Friend, F. Cacialli, R. Daik, W. J. Feast, *Appl. Phys. Lett.* **75**, 1679-1681 (1999).

29 Dissertation: Markus Groß, University of Munich, 2002

30 H. Bässler, *Phys. Stat. Sol. (b),* **107**, 9 (1981).

31 H. Bässler, *Phys. Stat. Sol. (b),* **175**, 15 (1993).

32 P. Gommes da Costa, E. M. Conwell, *Phys. Rev. B.*, **48** (1993).

33 D. Beljonne, Z. Shuai, R. H. Friend and J. L. Brédas, *J. Chem. Phys.*, **102,** 2042 (1995).

34 H. Bäßler, G. Schonherr, M. Abkowitz, D. M. Pai, *Phys. Rev. B* **26,** 3105-3113 (1982).

35 H. Ishii, K. Sugiyama, E. Ito, K. Seki, *Adv. Mat.* **11**, 605-625 (1999).

36 R. A. Strayer, W. Mackie, L. W. Swanson, *Surf. Sci.* **34**, 225 (1973).

37 J. Hoelzel, F. K. Schulte, H. Wagner, *Solid State Surface Physics*, Springer, Berlin (1979).

38 L. J. Brillson, *Surf. Sci. Rep.* **2**, 123 (1982).

39 W. Erley, H. Ibach, *Surf. Sci.* **178**, 565 (1986).

40 K. Seki, H. Yanagi, Y. Kobayashi, T. Ohta, *Phys. Rev. B* **49**, 2760 (1994).

41 G. Gensterblum, K. Hevesi, B.-Y. Han, L.-M. Yu, J.-J. Pireaux, P. A. Thiry, R. Caudano, A.-A. Lucas, D. Bernaerts, S. Amelinckx, G. Van Tendeloo, G. Bendele, T. Buslaps, R. L. Johnson, M. Foss, R. Feidenhansl, G. Le Lay, *Phys. Rev. B* **50**, 11 981 (1994).

42   C. Gerthsen, H.O. Kneser, H. Vogel, *Physik*, 756-760 (1989).

43 Y. Park,V. Choong, E. Ettedgui,Y. Gao,B. R. Hsieh, T.Wehrmeister, K. Muellen, *Appl. Phys. Lett.* **69**, 1080 (1996).

44 S. M. Sze, *Physics of Semiconductor Devices*, 2nd ed.,Wiley, New York (1981).

45 W. Mönch, *Surf. Sci.* **299/300**, 928 (1994).

46 L. J. Brillson, *Surf. Sci.* **299/300**, 909 (1994).

47 W. R. Salaneck, M. Logdlund, Polymers for Adv. Technologies **9**, 419-428 (1998)

48 J. D. Wright, *Molecular Crystals*, Cambridge University Press, Cambridge (1987).

49 Y. Maruyama, H. Inokuchi, *Bull. Chem. Soc. Jpn.* **39**, 1418 (1966).

50 M. Martin, J. J. Andre, J. Simon, *J. Appl. Phys.* **54**, 2792 (1983).

51 W. R. Salaneck, S. Stafström, J. L. Brédas, *Conjugated Polymer Surfaces and Interfaces: Electronic and Chemical Structure of Interfaces for Polymer Light Emitting Devices*, *Cambridge University Press*, Cambridge (1996).

52 V.-E. Choong, M. G. Mason, C. W. Tang, Y. Gao, *Appl. Phys. Lett.* **72**, 2689 (1998).

53 K. Konstadinidis, F. Papadimitrakopoulos, M. Galvin, R. L. Opila, *Appl. Phys.* **77**, 5642 (1995).

54 K. Xing, M. Fahlman, J.Löglund, D. A. dos Santos, P. V. R. Lazzaroni, J.-L. Brédas, R. W. Gymer,W. R. Salaneck, *Adv. Mater.* **8**, 971 (1996).

55 Y. Gao, in *Polymer-Solid Interfaces: from Model to Real Systems* (Eds: J. D. J. J. Pireaux, P. Rudolf), *Press Universitaires de Namur*, Namur, 365 (1998).

56 V. E. Choong, Y. Park, B. R. Hsieh, Y. Gao, *in Electrical and Optical Polymer Systems: Fundamentals, Methods, and Applications* (Eds: D. L. Wise, G. Wnek, D. J. Trantolo, T. M. Cooper), Marcel Dekker, New York, in press.

57 M. Löglund, P. Dannetun, W. Salaneck, *in Handbook of Conducting Polymers* (Eds: T. Skotheim, R. L. Elsenbaumer, J. R. Reynolds), Marcel Dekker, New York, pp. 667-694 (1997).

58 A. J. Heeger, S. Kivelson, J. R. Schrieffer, W.-P. Su, *Rev. Mod. Phys.* **60**, 781 (1988).

59 MultiMode™ SPM Instruction Manual, digital instruments

60 X. Maldague, *Nondestructive evaluation of materials by infrared thermograph*y, London, Springer-Verlag, 224 p., 1993 (new revised edition, *John Wiley & Sons* Pub., exp. in 2001).

61 X. Maldague ed., *Infrared Methodology and Technolog*y, *Gordon and Breac*h, NY, 525- (1994).

62 Kaplan H., *Practical applications of infrared thermal sensing and imaging equipment, SPIE vol. TT* **13**, 137- (1993).

63 J. R. Sheats, H. Antoniadis, M. Hueschen, W. Leonard, J. Miller, R. Moon, D. Roitman, A. Stocking, *Science* **273,** 884-888 (1996).

64 R. Lazzaroni, M. Lögdlund, S. Stafström, W. R. Salaneck, D. D. C. Bradley, R. H. Friend, N. Sato, E. Orti, J. L. Brédas 1990 *Conjugated Polymeric Materials: Opportunities in Electronics, Optoelectronics, and Molecular Electronics* ed J. L. Brédas and R. R. Chance (Dordrecht: Kluwer)

65 G. Yu, C. Zhang, A. J. Heeger, *Appl. Phys. Lett.* **64**, 1540 (1994).

66 H. Antoniadis, B. R. Hsieh, M. A. Abkowitz, M. Stolka, S. A. Jenekhe, *Polym Prepr.* **34**, 490 (1993).

67 S. Karg, W. Riess, V. Dyakonov, M. Schwoerer, *Synth. Met.* **54**, 427 (1993).

68 R. H. Friend, R. W. Gymer, A. B. Holmes, J. H. Burroughes, R. N. Marks, C. Taliani, D. D. C. Bradley, D. A. Dos Santos, J. L. Bredas, M. Logdlund, W. R. Salaneck, *Nature* **397**, 121-128 (1999).

69 A. J. Heeger, *Solid State Commun.* **107**, 673-679 (1998).

70 H. Spreizer, H. Becker, E. Kluge, W. Kreuder, H. Schenk, R. Demandt, H. Schoo, *Adv. Mater.* **10**, 1340-1344 (1998).

71 D. A. Pardo, G. E. Jabbour, N. Peyghambarian, *Adv. Mater.* **12**, 1249– 1252 (2000).

72 J. Birnstock et al., *Appl. Phys. Lett.* **78**, 3905-3907 (2001).

73 E. Haskal et al., *SID Digest Tech. Pap.* **33**, 776–779 (2002).

74 C. David Müller, Aurélie Falcou, Nina Reckefuss, Markus Rojahn, Valèrie Wiederhirn, Paula Rudati, Holger Frohne, Oskar Nuyken, Heinrich Becker, Klaus Meerholz, *Nature* **421**, 829-833 (2003).

75 P. W. M. Blom, M.C.J.M. Vissenberg, *Mat. Sci. Engin.*, *27*, 53-94 (2000).

76 M. Deußen, H. Bässler, *Chem. i. u. Z.* **31,** 76 (1997).

77 F. Garten, J. Vrijmoeth, A. R. Schlatmann, R. E. Klapwijk, G. Hadziioannou, *Synth. Met.* **76**, 85 (1996).

78 P. E. Burrows, C. Bulovic, S. T. Forrest. L. S. Sapochak, D. M. McCarty, M. E. Thompson, *Appl. Phys. Lett.* **65**, 2922 (1994).

79 C. J. Brabec, N. S. Sariciftci, J. C. Hummelen, *Adv. Funct. Mater.* **11**, 15- 26 (2001).

80 S. E. Shaheen C. J. Brabec, N. S. Sariciftci, F. Padinger, T. Fromherz, J. C. Hummelen, *Appl. Phys. Lett.* **78**, 841 (2001).

81 G. Yu, K. Pakbaz, A. J. Heeger, *Appl. Phys. Lett.* **64**, 3422 (1994).

82 H. Antoniadis, B. R. Hsieh, M. A. Abkowitz, S. A. Jenekhe, M. Stolka, *Synth. Meth.* **62**, 265 (1994).

83 Yoshino, K.; Tada, K.; Fujii, A.; Conwell, E. M.; Zakhidov, *A. A. IEEE Trans. Electron Devices* **44**, 1315–1324 (1997).

84 W. Rieß, S. Karg, V. Dyakonov, M. Meier, M. Schwoerer, *J. Lumin.* **60-61**, 906 (1994).

85 N. S. Saricifci, D. Braun, C. Zhang, V. Srdanov, A. J. Heeger, G. Stucky, F. Wudl, *Appl. Phys. Lett.* **62**, 585 (1993).

86 J. J. M. Halls, C. A. Walsh, N. C. Greenham, E. A. Marseglia, R. H. Friend, S. C. Moratti, A. B. Holmes, *Nature* **376**, 498 (1995).

87 N. S. Sariciftci, A. J. Heeger, *Int. J. Mod. Phys. B* **8**, 237 (1994).

88 X. Wei, Z. V. Vardeny, N. S. Sariciftci, A. J. Heeger, *Phys. Rev. B* **53**, 2187 (1996).

89 S. Morita, A. A. Zakhidov, K. Yoshino, *Solid State Commun.* **82**, 249 (1992).

90 K. Yoshino, X. H. Yin, S. Morita, T. Kawai, A. A. Zakhidov, *Solid State Commun.* **85**, 85 (1993).

91 K. Yoshino, T. Akashi, K. Yoshimoto, S. Morita, R. Sugimoto, A. A. Zakhidov, *Solid State Commun.* **90**, 41 (1994).

92 J. Salbeck, *Ber. Bunsenges. Phys. Chem.* **100**, 1667-1677 (1996).

93 Y. Cao, G. Yu, C. Zhang, R. Menon, A. J. Heeger, *Synth. Met.* **87**, 171-174 (1997).

94 G. G. Malliaras, J. R. Salem, P. J. Brock, C. Scott, *Phys. Rev. B* **58**, R13411-R13414 (1998).

95 M. Dietrich, *Dissertation*, Universität Freiburg, 104 (1990).

96 M. Dietrich, J. Heinze, *Synth. Met.* **41-43,** 503-506 (1991).

97 Produktinformation *Baytron P*, Bayer AG (1997).

98 K. Meerholz, J. Swiatkiewicz, P. N. Prasad, *J. Phys. Chem.* **99,** 7715-7722 (1995).

99 M. Gross, D. C. Müller, H.-G. Nothofer, U. Scherf, D. Neher, C. Bräuchle, K. Meerholz, *Nature* **405**, 661-665 (2000).

100 G. Li, M. Josowicz, J. Janata, *Synth. Met.* **125**, 273-278 (2001).

101 R. O. Loufty, C. K. Hsiao, B. S. Ong, B. Keoshkerian, *Can. J. Chem.* **62**, 1877-1885 (1984).

102 L. L. Miller, G. D. Nordblom, E. A. Mayeda, *J. Org. Chem.* **37**, 916-919 (1972).

103 K. Winkler, K. Noworyta, W. Kutner, A. L. Balch, *J. Electrochem. Soc.* **147**, 7, 2597-2603 (2000).

104 W. K. Winkler, K. Noworyta, A. de Bettencourt-Dias, J. W. Sobczak, C.-T. Wu, L.-C. Chen, W. Kutner, A. L. Balch, *J. Mater. Chem.* **13**, 518–525 (2003).

105 W. Kutner, *Electrochim. Acta* **37**, 1109-1117 (1992).

106 a) I. H. Campbell, T. W. Hagler, D. L. Smith, *Phys. Rev. Lett.* **76**, 1900-1903 (1996); b) C. M. Heller, I. H. Campbell, D. L. Smith, N. N. Barashkov, A. P. Ferraris, *J. Appl. Phys.* **81**, 3227-3231 (1997).

107 G. G. Malliaras, J. R. Salem, P. J. Brock, J. C. Scott, *J. Appl. Phys.* **84**, 1583-1587 (1998).

108 X. Wei, M. Raikh, Z. V. Vardeny, Y. Yang, D. Moses, *Phys. Rev. B* **49**, 17 480 (1994).

109 Handbook of Chemistry and Physics, CRC Press.

110 H. Muramatsu, E. Tamia, I. Karube, *Anal. Chem.* **60**, 2142-2146 (1988).

111 Y. Shirota, Y. Kuwabara, H. Inada, T. Wakimoto, H. Nakada, Y. Yonemoto, S. Kawami, K. Imai, *Appl. Phys. Lett.* **65**, 807-809 (1994).

112 G. G. Malliaras, J. C. Scott, *J. Appl. Phys.* **85**, 7426-7432 (1999).

113 M. Wohlgenannt, K. Tandon, S. Mazumdar, S. Ramasesha, Z.V. Vardeny, *Nature* **409**, 494-497 (2001).

114 K. Meerholz, D. C. Müller, *Adv. Funct. Materials* **11**, 251-253 (2001).

115 U. Albrecht, H. Bässler, *Chem. Phys.* **199**, 207-214 (1995).

116 R. H. Fowler , L. Nordheim, *Proc. R. Soc. London Ser. A* **119**, 173-181 (1928).

117 H. Campbell, J. D. Kress, R. L. Martin, D. L. Smith, N. N. Barashkov, J. P. Ferraris, *Appl. Phys. Lett.* **71**, 3528 (1997).

118 E. A. Katz, D. Faiman, S. M. Tuladhar, J. M. Kroon, M. M. Wienk, T. Fromherz, F. Padinger, C. J. Brabec, N. S. Sariciftci, *J. Appl. Phys.* **90**, 5343-5350 (2001).

119 C. J. Brabec, A. Cravino, D. Meissner, N. S. Sariciftci, T. Fromherz, M. T. Rispens, L. Sanchez, J. C. Hummelen, *Adv. Funct. Mat.* **11**, 374-380 (2001).

120 C. J. Brabec, A. Cravino, D. Meissner, N. S. Sariciftci, M. T. Rispens, L. Sanchez, J. C. Hummelen, T. Fromherz, *Thin Solid Films* **403**, 368 (2002).

121 G. G. Malliaras, J. R. Salem, P. J. Brock, J. C. Scott, *J. Appl. Phys.* **84**, 1583 (1998).

122 J. Heinze, Angew. Chem. **96**, 823-840 (1984).

9 Appendix

9.1 <u>Abbreviations</u>

AFM	Atomic Force Microscope
CPD	Contact Potential Difference
CV	Cyclic Voltammogram
E_{eq}	Electrochemical Equilibrium Potential
$E_{eq,ox}$	Electrochemical Equilibrium Oxidation Potential
E_F	Fermi Level
EFM	Electric Force Microscope
EL	Electroluminescence
FF	Fill Factor
HOMO	Highest Occupied Molecular Orbital
I_{sc}	Short-circuit Voltage
I_e	Electron Current
I_h	Hole Current
ILC	Injection Limited Current
ITO	Indium Tin Oxide
J_e	Electron Current Density
J_h	Hole Current Density
LUMO	Lowest Unoccupied Molecular Orbital
OLED	Organic Light Emitting Diode
OSC	Organic Solar Cell
PL	Photoluminescence
SCLC	Space Charge Limited Current
UPS	Ultraviolet photon spectroscopy
V_0	Compensation Voltage
V_{bi}	Built-in Voltage
V_{oc}	Open Circuit Voltage
ε	Emissivity
ϕ_W	Work Function
$\phi_{B,e}$	Barrier Height for Electrons
$\phi_{B,h}$	Barrier Height for Holes
η_{rec}	Recombination Efficiency

9.2 Publications

9.2.1 Articles in International Journals

Holger Frohne, Christopher R. McNeill, Gordon G. Wallace, Paul C. Dastoor
Enhancement of polymer electronics via surface states on highly doped polymeric anodes
J. Phys. D. **37**, 165-170 (2004).

Holger Frohne, David C. Müller, Nina Reckefuß, Paula Rudati, Klaus Meerholz
Optimisation of Organic Semiconductor Devices by Anode Modification
SPIE proceedings **4800**, 172-181 (2003).

C. David Müller, Aurélie Falcou, Nina Reckefuss, Markus Rojahn,
Valèrie Wiederhirn, Paula Rudati, Holger Frohne, Oskar Nuyken,
Heinrich Becker, Klaus Meerholz
Multi-colour Organic Light-emitting Displays by Solution Processing
Nature **421**, 829-833 (2003).

Holger Frohne, Sean E. Shaheen, Christoph J. Brabec, David C. Müller, N.S. Sariciftci, Klaus Meerholz
Influence of the Anodic Work Function on the Performance of Organic Solar Cells
ChemPhysChem **9**, 795-799 (2002).

Holger Frohne, David C. Müller, Klaus Meerholz
Continuously Variable Hole Injection in Organic Light Emitting Diodes
ChemPhysChem **8**, 707-711 (2002).

Holger Frohne, Shouke Yan, Klaus Dieter Rogausch, Alexander Karbach, Jürgen Petermann
Friction-transfer of Polymeric Materials Using Ultra-high Shear Rates
J. Mat. Sci. Let. **20**, 595–596 (2001).

9.2.2 Talks

Holger Frohne, D. C. Müller, N. Reckefuss, P. Rudati, K. Meerholz
Optimization of organic semiconductor devices by anode modification
[4800-38]
SPIE Annual Meeting 2002, Seattle, USA, 9. Jul. 2002

Holger Frohne, Markus Groß, David Müller, Klaus Meerholz
Manipulation of the Work Function of Conducting Polymers
Seminar, Inteligent Polymer Research Institute, University of Wollongong, Australia, 27. Sep. 2001

Holger Frohne, Markus Groß, David Müller, Klaus Meerholz
Adjustable Anodic Barrier in Polymeric Semiconductor Devices
Seminar, Dep. Physics , The University of Newcastle, Australia, 21. Sep. 2001

Holger Frohne, Markus Groß, David Müller, Klaus Meerholz
Manipulation of the Work Function of Conducting Polymers
6th Meeting „Electrode Reaction Mechanisms and Interfacial Structure"
(ERMIS), Bad Koesen, Mar. 2000

9.2.3   Poster Presentations

Holger Frohne, Markus Groß, David Müller, and Klaus Meerholz
Conjugated Polymers: Hole-Injecting Materials with Adjustable Work Function
DPG Tagung, Symposium Organische Festkörper, 26.-30. Mar. 2001,
Hamburg

Holger Frohne, Klaus Dieter Rogausch, Alexander Karbach, and Jürgen
Petermann
Reibungsinduzierte Herstellung von ultradünnen Polymerfilmen
DPG Tagung, Fachverbände Chemische Physik und Polymerphysik, 13.-16.
Mar. 2000, Potsdam

Holger Frohne, Alexander Karbach, Jürgen Petermann
Friction Induced Polymer Morphologies
29th German Electron Microscopy Congress, 5-10. Sep. 1999, Dortmund,
Germany

9.3 Zusammenfassung

Im Rahmen dieser Arbeit wurde das System „PEDOT (poly(3,4-ethylendioxythiophen)) als elektrochemisch eingestelltes Anodenmaterial für organische Bauteile" eingehend untersucht. Zunächst wurden PEDOT Filme elektrochemisch polymerisiert, die dann in einem zweiten elektrochemischen Schritt auf ein elektrochemisches Potential eingestellt wurden. Die resultierende Austrittsarbeit des eingestellten Oxidationsgrades wurde dann mittels eines Kelvinschwingerexperiments gemessen. Diese Arbeit zeigt, dass es einen direkten (linearen) Zusammenhang zwischen dem eingestellten elektrochemischen Potential und der Austrittsarbeit der Oberfläche gibt. Ein weiteres Ziel dieser Arbeit war, diese Austrittsarbeitsänderungen zu nutzen, um die elektronischen Eigenschaften organischer Bauteile zu optimieren.

Organische halbleitende Polymerbauteile der folgenden Struktur wurden daher präpariert:

Indium-Zinn-Oxid (ITO) / elektrochemisch abgeschieden und dotiertes PEDOT / elektroaktives Polymer / Metallelektrode

PEDOT diente in diesem Aufbau als Anodenmaterial und hat somit großen Einfluss auf die Injektion von Löchern. Der Dotierungsgrad (Oxidationsgrad) der PEDOT-Schicht wurde elektrochemisch eingestellt und der Einfluss auf die darauf aufgebauten elektronischen Bauteile untersucht.

Photovoltaische Messungen an derartigen Bauteilen spiegeln die Austrittsarbeitsdifferenz zwischen den Elektrodenmaterialien wider. Auch die Ergebnisse dieser Messungen belegten den direkten (linearen) Zusammenhang zwischen dem eingestellten elektrochemischen Potential und der Austrittsarbeit.

In einem nächsten Schritt wurde diese Entdeckung der quantitativ kontrollierten Einstellbarkeit der Austrittsarbeit verwendet, um organische Leuchtdioden (OLED) und organische Solarzellen (OSC) zu optimieren.

Für OLED mit verschiedenen Kathodenmaterialien (z. B. Ca oder Al) konnten so die jeweils optimale Lochinjektionsbarriere (entsprechend dotiertes PEDOT) eingestellt werden. Es konnte gezeigt werden, dass aneinander angepasste Ladungsträgerbarrieren auf Kathoden- bzw. Anodenseite eine optimale Effizienz erzielen. Der Einsatz von Bauteilen, die ausschließlich einen Lochstrom erlauben (Elektronen werden durch hohe Injektionsbarrieren abgeblockt), erlaubte eine Aussage über die Stromzusammensetzung in Bauteilen, in denen beide Ladungsträgersorten zum Strom beitragen. Die Ermittlung der ladungsträgerspezifischen Stromzusammensetzung bestätigten verbesserte Effizienzen, die experimentell durch frei eingestellte Barrieren erzielt werden konnten.

Die Variation der Austrittsarbeit der PEDOT-Schicht hat auch direkten Einfluss auf die physikalischen Eigenschaften der OSC. Da die Differenz der

Austrittsarbeiten der jeweiligen Elektroden das energetische Gefälle im Bauteil bestimmt, verändern sich mit zunehmender PEDOT-Austrittsarbeit – also mit größer werdendem Energieunterschied der Elektroden - die Kurzschlussströme und Leerlaufspannungen zu höheren Werten. Es konnte gezeigt werden, dass bei geeigneter Wahl der Materialien die PEDOT-Schicht auch als Kathode fungieren kann. Das ist nämlich dann der Fall, wenn die Austrittsarbeit des PEDOT das Energieniveau des Kathodenkontakts unterschreitet. In dieser Arbeit wurden so erstmals „invertierte" Bauteile hergestellt.

9.4 <u>Eidesstattliche Erklärung</u>

Ich versichere, dass ich die von mir vorgelegte Dissertation selbständig angefertigt, die benutzten Quellen und Hilfsmittel vollständig angegeben und die Stellen der Arbeit – einschließlich Tabellen, Karten und Abbildungen -, die anderen Werken im Wortlaut oder dem Sinn nach entnommen sind, in jeder Einzelfall als Entlehnung kenntlich gemacht habe; dass diese Dissertation noch keiner anderen Fakultät oder Universität zur Prüfung vorgelegen hat; dass sie – abgesehen von unten angegebenen Teilpublikationen – noch nicht veröffentlicht worden ist sowie, dass ich eine solche Veröffentlichung vor Abschluss des Promotionsverfahrens nicht vornehmen werde. Die Bestimmungen dieser Promotionsordnung sind mir bekannt. Die von mir vorgelegte Dissertation ist von Prof. Dr. Klaus Meerholz betreut worden.

Newcastle (AUS), den 23.02.04

_____
Holger Frohne

Teilpublikationen:

Holger Frohne, Christopher R. McNeill, Gordon G. Wallace, Paul C. Dastoor
Enhancement of polymer electronics via surface states on highly doped polymeric anodes
J. Phys. D. **37**, 165-170 (2004).

Holger Frohne, David C. Müller, Nina Reckefuß, Paula Rudati, Klaus Meerholz
Optimisation of Organic Semiconductor Devices by Anode Modification
SPIE proceedings **4800**, 172-181 (2003).

Holger Frohne, Sean E. Shaheen, Christoph J. Brabec, David C. Müller, N.S. Sariciftci, Klaus Meerholz
Influence of the Anodic Work Function on the Performance of Organic Solar Cells
ChemPhysChem **9**, 795-799 (2002).

Holger Frohne, D.C. Müller, Klaus Meerholz
Continuously Variable Hole Injection in Organic Light Emitting Diodes
ChemPhysChem **8**, 707-711 (2002).

9.5 **Lebenslauf**

Persönliche Daten

Name:	Holger Frohne
Geburtstag:	16. April 1973
Geburtsort:	Dortmund (D)
Staatsangehörigkeit:	deutsch
Familienstand:	verheiratet, 1 Kind

Schulbildung und Wehrdienst

1979-1983	Dudenrothschule Holzwickede (Grundschule)
1983-1992	Pestalozzi Gymnasium Unna
06/1992	Schulabschluss: Abitur
07/1992	Gefahrgutfahrer und Erdarbeitsgeräteführer
-09/1993	bei Landvermessungsarbeiten in Sachsen

Hochschul- und Promotionsstudium

1993-1998	Studium der Physik an der Universität Dortmund
11/1999	Diplomarbeit: *Friction-transfer of Polymeric Materials Using Ultra-high Shear Rates* (Prof. Dr. Jürgen Petermann) Fachbereich Chemietechnik, Universität Dortmund in Zusammenarbeit mit der Bayer AG
seit 04/2000	Promotionsstudium: *Doping of Hole Conducting Polymers Utilized to Enhance Polymer Electronics* (Prof. Dr. Klaus Meerholz) Department für Chemie und Center for Nanoscience (CeNS) an der Universität München

Arbeitsverhältnisse

seit 01/1999	Studentische Hilfskraft, Universität Dortmund
seit 11/1999	Wissenschaftlicher Mitarbeiter im Fachbereich Chemietechnik, Universität Dortmund
seit 04/2000	Wissenschaftlicher Mitarbeiter im Department Chemie an der Universität München
von 08/2002 bis 03/2003	Wissenschaftlicher Mitarbeiter am Institut für Physikalische Chemie an der Universität zu Köln